

# Lawrence Berkeley National Laboratory

## Recent Work

### **Title**

Ultrafast X-ray absorption spectroscopy: Properties of liquid silicon and carbon

### **Permalink**

<https://escholarship.org/uc/item/2h0747q7>

### **Author**

Johnson, Steven L.

### **Publication Date**

2002-12-16



# ERNEST ORLANDO LAWRENCE BERKELEY NATIONAL LABORATORY

## Ultrafast X-Ray Absorption Spectroscopy: Properties of Liquid Silicon and Carbon

Steven L. Johnson

Advanced Light Source Division

December 2002

Ph.D. Thesis



REFERENCE COPY  
 Does Not  
 Circulate  
 Library Annex Reference  
 Copy 1

Lawrence Berkeley National Laboratory

## **DISCLAIMER**

This document was prepared as an account of work sponsored by the United States Government. While this document is believed to contain correct information, neither the United States Government nor any agency thereof, nor the Regents of the University of California, nor any of their employees, makes any warranty, express or implied, or assumes any legal responsibility for the accuracy, completeness, or usefulness of any information, apparatus, product, or process disclosed, or represents that its use would not infringe privately owned rights. Reference herein to any specific commercial product, process, or service by its trade name, trademark, manufacturer, or otherwise, does not necessarily constitute or imply its endorsement, recommendation, or favoring by the United States Government or any agency thereof, or the Regents of the University of California. The views and opinions of authors expressed herein do not necessarily state or reflect those of the United States Government or any agency thereof or the Regents of the University of California.

**Ultrafast X-Ray Absorption Spectroscopy:  
Properties of Liquid Silicon and Carbon**

Steven Lee Johnson  
Ph.D. Thesis

Department of Physics  
University of California, Berkeley

and

Advanced Light Source Division  
Ernest Orlando Lawrence Berkeley National Laboratory  
University of California  
Berkeley, CA 94720

December 2002

**Ultrafast X-Ray Absorption Spectroscopy:  
Properties of Liquid Silicon and Carbon**

by

Steven Lee Johnson

B.S. (Harvey Mudd College) 1997

A dissertation submitted in partial satisfaction of the  
requirements for the degree of  
Doctor of Philosophy

in

Physics

in the

GRADUATE DIVISION

of the

UNIVERSITY OF CALIFORNIA, BERKELEY

Committee in charge:

Professor Roger W. Falcone, Chair

Professor Joseph Orenstein

Professor Jeffrey Bokor

Fall 2002

**Ultrafast X-Ray Absorption Spectroscopy:  
Properties of Liquid Silicon and Carbon**

Copyright © 2002

by

Steven Lee Johnson

The U.S. Department of Energy has the right to use this document  
for any purpose whatsoever including the right to reproduce  
all or any part thereof.

## Abstract

Ultrafast X-Ray Absorption Spectroscopy:

Properties of Liquid Silicon and Carbon

by

Steven Lee Johnson

Doctor of Philosophy in Physics

University of California, Berkeley

Professor Roger W. Falcone, Chair

A new technique of picosecond time-resolved x-ray absorption spectroscopy is applied to the study of the high-temperature, volatile liquids resulting from the heating of solid foils with a femtosecond laser pulse. In particular, this method is used to study the electronic structure and short-range atomic structure of liquid silicon and the bonding properties of liquid carbon at a variety of near-solid densities. The absorption spectra obtained by the experiment are compared to the predictions of molecular dynamics simulations. In silicon, this results in a largely successful quantitative match of experiment to *a priori* x-ray scattering theory. In carbon, fits of the liquid spectra to the sum of separately identifiable components allow quantitative statements about the types of bonding present in the liquid at various densities that agree in many respects

with the simulation results available in the literature. The success of these methods in studying the liquid forms of silicon and carbon demonstrates their potential to study a wide range of materials under extreme conditions of temperature and pressure.

---

Professor Roger W. Falcone  
Dissertation Committee Chair

# Contents

<b>List of Figures</b>	<b>iv</b>
<b>List of Tables</b>	<b>vi</b>
<b>1 Introduction</b>	<b>1</b>
1.1 Time-resolved x-ray diffraction . . . . .	4
1.2 Time-resolved x-ray spectroscopy . . . . .	7
1.2.1 Overview of x-ray absorption spectroscopy (XAS) . . . . .	8
1.2.2 X-ray absorption near edge structure (XANES) . . . . .	8
1.2.3 Extended x-ray absorption fine structure (EXAFS) . . . . .	11
1.2.4 Towards ultrafast XAS in warm dense systems . . . . .	14
<b>2 Experimental apparatus</b>	<b>16</b>
2.1 Synchrotron x-ray source . . . . .	16
2.1.1 Theory of bend magnet radiation . . . . .	17
2.1.2 Timing structure of the x-ray pulses . . . . .	23
2.2 Femtosecond laser system . . . . .	26
2.2.1 Oscillator . . . . .	26
2.2.2 Amplifiers . . . . .	32
2.3 Beamline endstation . . . . .	40
2.4 Overall timing . . . . .	53
<b>3 Time-resolved XAS of liquid silicon</b>	<b>64</b>
3.1 Background and previous work . . . . .	64
3.2 Pump-probe data . . . . .	65
3.3 Streak camera data . . . . .	69
3.4 Modeling . . . . .	71
3.5 Summary and future work . . . . .	78

<b>4</b>	<b>Bonding in liquid carbon</b>	<b>81</b>
4.1	Pump-probe results: low density liquid . . . . .	85
4.2	Higher densities: tamping . . . . .	91
4.2.1	Liquid carbon at 2.2 g/cc . . . . .	93
4.2.2	Liquid carbon at 2.6 g/cc . . . . .	96
4.3	Streak camera measurements . . . . .	98
4.4	Modeling . . . . .	100
4.4.1	Analysis of higher-energy $\sigma^*$ resonances . . . . .	104
4.4.2	Estimate of $\pi$ bond fraction and local bond structures . . . . .	110
4.5	Summary and future work . . . . .	114
<b>5</b>	<b>Conclusion</b>	<b>116</b>
<b>A</b>	<b>Electronic phase shifter</b>	<b>118</b>
A.1	Oscillator timing control . . . . .	119
A.2	Amplifier timing control . . . . .	122
A.3	Calibration . . . . .	122
A.4	Overview of computer control programs . . . . .	124
<b>B</b>	<b>Optical self-absorption</b>	<b>127</b>
<b>C</b>	<b>Grating spectrograph</b>	<b>134</b>
<b>D</b>	<b>Oscillator strength of <math>\pi^*</math> resonances</b>	<b>140</b>
<b>E</b>	<b>Computer scripts and code</b>	<b>144</b>
E.1	Makefile (for C programs) . . . . .	144
E.2	Phase shifter scripts and code . . . . .	146
E.2.1	readps-wrap.sh . . . . .	146
E.2.2	setps-d-wrap.sh . . . . .	147
E.2.3	shiftrrel-wrap.sh . . . . .	148
E.2.4	readps.c . . . . .	149
E.2.5	setps-d.c . . . . .	150
E.2.6	shiftrrel.c . . . . .	151
E.2.7	ps_constants.h . . . . .	153
E.2.8	ps.h . . . . .	154
E.2.9	ps.c . . . . .	155
E.2.10	dg.h . . . . .	161
E.2.11	dg.c . . . . .	162
E.2.12	serial-ps.h . . . . .	166
E.2.13	serial-ps.c . . . . .	166
E.2.14	setpsabs.c . . . . .	168
E.2.15	setiq.c . . . . .	169

E.3	Slow-feedback control scripts and code . . . . .	171
E.3.1	driftd.sh . . . . .	171
E.3.2	driftcheck.sh . . . . .	171
E.3.3	drift.c . . . . .	172
<b>Bibliography</b>		<b>175</b>

# List of Figures

1.1	Conceptual diagram of x-ray diffraction from a crystal. . . . .	5
1.2	Energy level diagram showing x-ray absorption pathways . . . . .	9
1.3	Broad spectral overview of x-ray absorption in a typical system . . . . .	10
1.4	Sketch of photoelectron scattering in a simple molecular system . . . . .	12
2.1	Overview of the Advanced Light Source. . . . .	18
2.2	Sketch of radiation emitted by a curved electron path. . . . .	21
2.3	Vertical angular dependence of bend-magnet radiation . . . . .	22
2.4	Spectral distribution of photon flux for ALS beamline 5.3.1. . . . .	23
2.5	Pictorial sketch of a typical electron bunch timing mode at the ALS . . . . .	25
2.6	Sketch of oscillator beam path. . . . .	28
2.7	Block diagram of oscillator synchronization. . . . .	29
2.8	Sketch of stretcher/compressor for CPA . . . . .	33
2.9	Sketch of the regenerative amplifier. . . . .	34
2.10	Sketch of the 1 KHz two-pass amplifier stage. . . . .	37
2.11	Sketch of the 10 Hz two-pass amplifier stage. . . . .	39
2.12	Timing of oscillator pulses to synchrotron roundtrip clock . . . . .	41
2.13	Sketch of absorption experiment at beamline 5.3.1. . . . .	42
2.14	Spectral reflectivity of filtering mirror pairs. . . . .	45
2.15	Sketch of MCP based pump-probe detector . . . . .	48
2.16	Sketch of ultrafast x-ray streak camera. . . . .	50
2.17	Operation of meander sweep plates in the streak camera. . . . .	51
2.18	Sketch of GaAs photoconductive switch. . . . .	52
2.19	Block diagram of timing setup for silicon foil experiments. . . . .	54
2.20	Block diagram of timing setup for carbon foil experiments. . . . .	55
2.21	Circuit schematic of edge synchronization box . . . . .	57
2.22	Circuit schematic of single-shot box . . . . .	57
2.23	Circuit schematic of extended single-shot box . . . . .	59
2.24	Circuit schematic for x10 multiplier circuit . . . . .	60
2.25	Timing diagram of signals in the carbon experiment. . . . .	63

3.1	Silicon absorption data from Murakami, et al. . . . .	66
3.2	Absorption data from pump-probe experiments on silicon . . . . .	67
3.3	Fluence dependence of $L_{II,III}$ edge absorption . . . . .	68
3.4	Dynamics of the $L_{II,III}$ post-edge absorption . . . . .	70
3.5	Pair correlation function in liquid silicon from simulation and literature	72
3.6	Comparison of model results for the $L_{II,III}$ XANES to experiment . .	74
3.7	Phase-corrected EXAFS FFT . . . . .	75
3.8	Model spectrum resulting from imposing a $\pm 15\%$ range of densities on the MD liquid structure . . . . .	77
3.9	Model calculations of the $L_I$ edge compared to experiment . . . . .	79
4.1	Phase diagram of carbon . . . . .	83
4.2	Results of tight-bonding MD simulations from ref. [58] . . . . .	85
4.3	Absorption spectrum of low-density liquid carbon . . . . .	86
4.4	Fluence dependence of pre-edge absorption in untamped carbon . . .	87
4.5	Fluence dependence of ablation crater radius in bulk HOPG . . . . .	88
4.6	Pictorial explanation of the asymmetric shape of $\sigma^*$ resonances . . . .	90
4.7	X-ray transmission of the LiF tamping layers . . . . .	93
4.8	Absorption spectrum of liquid carbon at 2.2 g/cc . . . . .	94
4.9	Fluence dependence of the pre-edge absorption for tamped soft carbon	95
4.10	Absorption spectrum of liquid carbon at 2.6 g/cc . . . . .	97
4.11	Fluence dependence of pre-edge absorption in tamped DLC foils . . . .	98
4.12	Absorption spectrum integrated from 5–10 ps after heating . . . . .	99
4.13	Picosecond dynamics of the $\pi^*$ and $\sigma^*$ absorption bands . . . . .	101
4.14	Results of fitting to the (unheated) soft amorphous carbon spectrum.	105
4.15	Results of fitting to the (unheated) solid DLC spectrum. . . . .	105
4.16	Results of fitting to the untamped liquid carbon spectrum. . . . .	106
4.17	Results of fitting to the 2.2 g/cc liquid carbon spectrum. . . . .	106
4.18	Results of fitting to the 2.6 g/cc liquid carbon spectrum. . . . .	108
A.1	Functional schematic of the I-Q vector modulator (phase shifter). . .	120
A.2	Relationship of inputs I and Q to the phase shift $\theta$ . . . . .	121
A.3	Calibration of I and Q pin voltages . . . . .	123
A.4	Phase accuracy of calibrated phase shifter apparatus. . . . .	124
B.1	Radiation exchange between two points in an integrating sphere. . . .	129
B.2	Optical self-transmission measurement setup . . . . .	131
B.3	Optical self-reflectivity measurement setup . . . . .	132
C.1	Sketch of grating spectrograph . . . . .	135

# List of Tables

2.1	Explanation of symbols and functions used in equation 2.1. . . . .	20
2.2	Resistor values in figure 2.24 . . . . .	61
4.1	Numerical summary of fit results . . . . .	107
4.2	Fraction of the absorption spectra due to $\pi^*$ states . . . . .	111
B.1	Results of optical self-absorption measurements. . . . .	133

## Acknowledgments

This work would not have been possible without vital contributions from many different people. First, I would like to thank Phil Heimann for his tremendous support for this project and his guidance throughout. Similarly, my co-workers through my years at the ALS—Aaron Lindenberg, Andrew MacPhee, Donnacha Lowney, Inuk Kang, and Thomas Missalla—who all contributed many hours to this and related work when any sane person would be asleep.

I owe a lot to Roger Falcone, my advisor, for providing the vision for this project and for giving me the freedom to explore different possibilities. Our discussions have always been a valuable resource.

Zenghu Chang also deserves much thanks for his development of the streak camera used in these experiments and his timely responses to urgent questions. Othon Monteiro cheerfully produced the DLC samples used in the experiments on liquid carbon. Harald Jeschke and Martin Garcia performed the MD simulations of liquid silicon, and John Rehr was an important source of information for using his FEFF code to calculate absorption spectra. For very fruitful discussions on a wide range of topics related to this work, I would also like to thank Dick Lee, Andrea Cavalleri, Andrew Ng, and Javier Díaz.

Finally, I must thank all my friends and family for their support over the last few years. Hopefully I can continue to rely on their contributions for many years to come.

# Chapter 1

## Introduction

The use of ultrafast laser pulses to manipulate the electronic and structural properties of materials has long captured the imagination of scientists. Even more sophisticated ideas of using phase-shaped laser pulses to guide chemical reaction pathways have recently been implemented to achieve some control over molecular dissociation pathways [107, 6]. In condensed phase systems, experimental observations [28, 94, 75, 78, 84] and supporting theoretical work [86, 87, 82, 44] demonstrate that the manipulation of electronic populations by femtosecond laser pulses can result in a nonthermal phase transition from solid to liquid on sub-picosecond time scales. The possibility of using ultrafast optical pulses to induce nonthermal solid-solid phase transitions has also been explored theoretically [44] and experimentally [22, 31]. The idea of controllably manipulating the structure of a solid material via laser excitation is tantalizing, but realization of this dream requires a more detailed understanding of

light-matter interactions and the basic physics underlying highly excited condensed phase systems.

Perhaps the simplest model for how ultrafast laser pulses interact with solids is to treat the laser interaction as an impulsive delivery of thermal energy to the system. This model is valid only at times well after the directly excited modes of the solid (usually excited electronic states, but possibly also a set of optical phonon modes) reach a state of local equilibrium with the rest of the system. In cases where the primary mechanisms for optical energy absorption are electronic, this time is characterized by the electron-phonon coupling time, measured to be on the order of 1 ps for a variety of condensed phase materials [53, 80, 12, 27]. This fairly short relaxation time raises interesting possibilities for using femtosecond laser pulses to study near-solid density materials heated to temperatures well above the range where conventional static measurements are feasible, due to the inherent volatility of materials under these conditions. This is a regime of phase space between the realms of solid state physics and plasma physics, so far poorly understood due to the experimental challenges surrounding it. Materials under these conditions play important roles in the physics of planetary cores [77] and in constructing accurate models of systems that make a transition from solid to plasma. Knowledge of high-temperature, high-density physics could also contribute to efforts to achieve efficient, controllable fusion, although so far known sustainable fusion reactions require densities much greater than that of most solids [41].

Given that ultrafast laser pulses are well suited to creating transient states of dense, high-temperature matter, we also require some way of probing the resulting state. One obvious requirement for a probe is sufficiently high temporal resolution to permit observation of the transient before significant expansion, vaporization or cooling has occurred. An easy approach to this problem is to use another ultrafast optical pulse, probably derived from the same pulse used to excite the solid. This has the advantage of high temporal resolution, and indeed experiments have been attempted using this technique [28, 94, 75, 81, 103]. An unfortunate disadvantage of this type of probe is the very limited information that is available. Optical pulses interrogate material properties that extend over many atomic sites, while the most valuable information for relating experiments to model calculations concerns the interaction between individual atoms. An ideal probe would be able to map out both the electronic and atomic structure of the heated transient in a way that can be related directly to the bonding properties of the material.

X-ray measurements are a powerful way of probing these kinds of material properties. The advent of synchrotrons designed specifically for x-ray production has, over the past few decades, stimulated a tremendous development of new techniques to probe the electronic and atomic structure of materials. Adapting these techniques to the picosecond temporal resolution required to probe the transient heated matter discussed above is not trivial, but recent developments at synchrotrons and with laser-produced plasma sources have made some experiments possible. Two general avenues

of development in time-resolved x-ray science have so far been pursued: diffraction and spectroscopy.

## 1.1 Time-resolved x-ray diffraction

X-ray diffraction is a process whereby wave interference effects modify the scattering of hard x-rays from electrons. Since most of the electrons in a material are tightly bound to atomic nuclei, diffraction is generally sensitive only to the atomic structure of the material.<sup>1</sup> Figure 1.1 shows a conceptual diagram of x-ray diffraction from a crystal in a symmetric Bragg geometry. For this situation of plane wave diffraction from a set of lattice planes, constructive interference enhances scattering when the experimental conditions satisfy the Bragg condition

$$m\lambda = 2d \sin(\theta), \quad (1.1)$$

where  $m$  is an integer indicating the order of the reflection,  $\lambda$  is the x-ray wavelength,  $d$  is the distance between lattice planes, and  $\theta$  is the angle of incidence. By monitoring the position and shape of this Bragg peak as a function of experimentally controllable parameters such as  $\theta$  or  $\lambda$ , experiments using time-resolved x-ray diffraction can measure changes in the spacing and orientation of the lattice planes.

Several groups have recently demonstrated the ability to do time-resolved x-ray diffraction with time resolution approaching the pulse duration of ultrafast optical

---

<sup>1</sup>Exceptions to the general rule exist. For example, in situations where the arrangement of ionic cores in the lattice cause destructive interference for a particular reflection but scattering from valence electrons does not, a structurally “forbidden” diffraction peak may be observed in an experiment

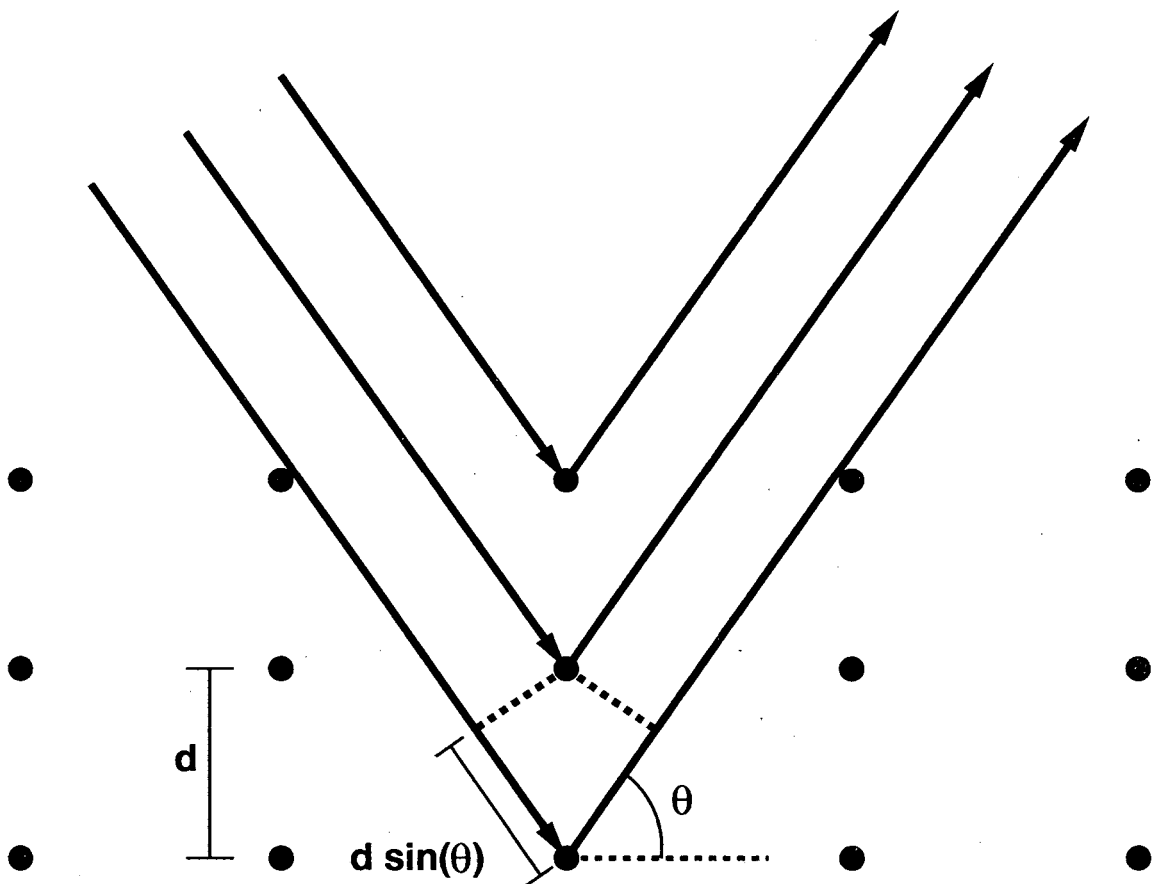


Figure 1.1: Conceptual diagram of x-ray diffraction from a crystal.

lasers. The picosecond time scale dynamics of coherent phonons generated by the impulsive stress of a femtosecond laser pulse have been observed with laser plasma sources [84, 20, 76] and with synchrotron based sources [53, 74, 51]. At higher laser fluences, experiments on excited semiconductors have observed a fast sub-picosecond drop in the integrated intensity of a Bragg reflection [84, 78], an effect attributed to ultrafast nonthermal melting previously inferred from optical measurements. Other work has observed the growth of an additional Bragg peak in diffraction from a laser-excited VO<sub>2</sub> crystal, evidence for a phase transition of the excited surface layer to another crystalline phase [22].

Time-resolved diffraction has also been applied to the study of systems that are not single crystals, by observation of changes in the Debye-Scherrer ring patterns produced by diffraction from a collection of randomly oriented molecules or small crystals. Synchrotron sources have been used to perform picosecond studies of the structural dynamics of solvated molecular systems [63] and the powder of an organic crystal [91]. Some discussion has recently focused on the possibility of doing ultrafast diffraction to study single protein molecules, but actual experiments must await new technologies to create more intense and much shorter pulses of hard x-rays [64].

Extensions of x-ray diffraction into the ultrafast regime have had considerable success, but there are a number of important limitations to the techniques that have so far been developed. First, severe limitations in the number of useful x-ray photons is a tight constraint for many experiments. Many important experiments are by nature

irreversible, requiring that the sample under study be renewed for each laser pump cycle which sets a practical limitation on the repetition rate of the experiment. The low scattering cross section for high energy x-rays from electrons is also a problem, frequently causing a mismatch between the x-ray probe depth (typically  $> 1 \mu\text{m}$  in many solids) and the optical absorption depth for high fluence femtosecond laser pulses ( $\sim 0.1 \mu\text{m}$ ). Since x-ray diffraction is primarily a tool for measuring long-range order, time-resolved diffraction on crystals on a picosecond time scale is highly sensitive to thermally generated strain waves, potentially masking other, more subtle effects. In solvated or heterogeneous systems without long-range order, another problem is overlap in the diffuse scattering patterns of different local structures that can confuse interpretation of the results.

## 1.2 Time-resolved x-ray spectroscopy

X-ray spectroscopy is a term for a variety of techniques, many of which are currently under active development for systems under static conditions. Although x-ray photoelectron spectroscopy has been applied on very fast time scales [66, 67, 102], probably the easiest technique to apply to ultrafast studies of condensed systems is x-ray absorption spectroscopy. Since absorption spectroscopy is also the primary subject of this dissertation, we will concentrate solely on this method.

### 1.2.1 Overview of x-ray absorption spectroscopy (XAS)

Absorption spectroscopy is simply the measurement of the photoabsorption cross section of a material as a function of photon energy. Absorption spectra in the x-ray range are dominated by large step-like functions in the cross section, occurring at energies where the photon energy becomes sufficient to promote core level electrons to the lowest-lying unoccupied electronic states allowed by selection rules. Figure 1.2 shows an energy level diagram depicting some mechanisms for absorption in a condensed system, along with the spectroscopic notation for these transitions. A corresponding absorption spectrum might look like figure 1.3. Note that the position of an edge is unique to a particular element.

Measurements of the absorption cross section in the vicinity of these edges reveals a great deal of structure above the edge, extending for several hundred eV of photon energy. This structure contains a great deal of information about the properties of the material. Traditionally, the absorption edge structure is divided into two regions: the x-ray absorption near-edge structure (XANES) for structure within roughly 50 eV of the edge, and the extended x-ray absorption fine structure (EXAFS) at higher energies.

### 1.2.2 X-ray absorption near edge structure (XANES)

In principle, the absorption spectrum is fully calculable from an appropriate application of Fermi's Golden Rule for the probability per unit time for the transition

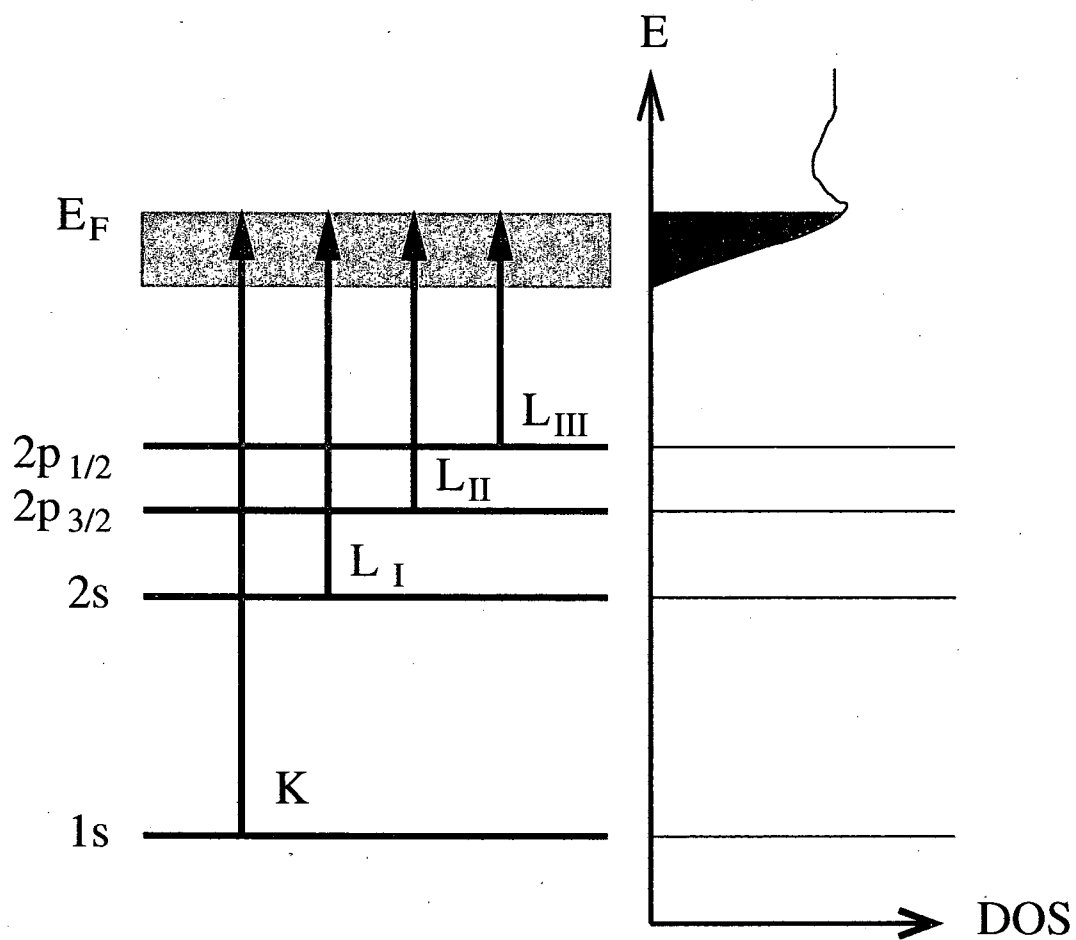


Figure 1.2: Energy level diagram showing some possible x-ray absorption pathways in a condensed system. The diagram is not to scale.

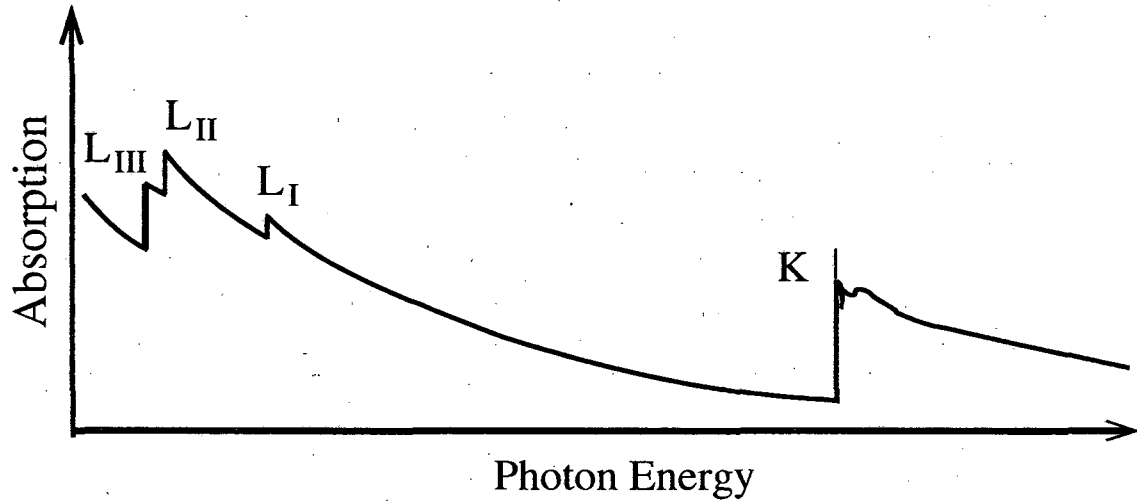


Figure 1.3: Hypothetical absorption spectrum over a broad range of photon energies.

from an initial state  $|i\rangle$  to a final state  $|f\rangle$  in the presence of an electromagnetic field:

$$P = \frac{2\pi}{\hbar} |\langle f | H_i | i \rangle|^2 \rho_f(\epsilon), \quad (1.2)$$

where  $H_i$  is the electromagnetic interaction Hamiltonian and  $\rho_f(\epsilon)$  is the energy density of final states. With some work this can be cast as an expression for the absorption cross section  $\sigma_x$ :

$$\sigma_x = \frac{4\pi\hbar^2\alpha}{m^2E} |\langle f | \mathbf{e} \cdot \mathbf{p} | i \rangle|^2 \rho_f(\epsilon), \quad (1.3)$$

where  $\alpha$  is the atomic fine structure constant,  $\mathbf{e}$  is a unit vector indicating the x-ray polarization direction, and  $\mathbf{p}$  is the momentum operator [88]. Although an exact evaluation of this expression can be difficult, it shows that a lot of the post-edge absorption structure depends intimately on the energy density of final states permitted by the dipole selection rules. Although this density of states information is not always strictly comparable to the ground state of the system due to the influence of

the core hole, the near edge spectrum still provides a powerful probe of molecular orbital antibonding resonances and band structure in the local environment of an x-ray absorber.

An alternative way of viewing the origin of absorption edge structure is to consider the effects of interference in the photoelectron wavefunction resulting from scattering. Figure 1.2.2 is a sketch of photoelectron scattering in a three-atom molecular system. The basic idea is that the absorption cross section is, in a system with a highly localized core state, proportional to the probability of finding the ejected photoelectron at the site of the absorber [73]. This scattering model of the absorption structure can be computed by existing computer codes [4], although their accuracy is sometimes compromised by the presence of non-spherical components of the electron potential from valence electrons and by core hole interactions, effects which are not completely understood from a quantitative perspective [73]. The codes are, however, sufficiently accurate to make statements about local structure in many systems.

### 1.2.3 Extended x-ray absorption fine structure (EXAFS)

For higher photon energies, the scattering formalism simplifies somewhat as we enter the realm of EXAFS. A higher photon energy translates into a higher photoelectron wavenumber  $k$ , and at higher wavenumbers the decay of the wavefunction with path length from the absorber becomes more steep. At energies higher than roughly 50 eV above the edge, the dominant scattering paths are single reflections from near-

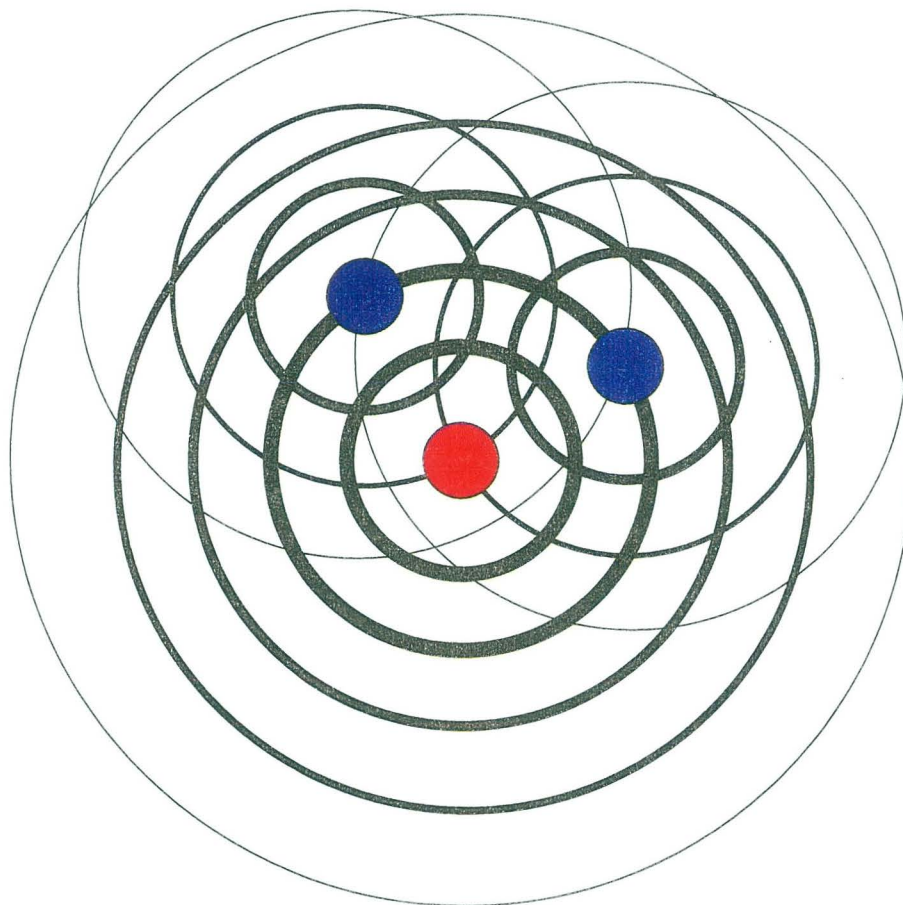


Figure 1.4: Diagram of photoelectron scattering in a hypothetical molecular system, showing the interference effects caused by scattering. The red circle indicates the x-ray absorber.

est neighbor atoms (although other reflections do still contribute). The contribution of this high-energy scattering to the absorption is given by the semi-phenomenological EXAFS equation

$$\chi(k) = \sum_R S_0^2 N_R \frac{|f(k)|}{kR^2} \sin(2kR + 2\delta_c + \Phi) e^{-2R/\lambda(k)} e^{-2\sigma_d^2 k^2}, \quad (1.4)$$

where  $\chi(k)$  is a normalized change in the absorption cross section (with the smoothly varying atomic-like contribution subtracted out),  $S_0$  is an amplitude factor from many-body effects,  $R$  is the distance from the absorber to a given shell of scattering neighbors,  $N_R$  is the number of atoms in this shell,  $|f(k)|$  is the backscattering amplitude,  $\delta_c$  is the phase shift from the central absorber,  $\Phi$  is the phase shift from an atom in the shell,  $\lambda(k)$  is a parameter representing the decay of the wavefunction with distance (the mean free path), and  $\sigma_d$  is the rms distribution of distance between the absorber and atoms in the shell, arising from either thermal fluctuations or structural disorder. Current *ab initio* scattering codes can calculate all the relevant parameters in this equation and can predict very accurately the EXAFS structure using only the actual structure of the material under study as an adjustable parameter [4, 5]. EXAFS spectra are now routinely used to measure nearest neighbor bond distances and coordination numbers, and with difficulty higher order shells and even bond angles can be inferred in some cases.

### 1.2.4 Towards ultrafast XAS in warm dense systems

Since XAS as a measurement technique offers the promise of measuring simultaneously the electronic and atomic structure of materials, it is an attractive prospect for an ultrafast probe of laser-induced phenomena. As with x-ray diffraction, progress in realizing this idea is closely tied to the development of intense, short pulses of x-rays, with the added requirement of broad spectral tunability. Laser-produced plasmas can give broad continuum x-ray pulses in the soft x-ray range with pulse widths that range from hundreds of picoseconds to nanoseconds, and they have been used to study the photoinduced responses of solvated SF<sub>6</sub> [72], aluminum [104], and silicon [60, 34, 96, 61]. Some groups have also used synchrotron sources, with intrinsic pulse widths of  $\sim 100$  ps, to study nanosecond [24] and even pulse duration limited picosecond XAS [11] in solvated molecular systems.

Picosecond XAS is in many ways a good way to probe the transient states of high temperature, solid density systems produced by high energy femtosecond optical pulses. The high temperature of these materials generally means there is no long range order, so the sensitivity to short range order in absorption spectroscopy is a definite advantage. When operating in a transmission geometry, x-ray absorption spectroscopy is not sensitive to changes in the highly volatile surface. Soft x-ray absorption also has a much higher cross section than diffraction, making it possible in condensed systems to easily match the probe depth with the laser excitation depth, even at the optical pump intensities needed to heat solids to very high temperatures.

Finally, the information on electronic bonding and local structure from XAS provides a valuable experimental basis for the development of a microscopic theory of such systems.

This dissertation reports on the application of picosecond time-resolved XAS to the study of high-temperature liquid silicon and liquid carbon at densities close to that of the solid phase. Liquid silicon provides an important model system for development of the technique, since it can be compared with earlier nanosecond time-resolved studies [60, 34, 96], numerous theoretical predictions [97, 42], and x-ray diffraction measurements of the liquid pair correlation function near the melting point [98, 32]. Liquid carbon is an important material to understand in astrophysical models of Uranus and Neptune [77], but so far experiments have been largely inconclusive on most of the properties of the liquid due to the difficulties imposed by its high melting point and volatility. Time resolved XAS measures the electronic bonding structure of liquid carbon, providing a direct experimental check of molecular dynamics models [105]. The techniques developed are general, and they can be extended to study a variety of other materials at even higher temperatures than those that have already been explored.

## Chapter 2

# Experimental apparatus

This chapter provides a description of the experimental setup used to conduct the time-resolved x-ray absorption measurements reported in chapters 3 and 4. In general, the apparatus can be divided into three components: a synchrotron bend magnet, a femtosecond laser system, and the x-ray beamline endstation where the experiments are actually performed.

### 2.1 Synchrotron x-ray source

These experiments were performed at bend magnet beamline 5.3.1 of the Advanced Light Source (ALS) at Lawrence Berkeley National Laboratory in Berkeley, California. The ALS is an electron storage ring built explicitly as a source of high-brightness electromagnetic radiation that ranges from the infrared to hard x-rays. Figure 2.1 is a simplified drawing of the ALS layout. A 50 MeV linac inside the actual storage ring

performs the initial acceleration of electrons, which then enter a “booster” ring which brings the energy of the beam to 1.5 GeV. The electrons are then injected into the main storage ring, where they are kept for several hours before scattering processes cause significant losses in the stored current and necessitate another injection. RF cavities within one of the straight sections of the ring compensate for radiative energy losses and offer the ability to further accelerate the stored beam to 1.9 GeV, currently the preferred mode of operation at the ALS since it offers higher brightness radiation for x-ray photon energies above 1 KeV. Although one of the distinguishing features of the ALS is the use of straight sections of the storage ring to generate very intense beams with arrays of magnets called “wigglers” and “undulators,” the work described uses the radiation emitted tangentially from the electron beam as it is bent by one of the high field-strength magnets that steer the beam in its path around the ring (i.e. a “bend magnet”).

### 2.1.1 Theory of bend magnet radiation

The basic physics of how bend magnets produce radiation is mathematically complex but well understood from relativity theory. From ref. [47], the differential form of the angular distribution of photon flux  $F$  from the magnet is given by

$$\frac{dF}{d\theta d\phi} = \frac{3\alpha}{4\pi^2} \gamma^2 \frac{\Delta\omega}{\omega} \frac{I}{e} y^2 (1 + X^2)^2 \left[ K_{2/3}^2(\xi) + \frac{X^2}{1 + X^2} K_{1/3}^2(\xi) \right]. \quad (2.1)$$

See table 2.1 and figure 2.2 for definitions of the variables and functions used. Equation 2.1 contains several important features of bend magnet radiation, some of which

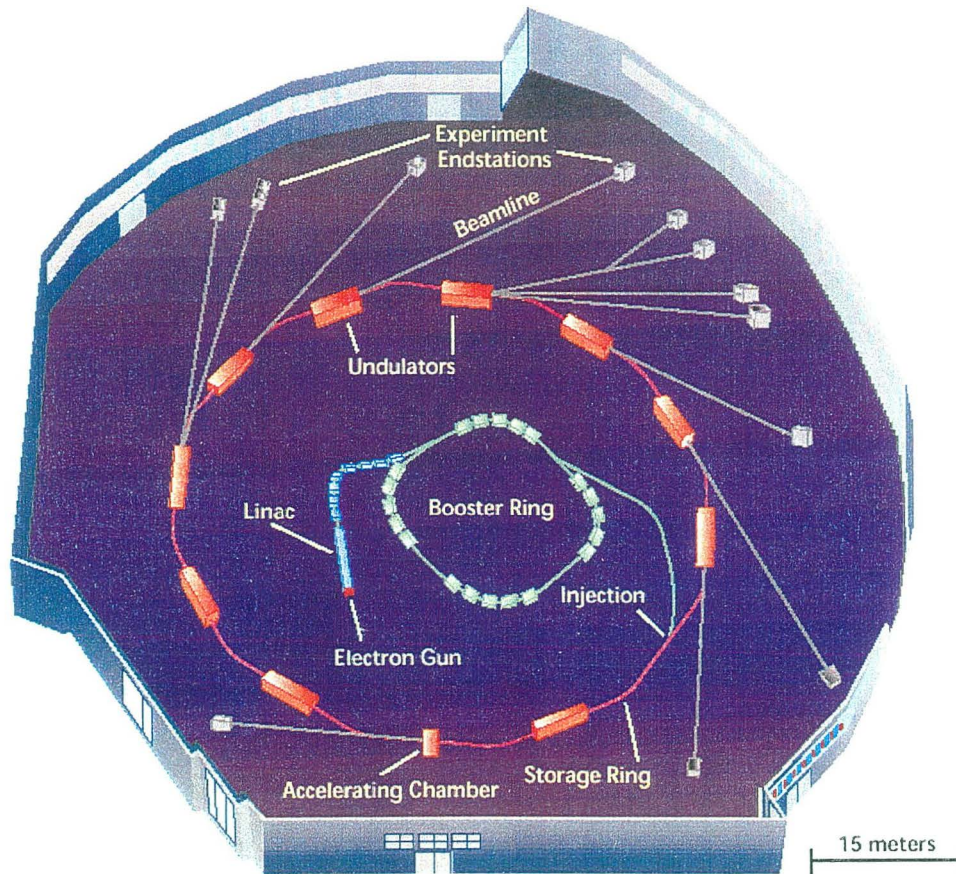


Figure 2.1: Overview of the Advanced Light Source. This picture is a modified version of one of the graphics available for public presentation (“Views You Can Use”) at <http://www.als.lbl.gov>.

we will now review.

The vertical angular dependence of the flux on  $\gamma\phi$  is plotted for various values of  $\epsilon/\epsilon_c$  in figure 2.3. Note that for photon energies  $\epsilon$  close to the critical energy  $\epsilon_c$ , the bend magnet emits radiation within an angular range roughly equal to  $1/\gamma$ . For ALS bend magnets during 1.9 GeV operation of the electron beam,  $\epsilon_c = 3$  keV and  $\gamma = 3700$ , so for soft x-rays ranging from 100 eV to 300 eV this vertical angular width is approximately 1–2 mrad. This is an important result, since it means that most of the radiation is confined to the plane of the storage ring, making it much easier to use grazing incidence optics to focus and steer x-rays onto the sample. For beamline 5.3.1, the first optic (a grazing incidence toroidal focusing mirror) has a vertical angular acceptance of 0.2 mrad, so it captures the central 10–20% of the beam at these energies.

This small vertical angle acceptance means that we can always make the simplifying assumption that  $X^2 = (\gamma\phi)^2 \ll 1$ . This allows us to write

$$\frac{dF}{d\theta d\phi} = \frac{3\alpha}{4\pi^2} \gamma^2 \frac{\Delta\omega}{\omega} \frac{I}{e} y^2 K_{2/3}^2(y). \quad (2.2)$$

If we set  $\Delta\omega/\omega = 0.1\%$  and use the parameters of an ALS bend magnet during 1.9 GeV operation of the storage ring at a current  $I = 400$  mA, figure 2.4 shows a plot of the flux as a function of photon energy. Note that the bend magnet provides significant flux over a very broad spectral range from 10 eV to more than 10 keV. These different photon energies are emitted simultaneously, without the need to tune parameters of the source. As we will see later, this is a critical quality of bend magnet

Symbol	Meaning
$F$	Number of photons per second (flux)
$\theta$	Angle in plane of electron orbit (horizontal)
$\phi$	Vertical observation angle
$\alpha$	Atomic fine structure constant ( $\approx 1/137$ )
$\gamma$	Ratio of electron total energy to rest energy
$\omega$	Frequency of photon in rad/s
$I$	Current of stored beam
$e$	Charge of electron = $1.602 \times 10^{-19}$ C
$y$	$\omega/\omega_c$
$\omega_c$	“Critical frequency” = $3\gamma^3 c/2\rho$
$\rho$	Radius of curvature of electron beam = $3.3E^2 B(\text{m}/\text{TGeV}^2)$
$E$	Energy of electron beam
$B$	Strength of magnetic field
$\epsilon_c$	$\hbar\omega_c$
$X$	$\gamma\psi$
$\xi$	$y(1 + X^2)^{3/2}/2$
$K_\nu$	Modified Bessel function of the second kind

Table 2.1: Explanation of symbols and functions used in equation 2.1.

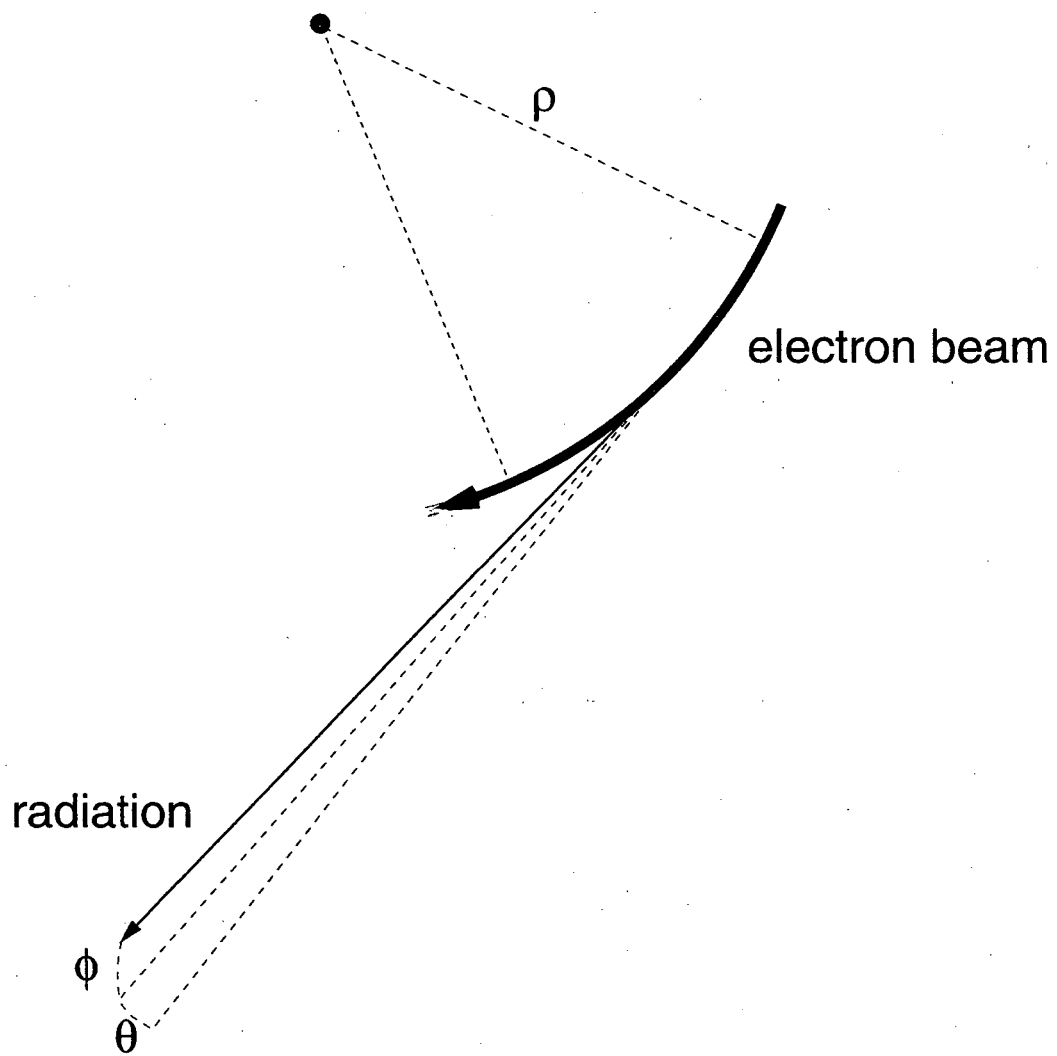


Figure 2.2: Sketch of radiation emitted by a curved electron path.

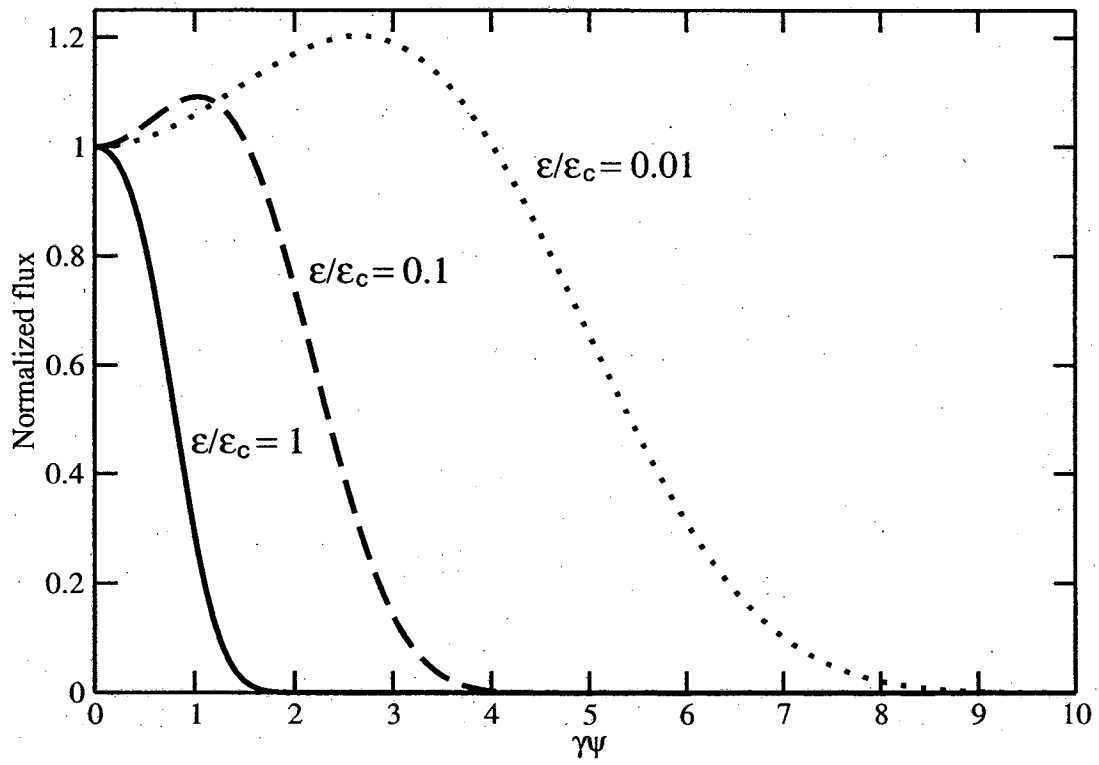


Figure 2.3: Plot of the vertical angular dependence of photon flux for some values of  $\epsilon/\epsilon_c$ .

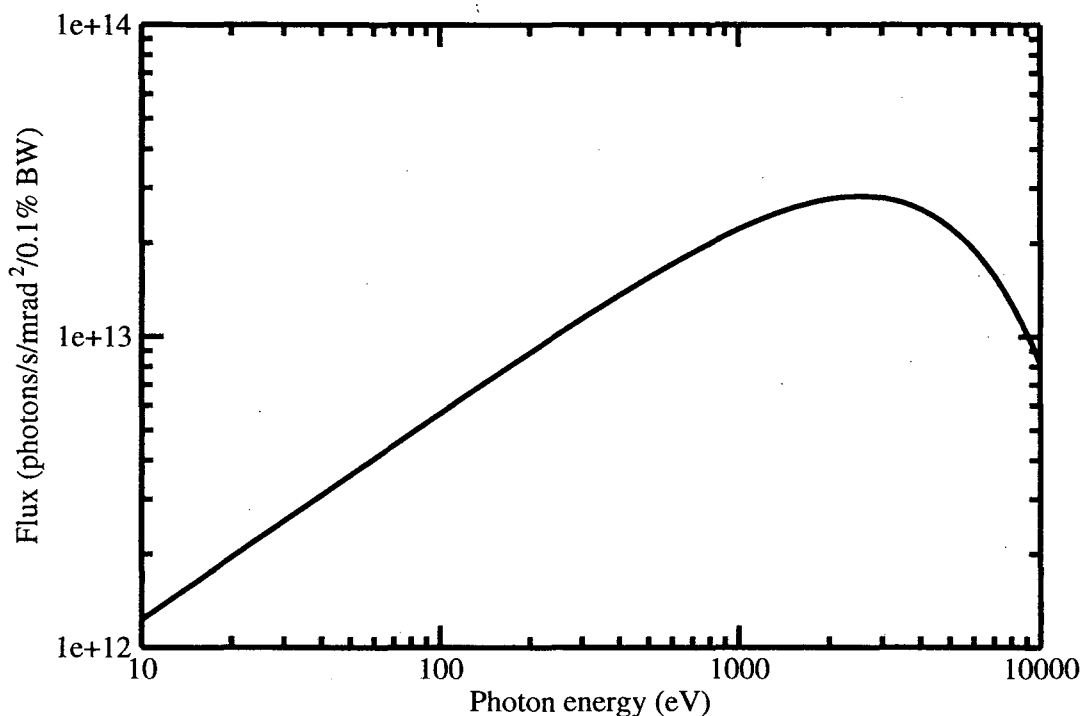


Figure 2.4: Spectral distribution of photon flux for ALS beamline 5.3.1.

radiation which the experiment exploits to a tremendous advantage.

### 2.1.2 Timing structure of the x-ray pulses

The timing characteristics of the x-rays match those of the stored electron beam. The RF system of the ALS storage ring supports a total of 328 possible electron bunch positions (called “buckets”), equally spaced around the ring. Usually, most of these buckets are filled with electrons, except for a short gap of about 40–50 consecutive empty buckets. The purpose of this gap is to clear the beam of ions that are attracted by the negative charge of the electrons, although the exact duration of the gap is flexible and can be tailored to accommodate user wishes. On request, one

bucket within this gap may be filled with a large number of electrons (up to 5 times as many as in the other filled buckets). Figure 2.5 shows a sketch of a typical ALS filling pattern, including this temporally isolated “camshaft” pulse. The ALS also runs for a few weeks each year in so-called “double bunch” mode, where only two buckets in the ring are filled to very high levels. This mode is primarily for experiments that use time-of-flight techniques that are incompatible with the normal operation of the ALS, but it is also extremely useful for time-resolved measurements.

The fine timing structure of the individual electron bunches is set by various parameters of the ring and by the number of electrons in the bunch, with more electrons causing longer bunch lengths (and faster decay rates) due to electron-electron scattering within the bunch. In particular, the ALS has recently installed passive “third harmonic” RF cavities, designed to increase the bunch length of the closely spaced series of electron pulses (the “multibunch train”) that comprises the majority of current in the ring. Usually the pulse duration of these pulses is roughly 50 ps. The camshaft pulse is normally longer than this, ranging from 70 ps immediately after injection (at 10 mA current) and approaching 50 ps as the stored electron beam decays for several hours. Visible light streak camera measurements of radiation from a diagnostic beamline show a roughly Gaussian temporal profile for the electron pulses [18], in agreement with the streak camera measurements of the x-ray temporal profile performed at beamline 5.3.1 that will be discussed later.

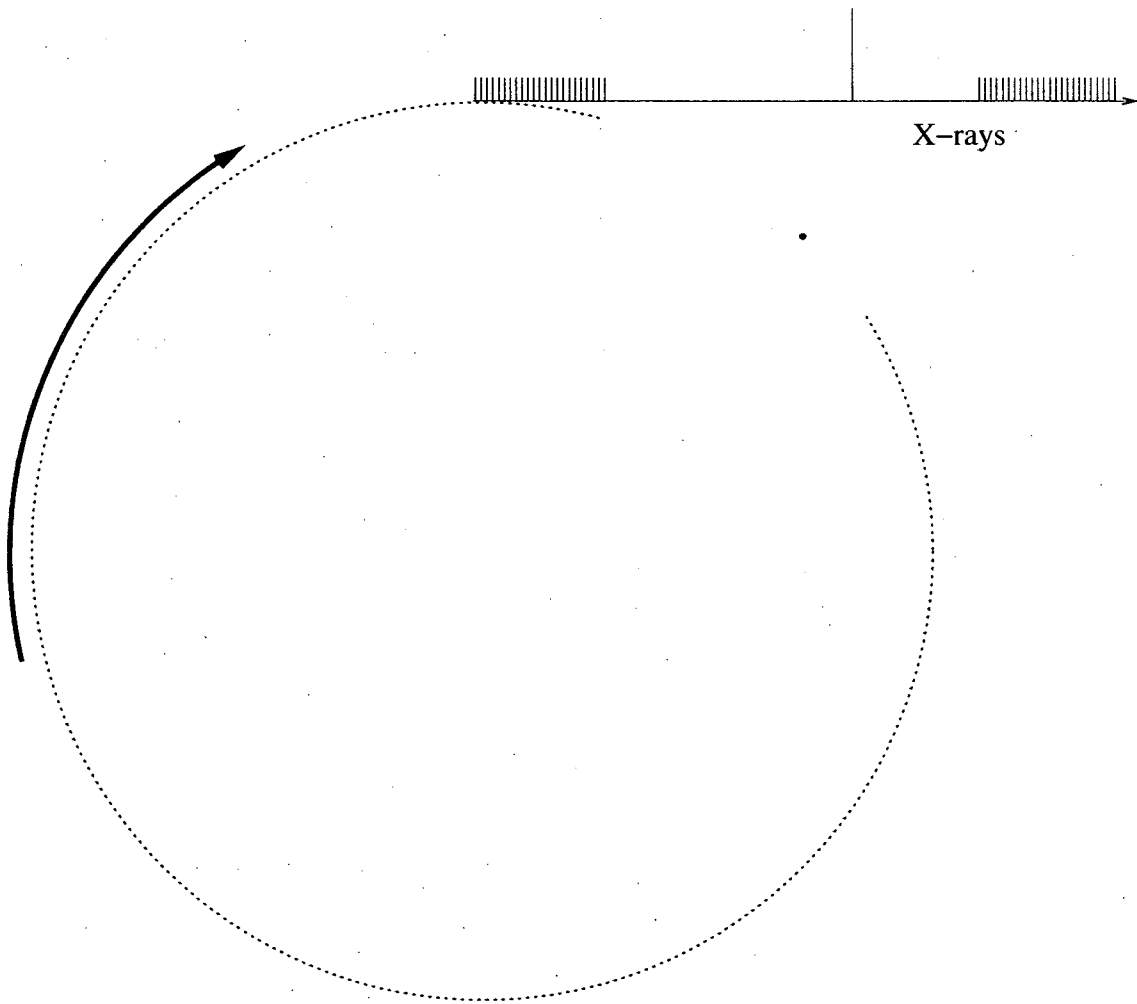


Figure 2.5: Pictorial sketch of a typical electron bunch timing mode at the ALS

## 2.2 Femtosecond laser system

The laser system consists of two discrete parts, a femtosecond oscillator and a set of optical amplifiers that work on the principle of chirped-pulse amplification (CPA). Although the details of these laser systems are well known and widely used in many laboratories, we have made several changes to the system to accommodate synchronization to the storage ring. What follows is a brief review of the basic components of the laser system, with special emphasis on these modifications that make time-resolved measurements with synchrotron x-rays possible.

### 2.2.1 Oscillator

The femtosecond oscillator is a Kerr-lens mode-locked system, purchased as a kit (model TS) from Kapteyn-Murnane Laboratories, L. L. C. and based on the system described in ref. [85]. Figure 2.6 shows a sketch of the components and the beam path. A diode-pumped “Millennia” laser from Spectra-Physics provides approximately 4 W of CW power at 532 nm that is focused onto a Ti:Sapphire crystal within the oscillator cavity. This crystal functions as both the gain medium and as the mechanism for passive mode locking that gives rise to the short, 50 fs output of the system. The theory behind this kind of mode-locking is involved and beyond the scope of this work; see ref. [39] for a complete explanation of the current understanding of this phenomenon. Besides the Ti:Sapphire crystal, the cavity contains a pair of prisms to compensate for the group velocity dispersion induced by the crystal. The prisms

are mounted on translation stages, useful for tuning the dispersion compensation and for causing the impulsive perturbation to the cavity alignment needed to start mode-locking. The optical path length for one round-trip through the oscillator cavity is 3.6 m, making the output of the oscillator a continuous train of  $\sim 3$  nJ pulses spaced apart by 12 ns. The flat end mirror of the oscillator cavity is mounted on a piezoelectric crystal to allow very fast and fine tuning of the length of the oscillator cavity, important for synchronization of the laser to the ALS electron bunches as we will now discuss.

The first major step to achieve synchronization to the storage ring is to force the oscillator pulses to occur at a fixed phase with respect to the 500 MHz RF signal that controls the spacing of buckets in the ring. Figure 2.7 shows a block diagram of how this is done. The design is essentially a type I phase-locked loop (described in the general case by ref. [40]) with the laser oscillator functioning as the “voltage-controlled oscillator” (VCO). A thin glass window placed in the oscillator output path diverts a small portion of the beam into a fast silicon diode ( $\sim 1$  ns rise time). This diode signal is then sent through a 500 MHz bandpass filter (Texscan, model 3BC500) that isolates the 6th harmonic of the 12 ns period pulse train. This signal then gets amplified by a 30 dB RF amplifier (Minicircuits, model ZKL-2R5) and fed into one of the inputs of an RF mixer.

The other input to the mixer is derived from the synchrotron 500 MHz RF clock. Before entering the mixer, the synchrotron RF passes through an I-Q vector modu-

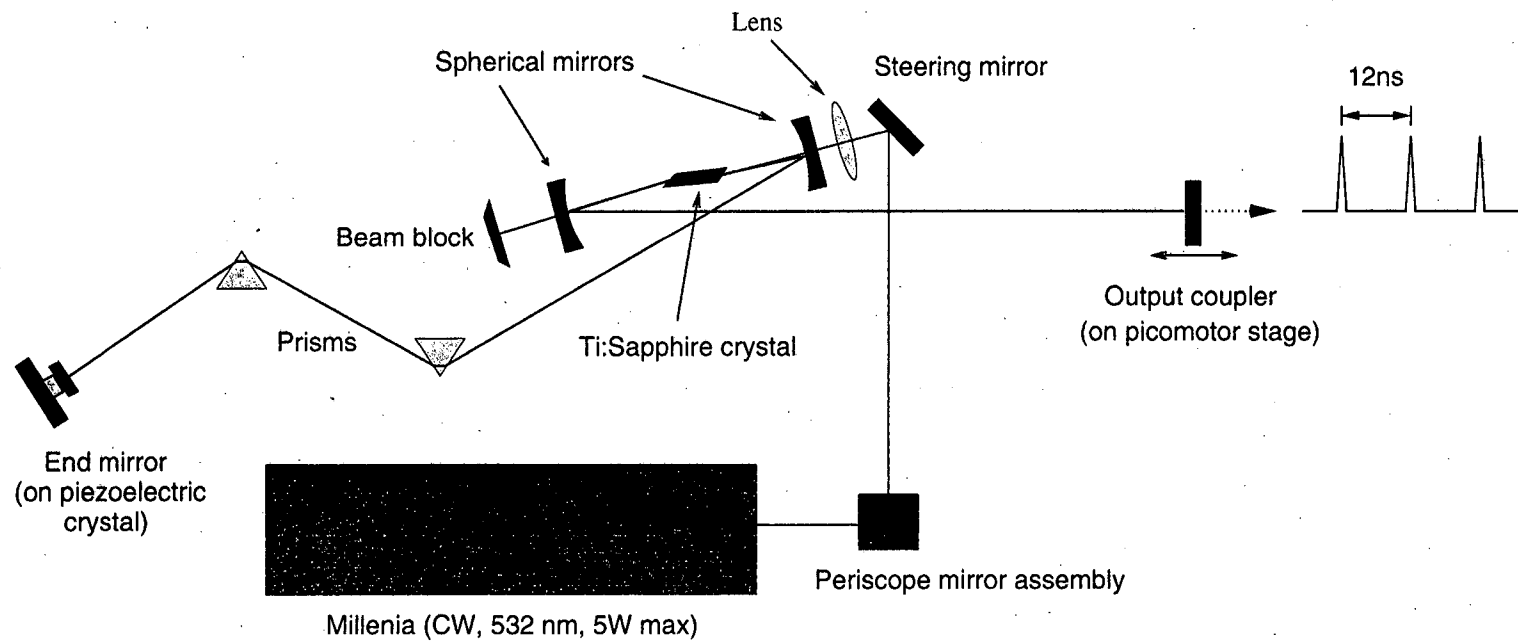


Figure 2.6: Sketch of oscillator beam path.

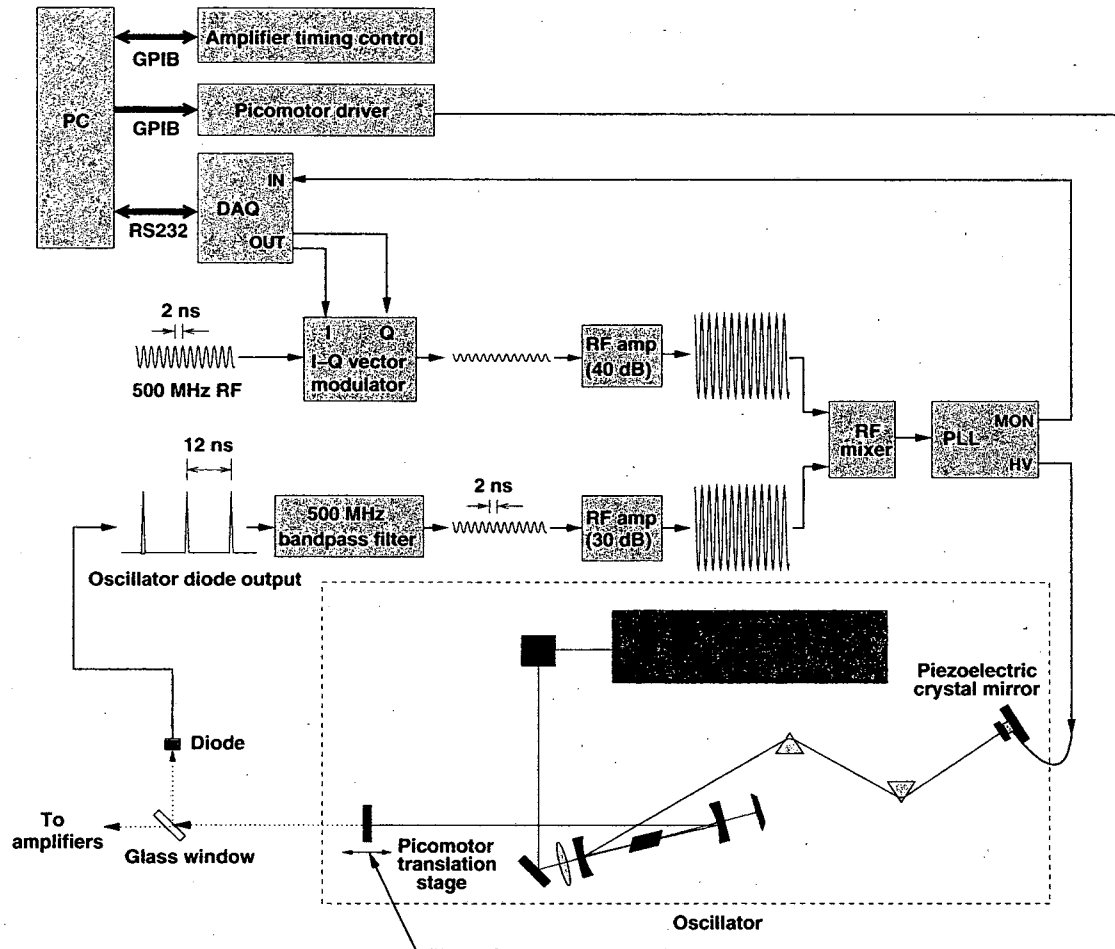


Figure 2.7: Block diagram of oscillator synchronization. Two steering mirrors between the oscillator output coupler and glass window have been omitted for simplicity.

lator (I. F. Engineering, model QPMX-499). The purpose of this device is to provide a means of electronically varying the phase of the RF arbitrarily, thus facilitating control over the relative timing of the oscillator and x-ray pulses. See appendix A for a description of how this works. The I-Q modulator attenuates the RF by approximately 15 dB, so to reach an amplitude comparable to that of the oscillator-derived mixer input (approximately 100 mV peak-to-peak), the signal is amplified by 40 dB using a Minicircuits ZKL-1R5 RF amplifier. This signal is then sent into the mixer, which outputs the difference frequency of the oscillator 6th harmonic and the phase-shifted synchrotron RF signal, or (if the frequencies are exactly equal) a constant voltage related to the relative phase of the two inputs. This signal then enters a phase locked-loop interface circuit (labeled "PLL" in figure 2.7), which sends this difference frequency signal through a low-pass amplifier (cutoff  $\sim 100$  KHz) and then uses it to create a high-voltage transverse bias to the piezoelectric crystal end mirror of the oscillator cavity. This bias changes the length of the crystal and therefore the oscillator cavity by an amount proportional to the instantaneous phase difference between the oscillator pulses and the synchrotron RF. This change in the oscillator cavity length causes a change in the frequency of the output pulses, completing the feedback loop. The loop works to create a stable phase and frequency lock between the oscillator and synchrotron bunch timing with a jitter estimated at less than 10 ps [52]. This timing precision is acceptable, since the duration of the x-ray pulses is considerably longer ( $\sim 70$  ps).

Although this technique of using the piezoelectric crystal to perform small adjustments to the cavity length works well to correct short time-scale deviations in the relative timing between the oscillator pulses and the synchrotron bunches, the short range of motion available to the crystal (only  $10\ \mu\text{m}$ ) will cause the loop to fail if the cavity length changes by a larger amount due to thermal expansion or contraction. The cavity length is approximately 1.8 m, so a  $10\ \mu\text{m}$  expansion would correspond to a fractional change of  $6 \times 10^{-6}$ . Since typical thermal expansion for  $1\ ^\circ\text{C}$  temperature changes near room temperature is also of this magnitude, relying on the piezoelectric crystal alone to control the cavity length will fail unless we can impose very precise (and difficult) temperature stabilization of the area around the oscillator.

To remedy this, we mounted the output coupler of the oscillator on a motorized translation stage and set up a slow auxiliary feedback loop to correct for the gradual changes in cavity length that result from temperature variation. We elected to use a NewFocus “picomotor” translation stage because it offers very small discrete motion steps over a wide range, without the need for power to be sent to the motor to hold its position [65]. The driver for the translation motor, a NewFocus 8732 Multi-Axis Driver, is controlled by computer via GPIB (General Purpose Interface Bus). A program continuously running on the computer uses an SRS245 DAQ module (from Stanford Research Systems) to read an analog signal that monitors the voltage level applied to the piezoelectric crystal. If this signal indicates that the crystal is near one end of its range, the program attempts to correct for this by moving the output

coupler. For the source code, please see appendix E.3. The range of motion for the picomotor stage is longer than 1 inch, giving ample allowance for thermal effects on the cavity length.

### 2.2.2 Amplifiers

To amplify the 3 nJ oscillator pulses to the  $\sim 1$  mJ energy levels sufficient to melt solids over a 400  $\mu\text{m}$  diameter spot, we require several stages of amplification based on the principle of chirped-pulse amplification (CPA). Since straightforward amplification of femtosecond pulses would result in self-focusing and damage to crystals and other optics at fairly moderate pulse energies, all the amplification is done with pulses that are “stretched” in time to  $\sim 100$  ps by forcing different wavelength components of the pulse to be delayed by slightly different times. Later, after amplification, the process is reversed and the femtosecond pulse is reconstructed, but now with a much higher energy. For more details, see ref. [89]. Figure 2.8 shows a sketch of the stretcher and compressor used in our system, featuring a pair of matched diffraction gratings that create wavelength-dependent path lengths for the beam.

Between the stretcher and compressor there are three stages of amplification: a regenerative amplifier, a 1 KHz repetition rate two-pass amplifier, and a 10 Hz repetition rate two-pass amplifier. The regenerative amplifier is the primary amplification stage; of the remaining two, only one amplifier can be used at any time. The main differences between the two types of two-pass amplifiers are the maximum repetition

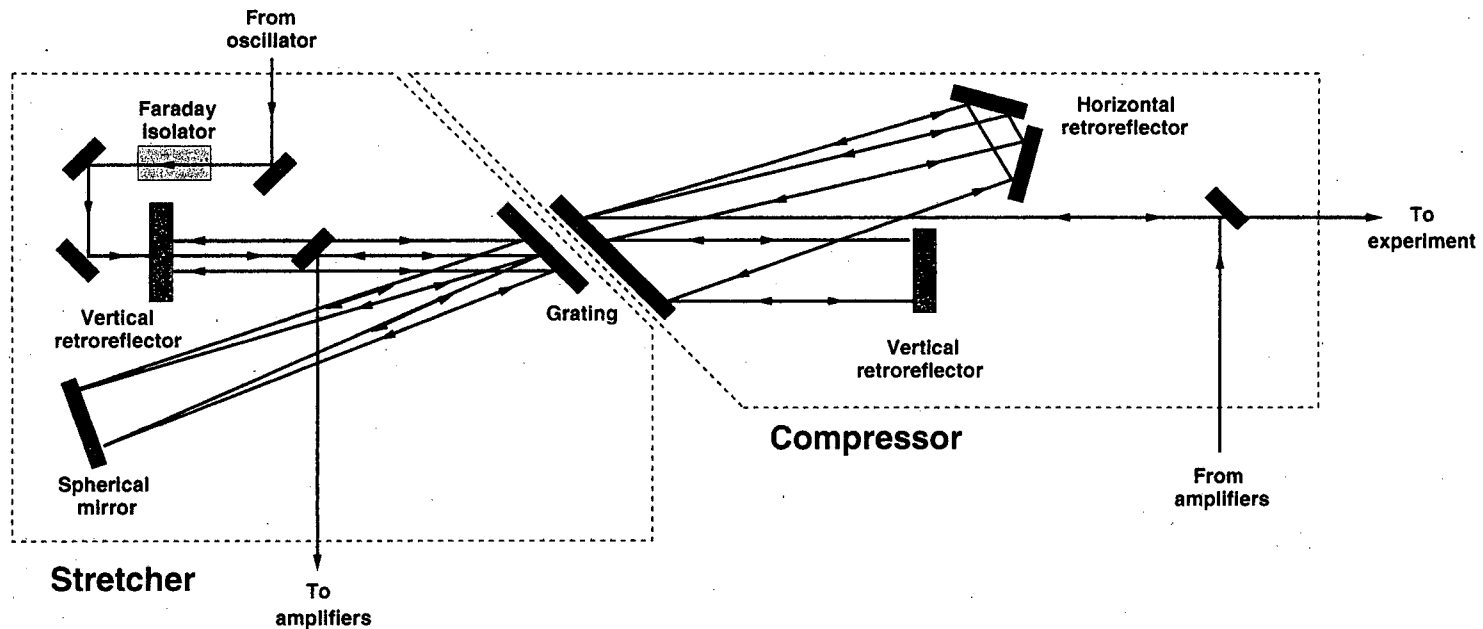


Figure 2.8: Sketch of the stretcher/compressor pair for CPA. The wavelength-dependent portions of the beam path are represented by red and blue lines indicating longer and shorter wavelengths, respectively. In several places in the drawing the beam appears to retrace itself, but in fact this is only because the top-down view shown does not accurately depict vertical displacements of the beam caused by the slightly off-axis spherical mirror and the vertical retroreflectors.

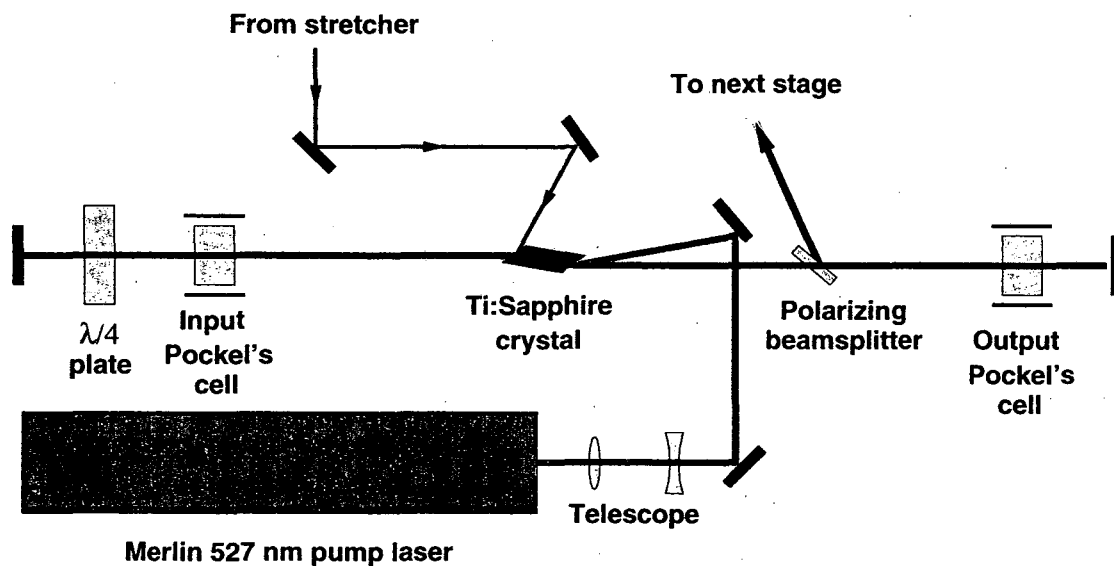


Figure 2.9: Sketch of the regenerative amplifier.

rate and the magnitude of the amplified pulse energies: for the 1 KHz system the maximum pulse energy output (after compression) is 2 mJ, and for the 10 Hz system pulse energies of more than 10 mJ have been measured.

### Regenerative amplifier

Figure 2.9 is a sketch of the important aspects of the regenerative amplifier. The basic idea behind this kind of amplifier is simply to select individual pulses from the oscillator pulse train and amplify them at much as possible.

The selection process is achieved by an electro-optic crystal known as a Pockel's cell. From the stretcher, s-polarized pulses enter a resonant laser cavity (called the "regen cavity") via reflection from an angled face of a Ti:Sapphire crystal. First, we will consider the fate of pulses that arrive *before* the pulse that we choose to amplify.

In the “off” state (i. e. no voltage is applied to the cell), the optic labeled “input Pockel’s cell” acts as a simple transmission optic, doing nothing to the polarization of the beam. In this case the beam passes twice through the  $\lambda/4$  plate, becoming p-polarized as it passes through the Ti:Sapphire crystal. Since all the intracavity optics on the right side of the crystal in the drawing are transmissive to p-polarized light (provided the Pockel’s cell there is also “off”), the pulse returns through the crystal, passes again through the (still inactive) Pockel’s cell, gets rotated into s-polarized light by the two passes through the  $\lambda/4$  plate, and gets ejected from the cavity mostly due to reflection from the polarizing beam splitter. The pulse has received very little amplification since it made only two passes through the crystal.

Now we consider a pulse that we do want to amplify, presumably at some time soon after the 1 KHz Merlin Nd:YLF pump laser (10 W,  $\lambda = 527$  nm) has excited the Ti:Sapphire crystal in the cavity. The input Pockel’s cell is initially off as the pulse enters the cavity and makes its double pass through the left hand side of the cavity. Immediately after the pulse leaves the input Pockel’s cell (heading toward the right hand end mirror), voltage is applied to the cell, causing the cell to behave as another  $\lambda/4$  plate and canceling the effect of the permanent  $\lambda/4$  plate. The pulse is then “trapped” inside the cavity, since it is always p-polarized when traveling through optics with a transmission sensitive to the polarization of the beam. The pulse now makes about 10 round-trips through the cavity, getting amplified by a factor of 2–3 each time until it reaches a saturation level. Note that any oscillator pulses that try to

enter the cavity while the Pockel's cell is active will be quickly ejected from the cavity after only one pass through the crystal, since s-polarized light will be immediately reflected by the polarizing beamsplitter (and, to a lesser extent, the Brewster-angle cut face of the crystal itself).

When the pulse has been amplified to saturation, a second Pockel's cell (labeled "output Pockel's cell") is activated while the pulse is on the left hand side of the cavity, causing a polarization rotation as it travels to the right and bounces off the end mirror. Now the pulse is s-polarized as it hits the polarizing beamsplitter from the right, causing the pulse to be reflected out of the cavity.

### **1 KHz two-pass amplifier**

All of the reported experiments on liquid silicon use the 1 KHz two-pass amplifier to further boost the energy output from the regenerative amplifier, since the 10 Hz stage (more appropriate for these essentially single-shot experiments) was only recently added to the system. Figure 2.10 shows a sketch of the beam path in this amplifier. The pulse, after being focused somewhat by a lens, passes twice through a Ti:Sapphire rod that has been excited by a second Merlin pump laser (operated at 15 W). The beam then enters the compressor, resulting in femtosecond pulses with a maximum pulse energy of 2 mJ.

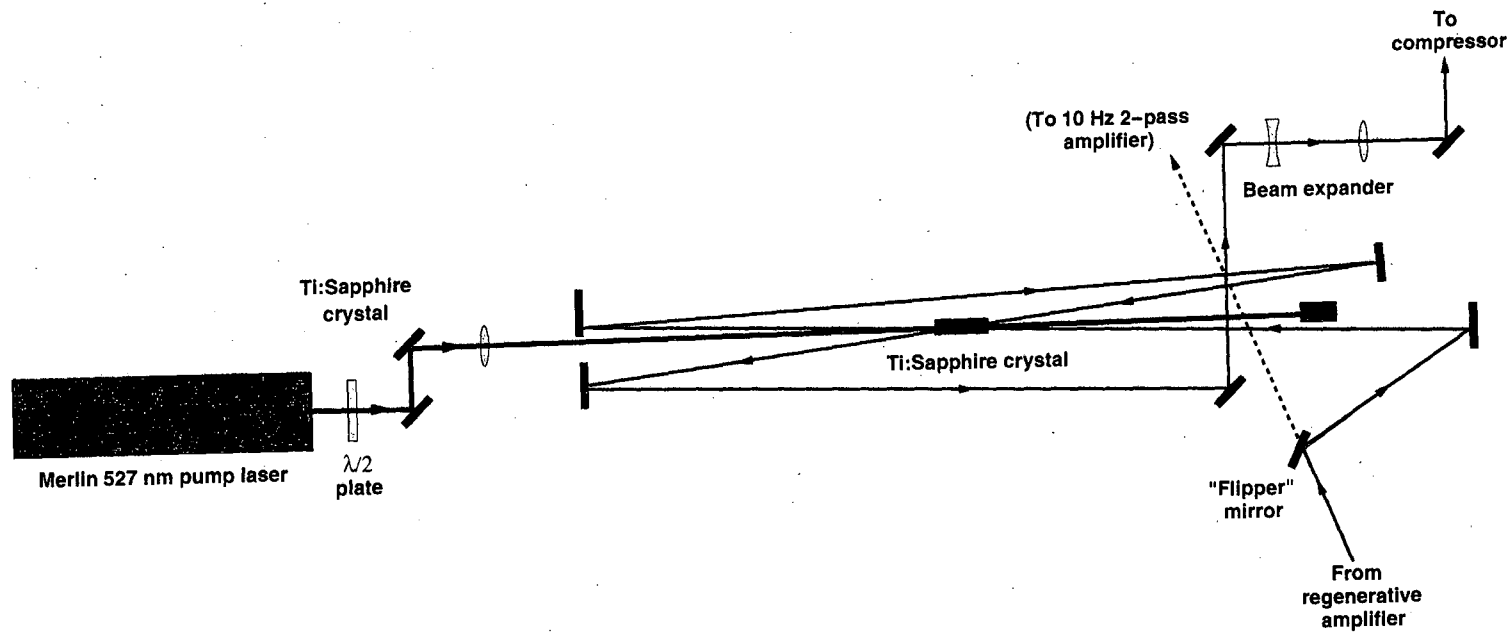


Figure 2.10: Sketch of the 1 KHz two-pass amplifier stage.

## 10 Hz two-pass amplifier

Rather than entering the 1 KHz two-pass amplifier, the output pulses from the regenerative amplifier can be diverted into a different amplifier stage that operates at a maximum repetition rate of 10 Hz but results in potentially much higher amplification. Figure 2.11 shows a sketch. The idea is similar to that of the 1 KHz system, only here the pump laser is a 10 Hz Quanta-Ray YAG laser, with  $\sim 500$  mJ pulse energies at 532 nm. Poor mode quality from this pump laser currently limits the amplification efficiency, resulting in approximately 11 mJ energies for femtosecond pulses after the compressor.

## Amplifier timing

The issue of properly timing the pump laser firing and Pockel's cell timings to allow proper operation of the amplifiers in x-ray experiments is fairly complicated and is explored further in appendix A and in section 2.4. At this point it is appropriate to point out that, although the phase-locked loop of section 2.2.1 synchronizes the pulse train of the oscillator to the 500 MHz storage ring clock, for experiments we need to synchronize the total amplified laser output to the camshaft pulse. Since the time for electrons to orbit the storage ring is 656 ns, we need to make sure that the pulses from the oscillator that we select to amplify are all at a fixed time delay with respect to a 1.52 MHz "roundtrip" clock that indicates the timing of the camshaft pulse. Because the least common multiple of the oscillator pulse train period (12 ns)

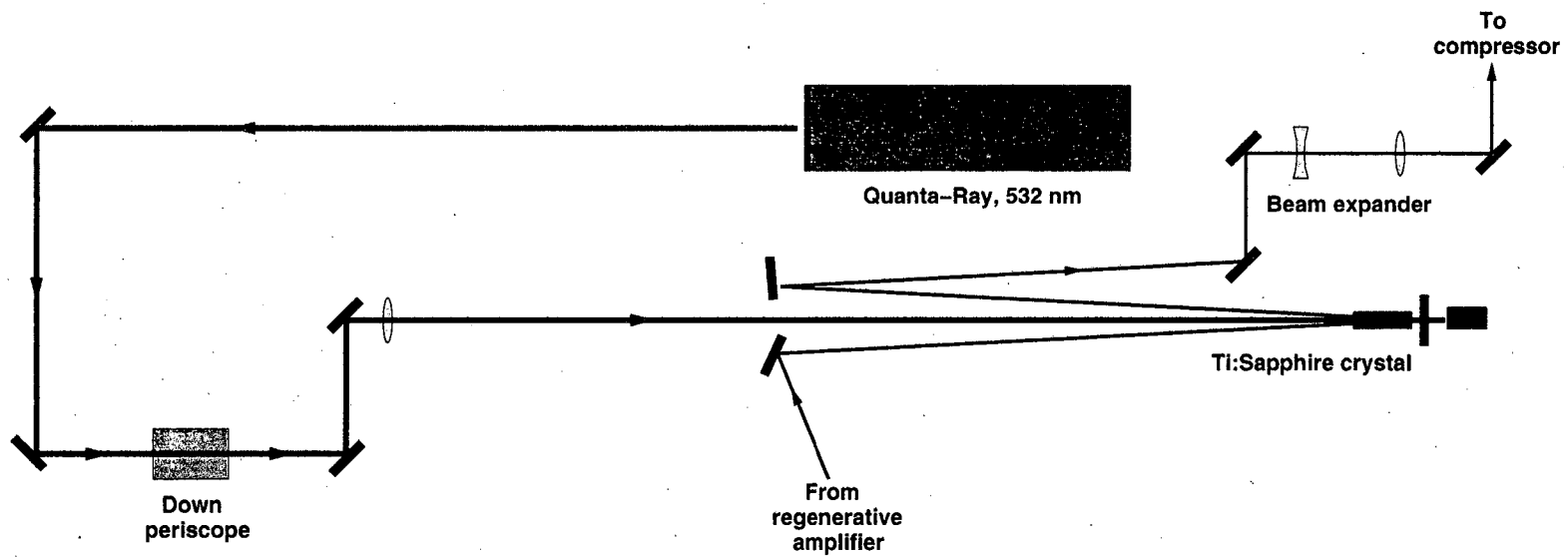


Figure 2.11: Sketch of the 10 Hz two-pass amplifier stage.

and this roundtrip clock period (656 ns) is 1968 ns, we need to divide the roundtrip clock by three and use some signal synchronous with the resulting 510 KHz clock to trigger the amplifier pump lasers and Pockel's cells. Figure 2.12 is an attempt to illustrate this fact by showing that the oscillator pulse timings are at a fixed delay with respect to every third leading edge of the synchrotron roundtrip clock.

## 2.3 Beamline endstation

The actual time-resolved x-ray absorption experiments are carried out within an interlocked radiation hutch at beamline 5.3.1. Figure 2.13 shows a sketch of the relevant beamline apparatus. All the components are enclosed in vacuum chambers, with pressures ranging from  $1 \times 10^{-6}$  torr near the sample to  $1 \times 10^{-8}$  torr at the focusing mirror (a differential pump between this mirror and the chopper is not shown in the figure).

Initially, a broad spectrum of x-rays strike a grazing incidence, Pt-coated toroidal focusing mirror. This mirror is bent and tilted with respect to the beam so as to project a 1:1 image of the electron beam onto the sample position. The size of the focused spot is currently  $250 \mu\text{m}$  horizontally and  $150 \mu\text{m}$  vertically, the vertical size limited by slope errors in the mirror. The experiments on liquid silicon used an older version of this mirror with a vertical focus size of  $250 \mu\text{m}$ .

After reflecting from the mirror but before hitting the foil, the x-rays pass through a number of obstacles designed to reduce the flux of unnecessary photons that would

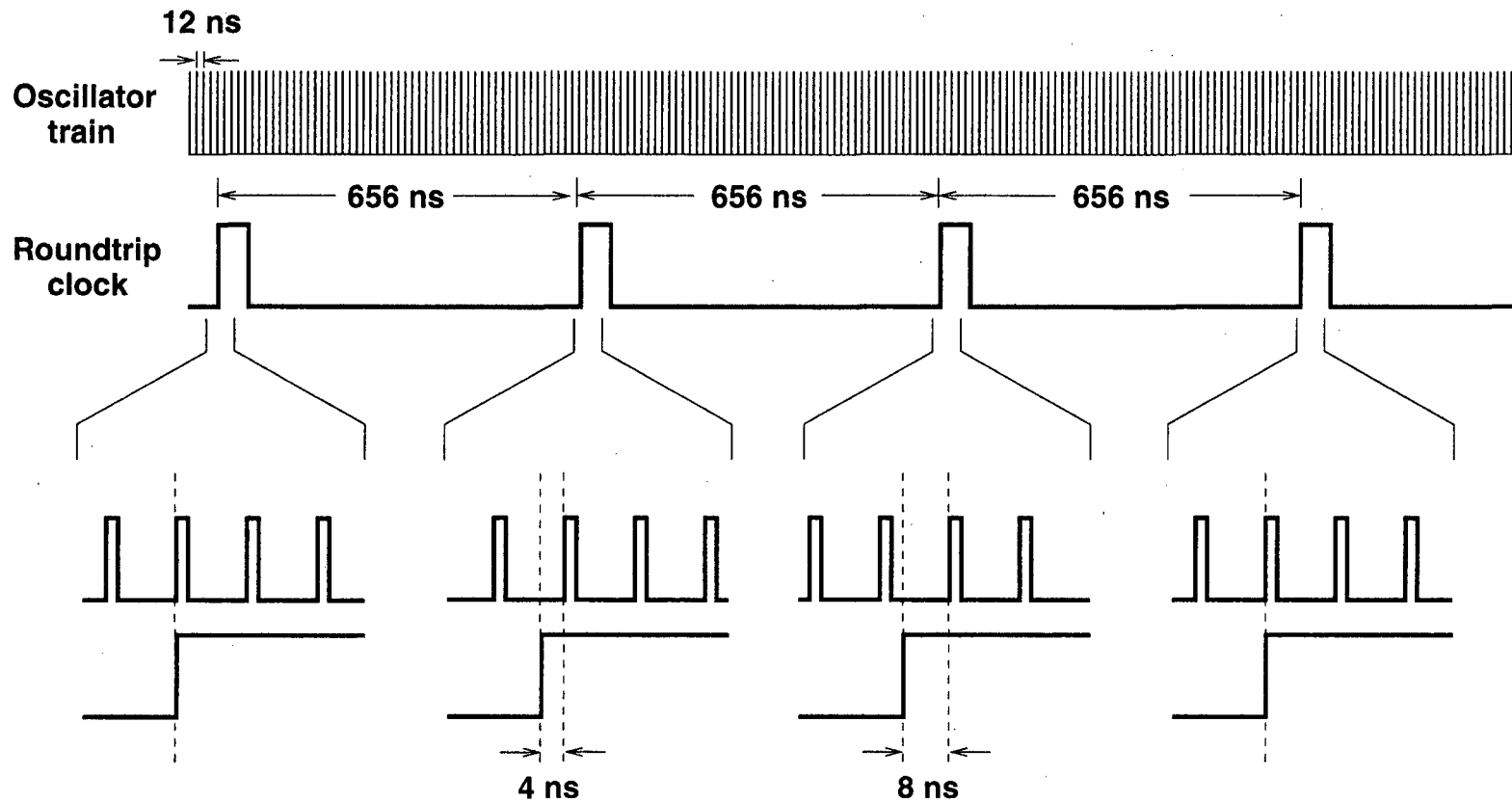


Figure 2.12: Timing diagram showing the (phase locked) oscillator pulse train versus the synchrotron roundtrip clock.

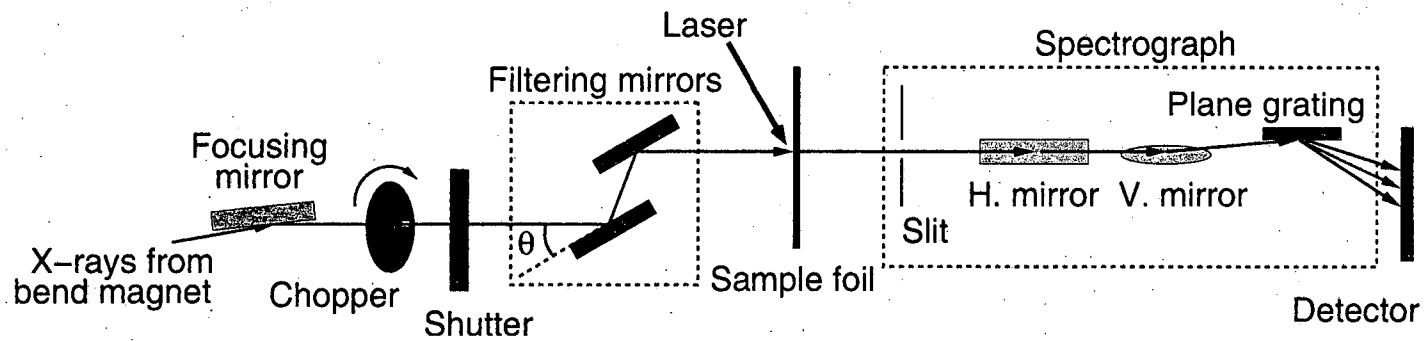


Figure 2.13: Sketch of absorption experiment at beamline 5.3.1. The x-ray reflection angles are exaggerated for illustrative purposes, and the figure has been slightly tilted to make the beam after the toroidal focusing mirror appear to be horizontal (when it is actually angled down by  $\sim 2$  mrad).

otherwise damage downstream components or contribute unwanted high-order intensity to the spectra. First, the x-rays pass through a chopper. The chopper consists of a thin metal disk thick enough to be opaque to the majority of photons emitted by the bend magnet, but with narrow slots to allow x-rays to pass through periodically as the chopper rotates at a fixed frequency. The opening time for one pass through a slot on the wheel is typically  $40 \mu\text{s}$  for the slot widths and rotation frequencies used in the experiments. The idea behind the chopper is to reduce the average photon flux through the rest of the beamline without sacrificing flux from the x-ray pulses that are actually used in the experiment. While important for the experiments on liquid silicon, this is absolutely critical for the carbon experiments because at the relatively high vacuum pressures used for components downstream of the toroidal mirror, a few seconds of continuous beam from the synchrotron causes a chemical reaction with the residual gasses in the vacuum chamber to create significant amount of soot-like carbon deposits on the reflective components of the apparatus. For the silicon measurements, we used a 6-slot wheel pattern to chop the x-rays at a repetition rate of 1 KHz; for the carbon experiments, we used a single-slot pattern to chop the beam at 100 Hz. A pair of optical diodes mounted on the rim of the wheel provides an electronic monitor of the chopping frequency that we use to control the timing of the experiment.

After the chopper, the x-rays encounter an electronically controlled mechanical shutter. The shutter is there to further limit unnecessary flux on the rest of the

apparatus, so it is open only when data is being collected. For the carbon experiments, we coordinate the opening time of this shutter (which takes  $\sim 5$  ms) with the rotation of the chopper wheel to ensure that exactly one  $40 \mu\text{s}$  chopper “window” comes through the shutter at a time.

The x-rays that survive the shutter are then forced to reflect from a pair of flat mirrors which serve as a low-pass energy filter to eliminate photons that would otherwise contribute to higher-order reflections in the grating spectrograph, confusing the shape of the first-order spectrum that we want to measure. The basic principle behind this is the dependence of the critical angle of reflection on energy in the soft x-ray range. For the s-polarized light from the bend magnet, the specular reflectivity of a smooth surface from Fresnel’s equations is simply

$$R = \frac{4\pi^2}{\lambda} \left| \frac{\cos \theta - \sqrt{n^2 - \cos^2 \theta}}{\cos \theta + \sqrt{n^2 - \cos^2 \theta}} \right|^2, \quad (2.3)$$

where  $\theta$  is the incidence angle and  $n$  is the complex index of refraction. If  $n$  were real (i.e. the material is non-absorbing) and  $n < 1$  (typical for the real part when  $\lambda < 400 \text{ \AA}$ ), we see that for angles  $\theta$  less than the “critical angle”  $\theta_c(\lambda) = \text{acos}(n^2)$ ,  $R = 1$  and the material is perfectly reflective (total external reflection). Since the real part of  $n - 1$  approaches 0 quadratically in  $\lambda$  as  $\lambda \rightarrow 0$ , reflection of a broad spectrum of radiation at a fixed angle  $\theta$  allows longer wavelength radiation with  $\theta_c(\lambda) > \theta$  to reflect, but shorter wavelength (higher photon energy) radiation does not. This analysis gets somewhat more complicated when we consider that real mirror materials are actually very absorbing in the soft x-ray range, but the qualitative result is the

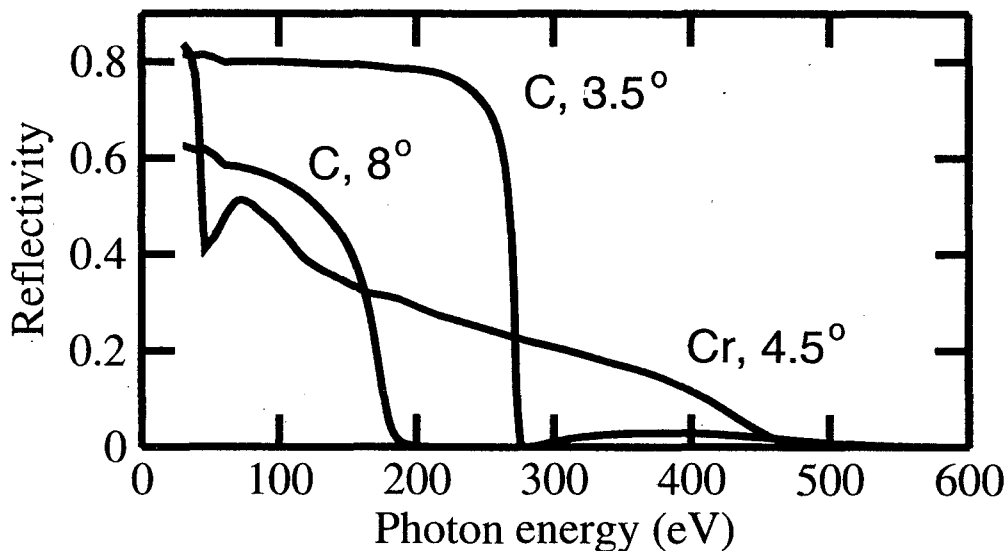


Figure 2.14: Reflectivity of filtering mirror pairs as a function of photon energy. The calculations assumed a 5 nm RMS surface roughness.

same: by setting the incidence angle appropriately, we can choose a low-pass “cutoff” photon energy for the reflected beam. For the silicon experiments, we chose to use carbon coated silicon wafers for the mirrors, and we used the angles  $\theta = 8^\circ$  (for a cutoff at  $\sim 150\text{eV}$  to study the Si  $L_{\text{II,III}}$  edge at 100 eV) and  $\theta = 3.5^\circ$  (to study the  $L$ -edge structure from 150 eV to 280 eV). The semi-empirical reflectivity for the mirror pair at these angles was calculated with ref. [36] and is plotted in figure 2.14, showing that the mirrors do an efficient job of reflecting the desired energy ranges while suppressing photon energies that might contribute to higher-order grating reflections. For the carbon experiment where we want to observe energies near the 285 eV carbon K-edge, we used a pair of chromium-coated silicon mirrors at  $4.5^\circ$ . The reflectivity for this mirror pair is also plotted in figure 2.14.

After reflection from the mirrors, the x-ray beam passes through a Ni mesh-

supported sample foil in the center of an approximately  $400\ \mu\text{m}$  diameter laser-heated region. The foils are typically  $500\ \text{\AA}$  thick, roughly the  $1/e$  absorption depth for both the x-rays and laser. The mesh wires form a grid for mechanical support of the foil, each  $\sim 5\ \mu\text{m}$  thick wire spaced by  $300\ \mu\text{m}$  from its neighbor. A single shot from the laser during the experiment will destroy the illuminated region, so the  $0.5'' \times 0.5''$  square foil is mounted on a motorized 3-axis manipulator that translates the sample within the plane of the foil so that we can perform the experiment on many different regions without breaking vacuum and replacing the sample. Typically, we can use one foil for approximately 200 laser shots. To measure the relative timing of the laser pulse and x-ray camshaft pulse on the sample, we measure the timing of both simultaneously on a 700 ps rise time x-ray photodiode placed at the sample position. This gives a measure of the absolute time delay between the laser and camshaft pulse. During the experiment (when the sample is in the beam), a fast 300 ps rise-time silicon photodiode monitors the timing of a small fraction of the laser pulse that leaks through a dielectric steering mirror, providing a permanent timing reference that we can compare with the timing of synchrotron pulses measured with another photodiode that looks at the visible-only light emitted from another bend magnet (5.3.4). This allows us to monitor continuously any changes in the the timing of the laser and x-ray camshaft pulses with an accuracy of approximately 100 ps.

A grating spectrograph analyzes the transmission of x-ray pulses through the foil. The spectrograph consists of an entrance slit, two curved refocusing mirrors, and

a grating. Appendix C discusses details of the focusing properties, efficiency and energy resolution of the spectrograph under conditions of the experiments. The most important result is that the spectrograph outputs an erect image of the slit spectrum at the back of the device, with reasonably high efficiency (2–20%) and moderate spectral resolution (1–2 eV).

A detector mounted on the back of the spectrograph images the entire spectrum from one x-ray pulse. The experiments described use two types of detectors, distinguished mainly by their temporal resolution. The primary detector is a set of two imaging-quality, 40 mm diameter gated microchannel plates (MCP's), coupled to a phosphor screen and a CCD camera. Figure 2.15 shows a sketch outlining the configuration of this device. X-rays initially strike the front of the plate and generate photoelectrons. A high electric field across the plate then accelerates these electrons into the small, microscopic channels of the MCP. Each time the highly energetic photoelectrons collide with the side of a channel, many more electrons are liberated from the inner channel coating. These electrons are also accelerated down the channel, creating still more electrons by collision with the channel walls. All these collisions result in a tremendous amount of signal gain, up to  $10^7$  at 2000 V bias. Electrons that emerge from the back of the MCP's hit the phosphor screen with high energy, causing the phosphor to glow with an intensity linearly related to the x-ray signal on the front of the MCP's. A set of optical fiber bundles couple this optical image of the x-ray spectrum onto a CCD chip, which digitizes the image and sends it to a computer. The

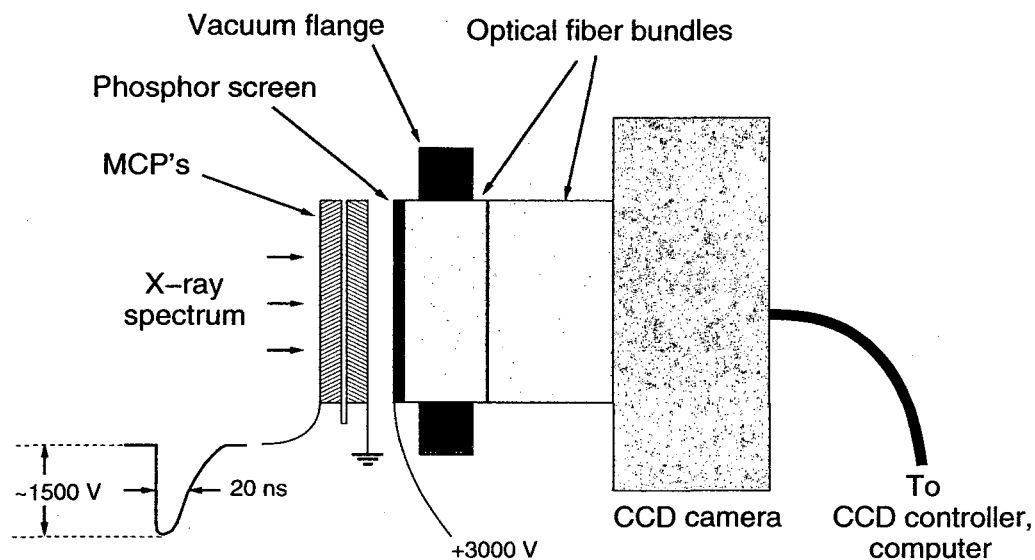


Figure 2.15: Sketch of MCP-based pump-probe detector, showing the configuration of electrical biases. The MCP's are mounted in a "Chevron" configuration, meaning that the angle of the channels is reversed as photoelectrons travel from the first to the second plate. The MCP's, phosphor screen and vacuum flange were purchased as a unit from Burle Scientific, Inc., and the fiber-coupled CCD camera is from Roper Scientific, Inc.

experiments on silicon used an uncoated set of plates with a quantum efficiency of  $\sim 10\%$ ; for the later experiments on carbon, we instead used a pair of 2–3 times more efficient KBr coated plates. The spatial resolution of the MCP's is approximately  $100 \mu\text{m}$  and temporal resolution is achieved by gating the bias on the plates with 20 ns wide high voltage pulses (typically 1500 V magnitude to achieve the  $\sim 10^6$  gain required to see a single x-ray camshaft pulse). This gate width is sufficient to isolate a camshaft x-ray pulse from the multibunch train, allowing experiments that use the intrinsic  $\sim 70$  ps duration of the camshaft pulse for time resolution as we vary the relative delay of the femtosecond laser pump pulse.

For faster time resolution at the cost of experimental complexity and reduced

quantum efficiency, an ultrafast x-ray streak camera can resolve the temporal profile of the camshaft pulse with resolutions approaching 1 ps. Figures 2.16 and 2.17 illustrate the working principles behind this detector, originally described in ref. [23]. The dispersed spectrum of x-rays initially hits a photocathode. The composition of the photocathode is optimized for a particular spectral range; in the case of silicon, we used a photocathode composed of layers of 500 Å polyimide (on the x-ray side), then 300 Å Al, and then 500 Å CsI.<sup>1</sup> The layer of polyimide (a type of plastic) is there for mechanical support, and the Al provides a conductive layer that allows us to set the potential of the photocathode to a constant -7 kV. X-rays that penetrate these two layers enter the CsI and generate a large number of electron-hole pairs due to the small work-function and high x-ray absorption in this material. A narrow slit on a grounded metal substrate lies a few millimeters behind the photocathode, aligned so that it is parallel to the direction of x-ray spectral dispersion. The high electric field between the Al plane and the grounded slit rapidly accelerates the photoelectrons, ejecting them from the photocathode and drawing them through the slit. The temporal and spatial profiles of the x-ray pulse are thus mirrored by a high velocity electron pulse. This electron pulse propagates down the camera, passing between a pair of sweep plates. As the electron pulse moves between the plates, a quickly ramping electric field voltage copropagates with the pulse, causing electrons at different times within the pulse to be accelerated by different amounts, depending on exactly

---

<sup>1</sup>For the experiments on carbon, we replaced the plastic polyimide layer with 1000 Å Si<sub>3</sub>N<sub>4</sub> and increased the thickness of the CsI layer to 700 Å.

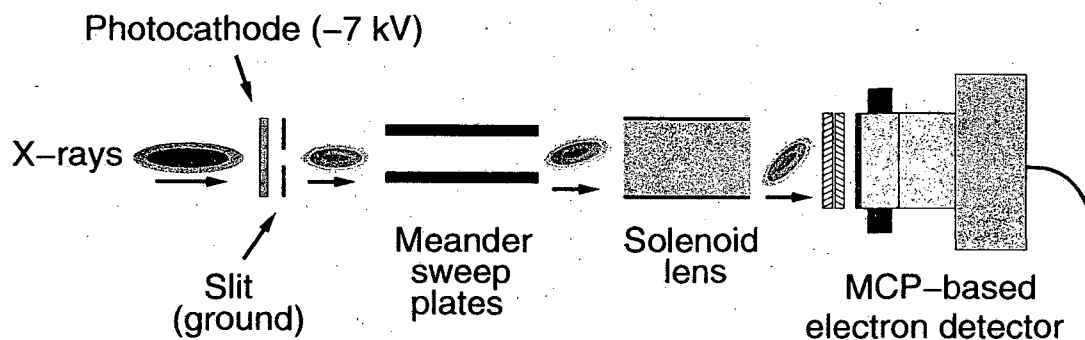


Figure 2.16: Sketch of ultrafast x-ray streak camera.

when they arrive with respect to the ramp signal. To slow down the propagation of the electronic ramp signal to the relatively slow speeds of the 7 keV electron pulse, the sweep signal is forced to adopt a windy, “meandering” conduction path along the plates (shown in figure 2.17). This meander design forces the electron beam to interact with the transverse field of the ramp signal again and again, resulting in a large distribution of transverse velocities that vary linearly over the temporal profile of the electron beam.

As the electron pulse propagates beyond the plates, these time-dependent transverse velocities cause the beam to spread out in a direction perpendicular to the slit. A solenoid magnetic lens focuses this “swept” electron beam to an image of the slit on the MCP-based detector of figure 2.15. The result is a two-dimensional image, with one axis representing time and the other x-ray wavelength.

The source of the fast-ramping electronic signal is a GaAs photoconductive switch triggered by a small portion of the femtosecond laser output. Figure 2.18 shows a

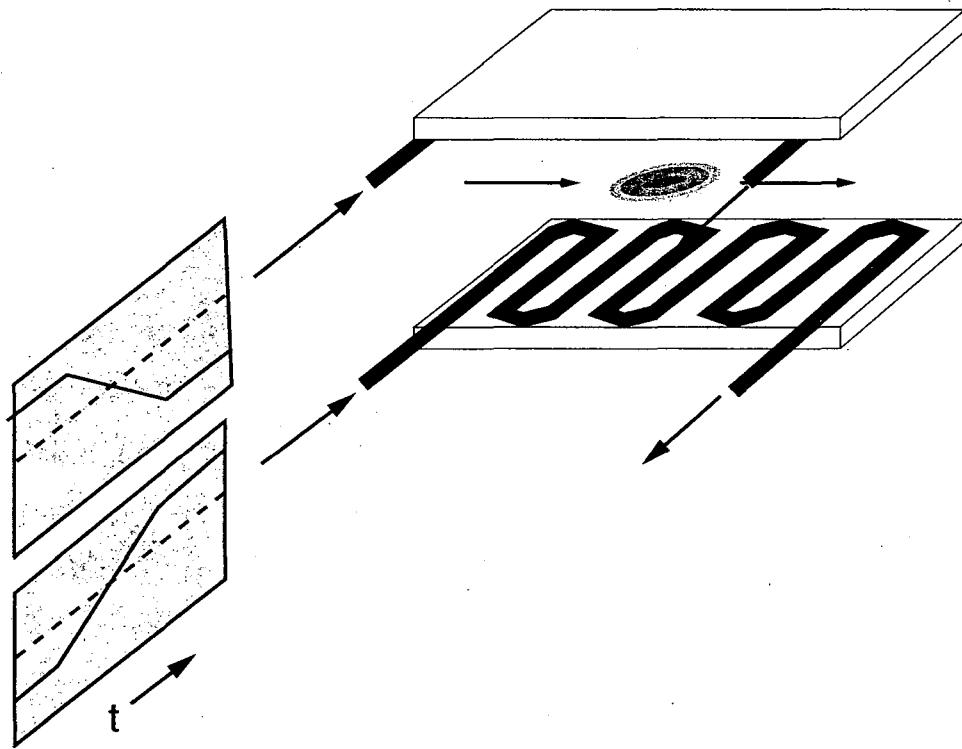


Figure 2.17: Operation of meander sweep plates in the streak camera. The fast, nearly step-like electrical signals sketched on the right propagate through the meandering tracks on the inner surfaces of the plates, providing a quickly increasing electric field that interacts with the electron pulse with each pass.

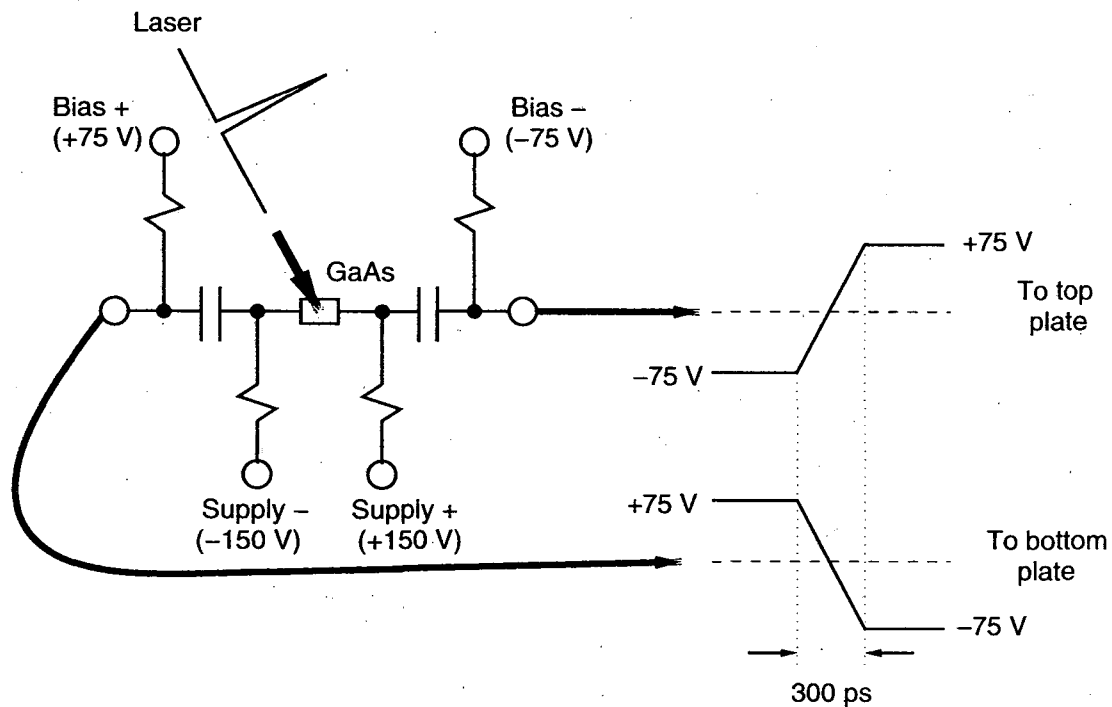


Figure 2.18: Sketch of GaAs photoconductive switch.

sketch of this switch. Initially, the output of the switch for each plate is constant, deflecting the electron beam to one side of the MCP's. The laser pulse then strikes the GaAs wafer at the center of the switch, quickly (within  $\sim 100$  fs) generating carriers and dropping the electrical resistance across the GaAs. Stored charge rushes across the wafer, causing a very fast voltage change that propagates across the capacitors (with some low-frequency cutoff) and into the sweep plates. The voltages in the figure are only nominal; in practice, we tune the sweep and bias voltages to get the desired sweep speed and beam position. Although time resolutions of less than 1 ps have been measured for this camera [23], for these experiments low quantum yield limited the useful resolution to 5 ps.

We can roughly estimate the number of detected photons per x-ray camshaft pulse from equation 2.2 and the physical parameters of the beamline and endstation outlined above. For the silicon *L*-edges at 70–280 eV, the MCP detector measures on the order of 200 photons/pulse in a 1% energy window. With the streak camera the theoretical throughput is similar, but during the experiment the quantum efficiency was roughly a factor of ten less (presumably due to loss of signal within the camera). For the carbon experiment near 300 eV, the MCP detects approximately 300 photons/pulse/1% bandwidth, and the streak camera detects about 50 photons/pulse/1% bandwidth.

## 2.4 Overall timing

Although sections 2.2.1, 2.2.2 and appendix A discuss some aspects of timing the laser pulses to the synchrotron bunches, this section provides a more complete overview of the techniques involved in coordinating the timing of the experiment as a whole. This timing is especially critical for the experiments on carbon due to possible contamination of the x-ray optics from extraneous synchrotron light, as mentioned in section 2.3.

Figures 2.19 and 2.20 show block diagram overviews of the timing for the experiment on silicon and carbon targets, respectively. The setup for silicon experiments is simpler, both because of the irrelevance of carbon contamination on optics and the fact that they were done before installation of the 10 Hz amplifier.

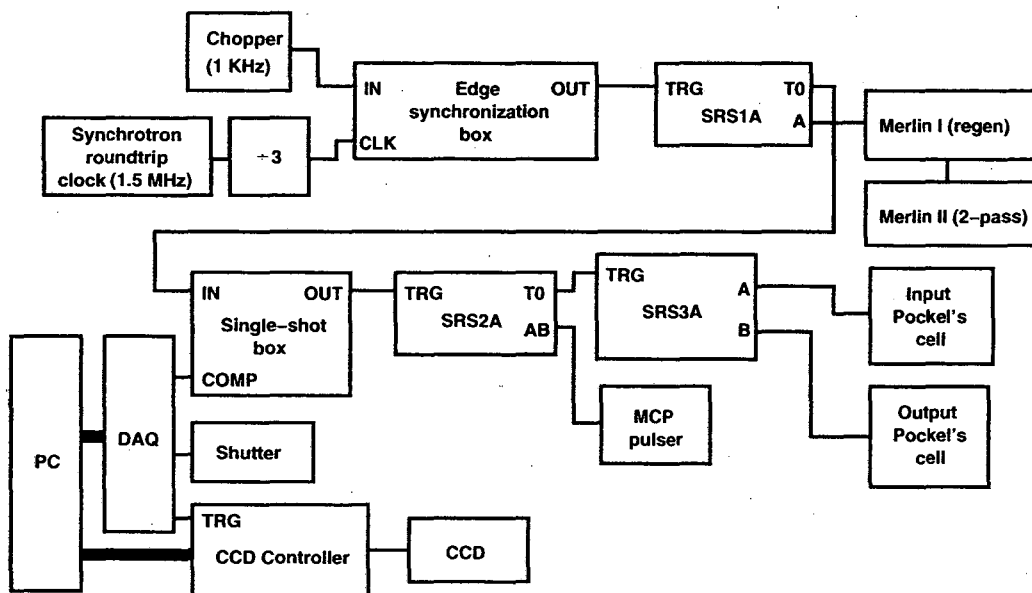


Figure 2.19: Block diagram of timing setup for silicon foil experiments.

The timing for the silicon experiments begins with the diode signal output from the x-ray chopper, set to use a 6-slot wheel pattern to pass  $40 \mu\text{s}$  time slices of the bend magnet output each millisecond. The 1 KHz output of these chopper diodes gives an indication of when x-rays pass through the slots of the chopper. This signal is then fed into the “edge synchronization” circuit sketched in figure 2.21. The purpose of this circuit is to delay the rising edge of the chopper diode signal so it occurs synchronously with the 510 KHz signal discussed in section 2.2.2. Since the period of this signal is only 1968 ns, the delayed output from the box still indicates the timing of the chopper x-ray “windows” well enough to predict when x-rays will pass through. This signal then triggers an SRS DG535 delay generator (labeled “SRS1A” in the drawing). SRS1A is configured to provide two outputs: one is sent to trigger the

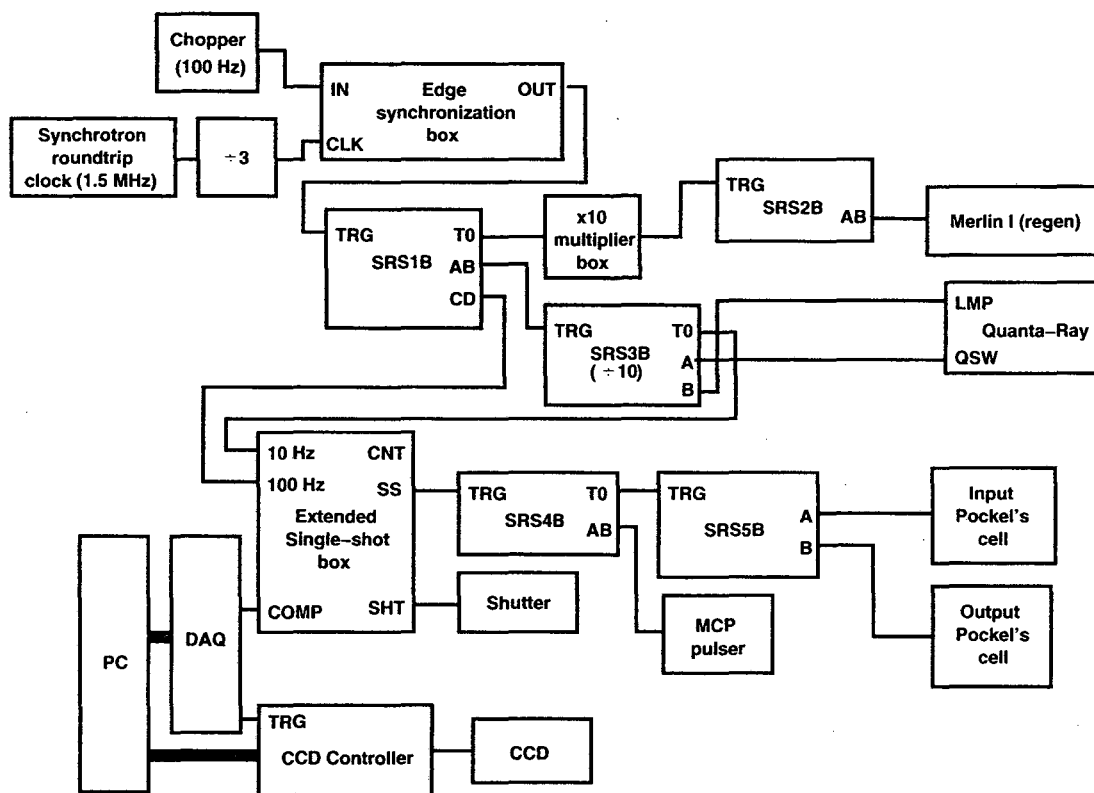


Figure 2.20: Block diagram of timing setup for carbon foil experiments.

lamps and Q-switches of the two Merlin amplifier pump lasers, and the other enters the circuit drawn in figure 2.22 (the “single-shot box”). The circuit uses this signal and a TTL trigger signal from a Windows PC DAQ board (National Instruments, model AT-MIO-10X) to output a single pulse, synchronized to the rising edge of its input from SRS1A but occurring only once after each pulse from the computer. We then feed this into another SRS DG535 (“SRS2A”) that provides triggers to the high voltage pulser for the MCP’s and yet another SRS DG535 (“SRS3A”). SRS3A creates triggers for the regenerative amplifier’s Pockel’s cells, causing the amplifier to output a single laser pulse that is at a known delay with respect to the x-ray camshaft pulse, the MCP gate timing, and the chopper slot timing. The trigger for the x-ray shutter is controlled by a TTL output from the computer DAQ board, configured to simply open and close the shutter several milliseconds before and after sending a pulse to the single-shot box.

When collecting data images from the MCP-based detector or the streak camera, we use a computer controlled CCD camera to collect the sum of several shots over different regions of the foil at once (usually spanning one “row” of the foil). Further, for each row, we actually collect three sets of images: one with the pump laser blocked (“before”), one with the laser striking the foil once for each spot (“with laser”), and once with the laser again blocked, but looking at the holes in the foil left behind (“after”). Other than the time of collection and whether the laser is physically blocked, there is no difference in the procedure for collecting these images. We then

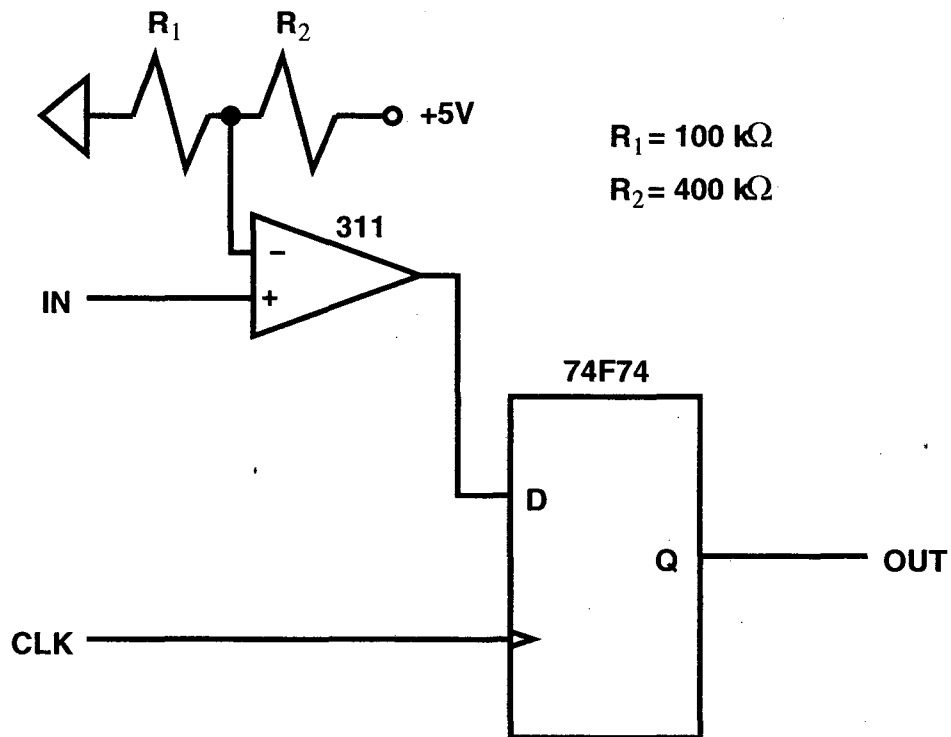


Figure 2.21: Circuit schematic for the “edge synchronization box” used to delay the edges of the chopper diode signal to that they occur synchronously with the CLK input (the synchrotron roundtrip clock divided by 3).

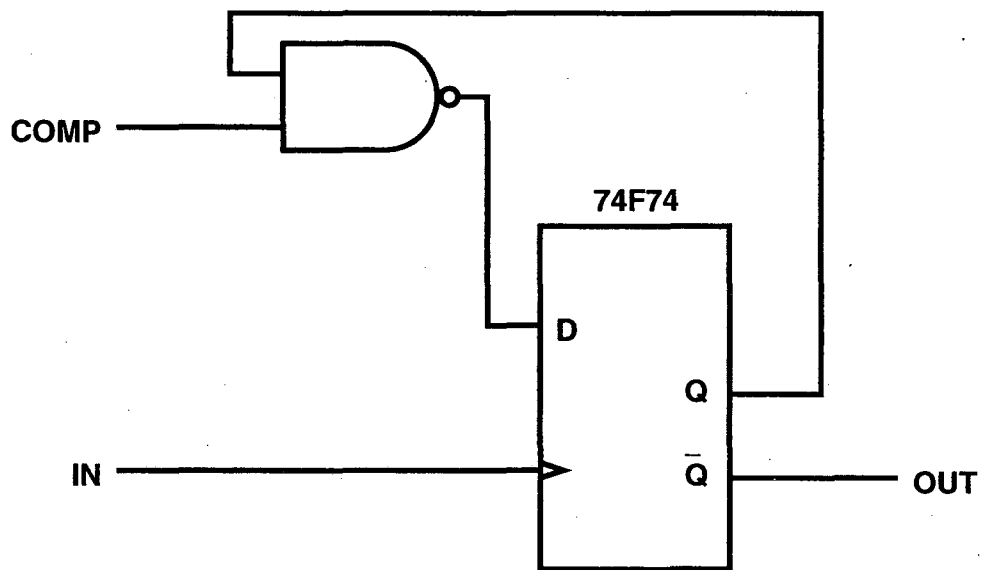


Figure 2.22: Circuit schematic for the single-shot gate switch (“single-shot box”) used in the silicon experiments.

use the “after” image to normalize the other two, extracting a transmission spectrum for both the unheated and heated foils.

The timing apparatus for the carbon experiments sketched in figure 2.20 is similar to that for the silicon experiments, with a few extra steps to minimize superfluous x-ray flux and to trigger the 10 Hz pump laser. Instead of running the chopper with a 6-slot wheel pattern to modulate the x-rays at 1 KHz, we use a single slot pattern to modulate the x-ray signal at 100 Hz. Since the shutter opening time is  $\sim 5$  ms, this gives ample time to use the shutter to prevent any chopper pulses other than the one used for the experiment to pass through to the filtering mirrors. As before, the diode signal from the chopper passes into the the edge synchronization circuit of figure 2.21 and then into an SRS DG535 box (“SRS1B”) that splits the ring-clock synchronized chopper signal into three separate timing signals. One signal branch enters the circuit of figure 2.24 (the “x10 multiplier box”) that uses the input 100 Hz signal to create a 1 KHz trigger for a DG535 (“SRS2B”) that in turn creates triggers for the Merlin pump laser. Another branch from SRS1B is sent to yet another DG535 (“SRS3B”) that divides the trigger by 10 and uses the resulting 10 Hz signal to trigger the lamps and Q-switch of the Quanta-Ray pump laser. Another 10 Hz output of SRS3B and the final 100 Hz output of SRS1B feed into the circuit drawn in figure 2.23.

The operation of this “extended single-shot box” is similar to that of the circuit of figure 2.22, except that the circuit now has more to do: it must ensure that the trigger occurs synchronously with the 10 Hz Quanta-Ray lamp trigger, and it must

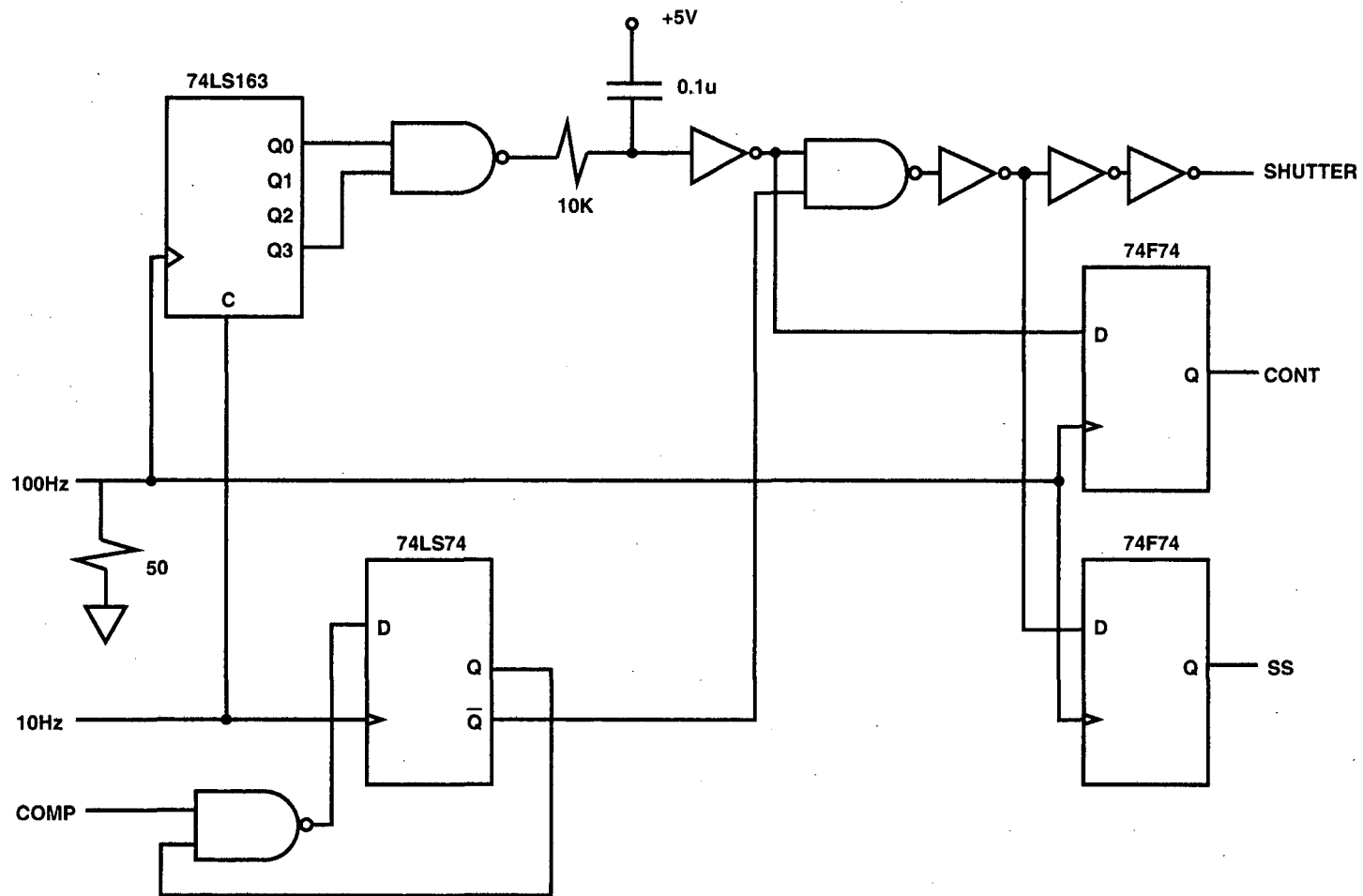


Figure 2.23: Circuit schematic for the extended single-shot gate switch (“extended single-shot box”) used in the carbon experiments.

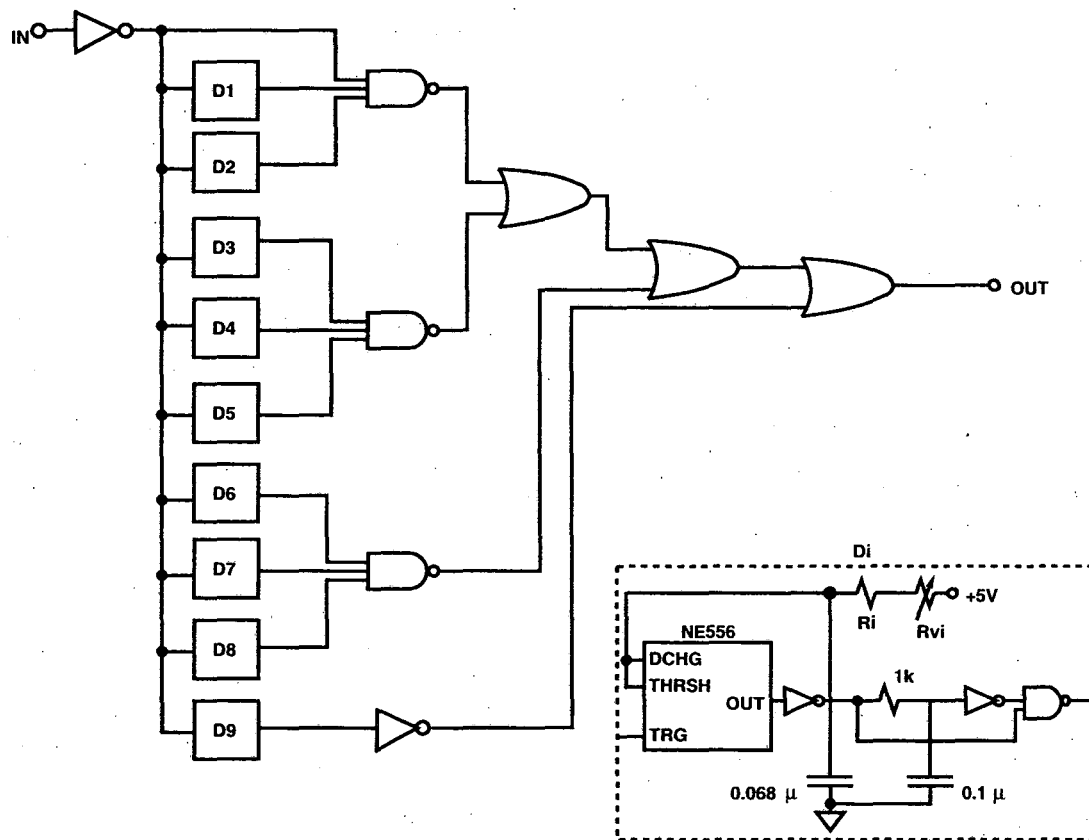


Figure 2.24: Circuit schematic for the 100 Hz to 1 kHz “x10 multiplier box”. The circuit is essentially just a set of 9 delay generators that produce short pulses at 1 ms intervals from the 100 Hz input signal. The pulses are then ORed together to produce the output. While making adjustment of the input frequency difficult, this design has the advantage of very low ( $< 5$  ns) jitter of the “first” pulse with respect to the input.

$i$	$R_i(\text{k}\Omega)$	$R_{vi}(\text{k}\Omega)$
1	11.0	2
2	23.0	5
3	35.0	5
4	47.0	5
5	65.0	5
6	74.0	10
7	82.0	10
8	92.0	20
9	105	20

Table 2.2: Resistor values of indexed stages  $D_i$  in figure 2.24. The  $R_{vi}$  values indicate the maximum value of an adjustable potentiometer that is tuned to make the separation between pulses exactly 1 ms.

also provide a trigger for the x-ray shutter that will let through only the pulse used for the experiment. The circuit works by using a counter, reset by the rising edge of the 10 Hz input and clocked by the ring-clock-synchronized 100 Hz chopper signal. When a signal from the computer enables the output of the counter, the circuit uses the counter output to create a trigger for the x-ray shutter and for the MCP pulser and the laser Pockel's cells (via "SRS4B" and "SRS5B") that are appropriately timed with respect to the firing of the Quanta-Ray pump laser.

Figure 2.25 shows a timing diagram of several of the signals described above. With these modifications to the timing, the procedure for data collection with the carbon experiment is identical to that for the silicon. Because some carbon contamination of the x-ray optics is unavoidable, the use of "after" images of the holes left behind

by the laser to normalize the spectra is essential to identify spectral features of the sample foil.

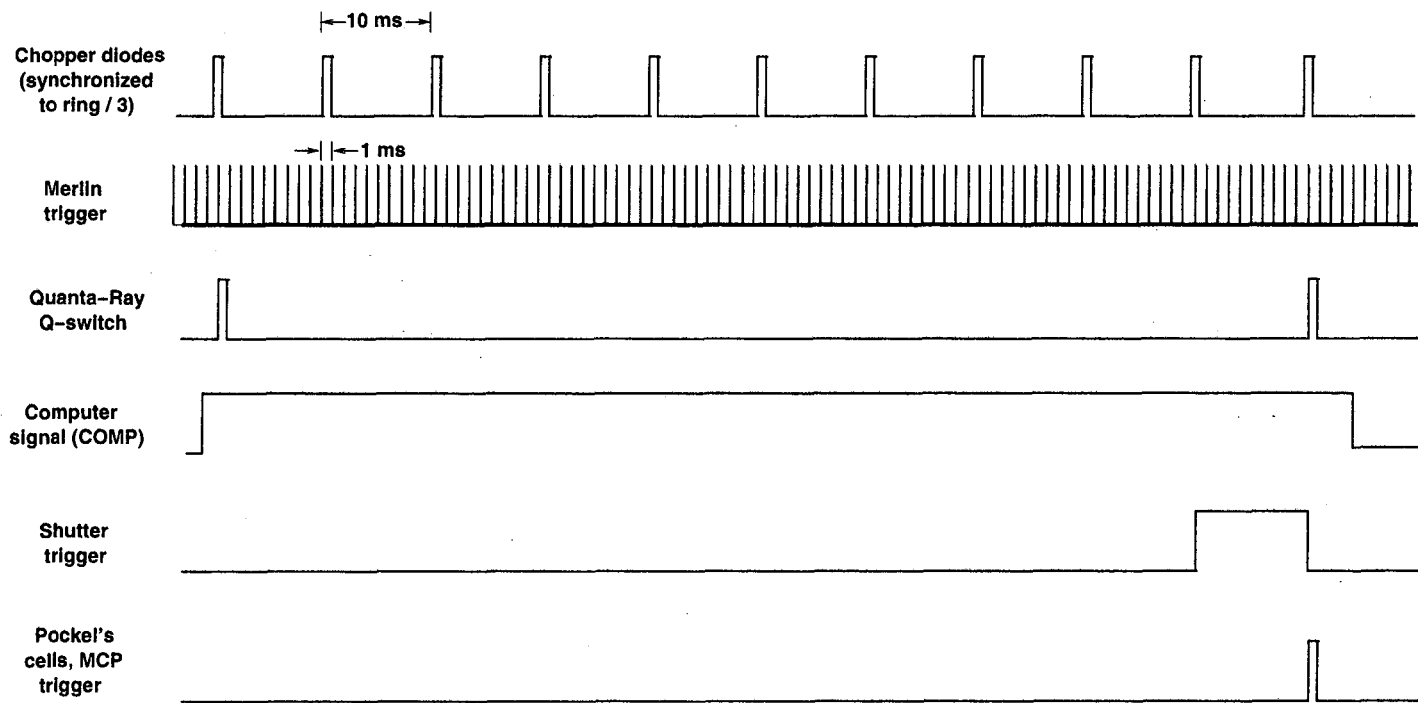


Figure 2.25: Timing diagram of signals in the carbon experiment.

## Chapter 3

# Time-resolved XAS of liquid silicon

### 3.1 Background and previous work

The melting of solid, covalently bonded semiconductors such as silicon into metallic liquids has attracted considerable attention in recent years. This is due to both the technological importance of semiconductor processing and the peculiar structure of the melt: typically, these liquids have coordination numbers of 6–7, values significantly lower than in most liquid metals where the number of nearest-neighbors is in the range of 10–12 [79, 71, 50]. This lower coordination number is presumably due to a persistence of covalent bonding. Molecular dynamics simulations of molten silicon have suggested that approximately 30% of the bonding in liquid silicon is covalent and that the bonding in the melt is a highly dynamic phenomenon, with bonds rapidly forming and breaking on a time scale of 20 fs [97]. Although x-ray and neutron

diffraction experiments have accurately characterized the atomic structure of liquid silicon [98, 32], experimental investigation of the electronic structure is incomplete.

As early as 1986, Murakami and co-workers used nanosecond pulses of continuum x-rays from a laser-produced plasma to study the time-resolved  $L$ -edge spectrum of laser-heated silicon foils [60, 96, 34]. Figure 3.1 shows the temporal evolution of the  $L$ -edge spectrum they observed. Although they were able to interpret their data qualitatively in terms of a combination of melting and break-up of the sample into droplets, a quantitative interpretation requires higher time resolution, sufficient to distinguish between these very different effects. The picosecond resolution offered by our apparatus directly addresses this problem, and in addition it offers a factor of 4 improvement in the spectral resolution of the Murakami data.

Besides the present work, Nakano and co-workers have also recently extended silicon  $L$ -edge spectroscopy into the picosecond domain, but at laser fluences much too low for melting [61]. They observe a small transient change in the structure near the  $L_{II,III}$  edge which lasts for a shorter time than their roughly 40 ps time resolution. They attribute this change to excitation of electron-hole pairs by the pump pulse.

## 3.2 Pump-probe data

Representative data using the pump-probe technique with the MCP detector are shown in figure 3.2 for a 500 Å silicon foil with an incident laser fluence of 0.7 J/cm<sup>2</sup> at a wavelength of 800 nm. The dashed curve shows the absorption spectrum before

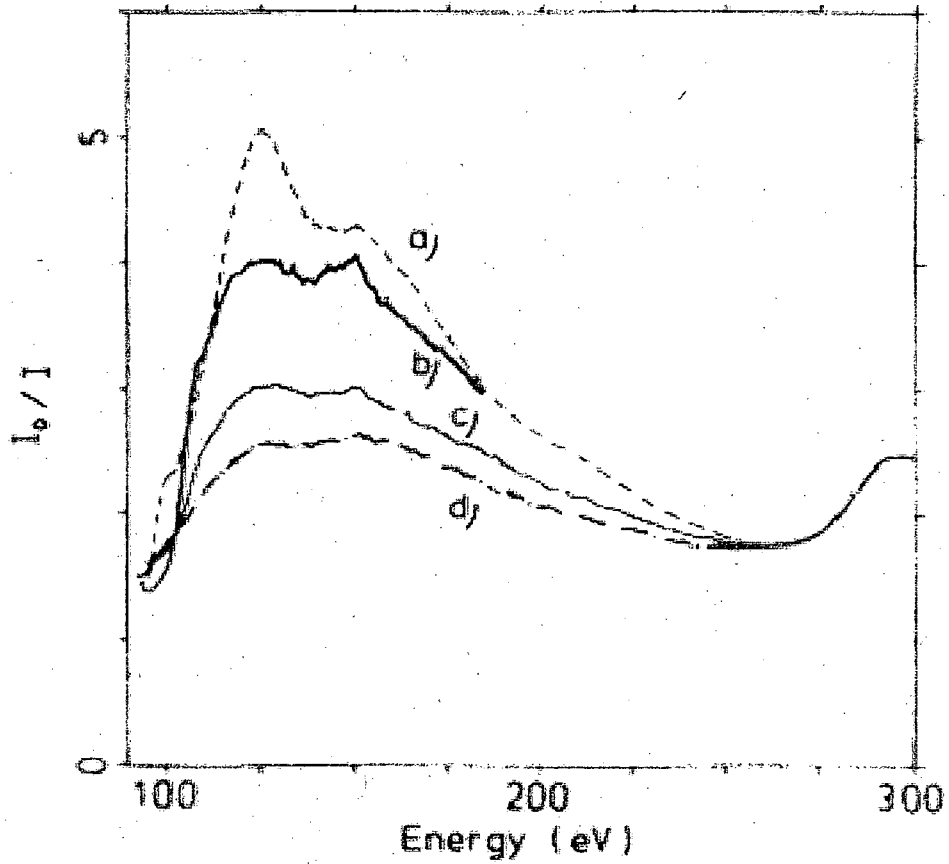


Figure 3.1: Inverse x-ray transmission data from Murakami, *et al.* showing the nanosecond temporal evolution of the soft x-ray spectrum of a laser-heated silicon foil. Plot (a) shows the unheated spectrum, and the others are at various times after heating: (b) 12 ns, (c) 30 ns, and (d) 60 ns. Taken from figure 4 of ref. [60].

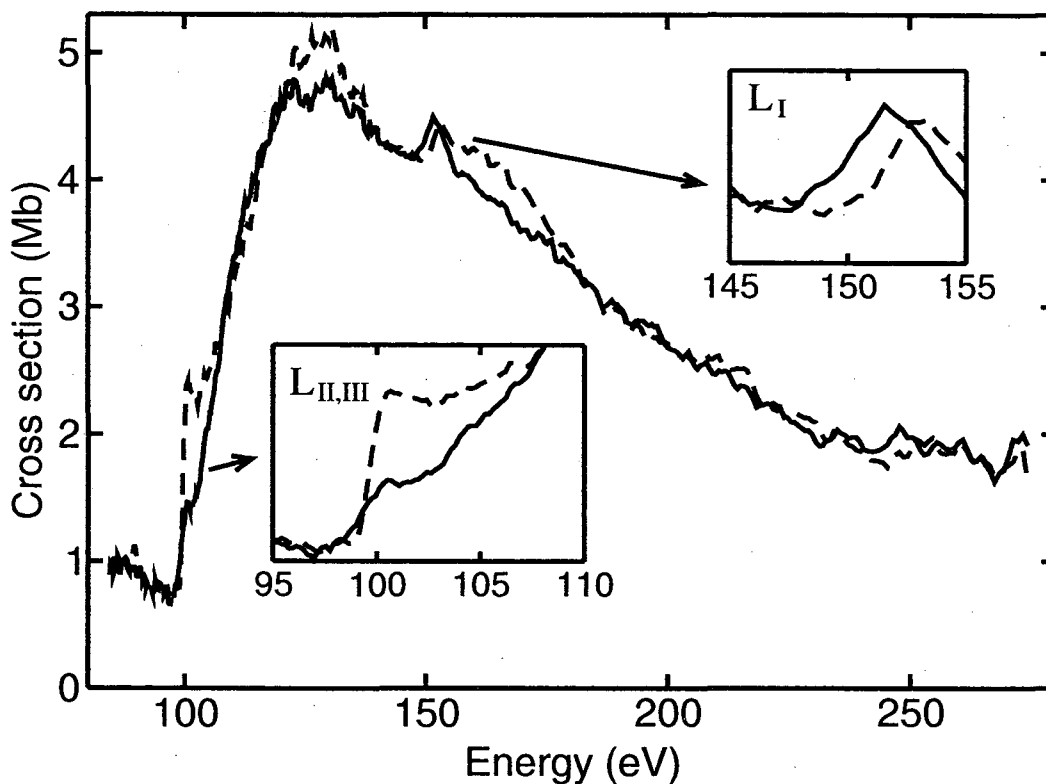


Figure 3.2: Absorption spectra of the 500 Å foils before (dashed curve) and 100 ps after (solid curve) laser excitation. The  $L_{II,III}$  edge at 100 eV and the  $L_I$  edge at 150 eV are shown with expanded scales as insets. The plots show the average of about 100 laser/x-ray shots.

excitation. This spectrum of the unheated foil agrees with previous measurements on solid amorphous Si, allowing for a 30% uncertainty in the assumed areal density of the foils [14, 13]. The large edge at 100 eV is a superposition of the  $L_{II}$  and  $L_{III}$  spin-orbit split edges, which are not separately distinguishable due to the resolution of the spectrometer. At 150 eV the smaller  $L_I$  edge appears. Energies beyond approximately 280 eV were inaccessible due to absorption above the  $K$ -edge of carbon in the optical path.

The solid line in figure 3.2 shows the absorption spectrum 100 ps after laser

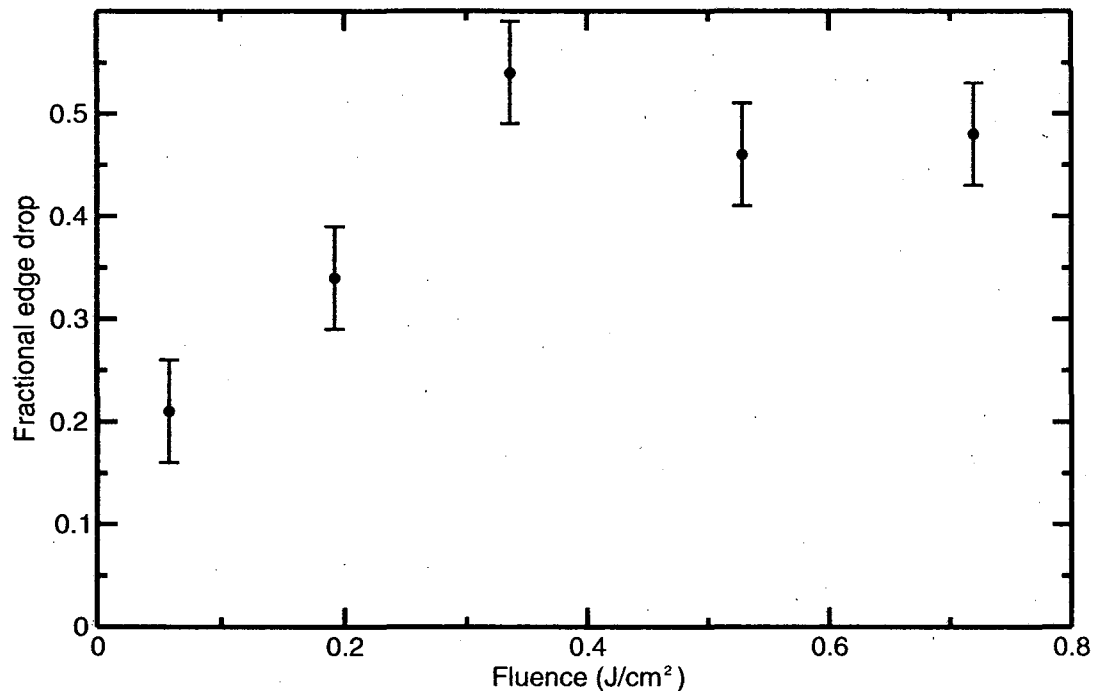


Figure 3.3: Fluence dependence of  $L_{II,III}$  post-edge drop in absorption, integrated from 100–105 eV and normalized to the  $L_{II,III}$  absorption step of the unheated foil.

excitation. The melting induced by the laser causes a dramatic effect at the  $L_{II,III}$  edge: the magnitude of the edge drops by approximately 50%, and the width broadens to 2 eV. In addition the near-edge features of the  $L_{II,III}$  edge are modified, the  $L_I$  edge is shifted to lower energies by  $1.6 \pm 0.2$  eV, and the small  $L_{II,III}$  EXAFS oscillations beyond the  $L_I$  edge disappear (an observation discussed in greater detail below).

Figure 3.3 shows the dependence of near-threshold absorption of the  $L_{II,III}$  edge on incident laser fluence. The observed absorption change takes effect at approximately  $0.1 \text{ J/cm}^2$ , and it reaches a fluence-independent saturation level above  $0.3 \text{ J/cm}^2$ . The onset fluence is roughly consistent with previous measurements of the threshold fluence for femtosecond melting in bulk silicon [28], and the observed saturation at higher

fluence suggests that under these conditions the probed region of the foil is completely melted. At the fluence of  $0.7 \text{ J/cm}^2$  where all other reported measurements have been performed, transreflectance measurements using an integrating sphere show that 40% of the laser pulse energy is absorbed in the foil (see appendix B). Estimates of the temperature are difficult, since the resulting  $600 \text{ kJ/mol}$  energy density in the foil is comparable to the  $450 \text{ kJ/mol}$  cohesive energy of the solid [106]. At these energies the heat capacity increases rapidly as much of the energy is used to break strong interatomic bonds as the liquid approaches its critical temperature at  $\sim 5000 \text{ K}$  [57].

The observed spectral features do not change significantly for longer pump-probe delays until about 10 ns after excitation. At this time, the overall transmission of the foil begins to increase, suggesting that material is starting to leave the probed region. This observation is consistent with experimental and theoretical work on femtosecond laser ablation which suggest that, after  $\sim 100 \text{ ps}$  of initial expansion, the hydrodynamic evolution of the laser-melted foil results in an expanding 1-D liquid bubble with approximately constant temperature and density, persisting for several nanoseconds [83, 3].

### 3.3 Streak camera data

To achieve higher time resolution of the changes in the  $L_{\text{II,III}}$  edge, we employed the streak camera detector to measure the transmission spectrum of a  $1000 \text{ \AA}$  foil with 5 ps resolution. To obtain better statistics for the dynamics of the edge drop, we integrated

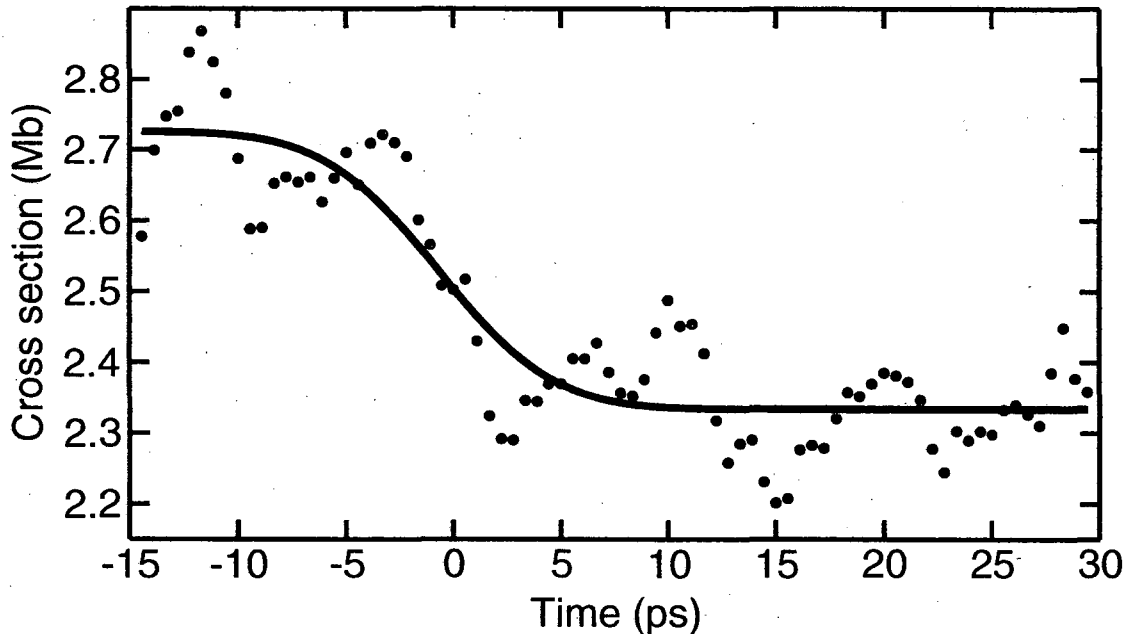


Figure 3.4: Absorption of a 1000 Å silicon foil immediately above the  $L_{II,III}$  edge as a function of time after laser excitation. The data points show the average of 140 shots. The curve shows a fit of the data to a step function convolved with a 5 ps FWHM Gaussian.

the signal over a 5 eV energy range above the edge. Figure 3.4 shows this integrated post-edge absorption as a function of time after laser excitation. The absorption drop is instantaneous within the camera resolution. Further, the magnitude of the drop agrees with that observed in pump-probe measurements on 1000 Å foils—a smaller effect than that observed in 500 Å foils, suggesting that the thicker foils are only partly melted even at  $0.7 \text{ J/cm}^2$ . These observations are consistent with ultrafast optical measurements, where a transition from the solid to a high reflectivity, electronically disordered phase occurs on a time scale of 300 fs [28, 94].

### 3.4 Modeling

To obtain models for comparison with the x-ray absorption data, we employed molecular dynamics (MD) simulations to calculate atomic structure and then used the *ab initio* x-ray absorption code FEFF 8.1 [4] to calculate the photoabsorption spectra from this structure. We performed the MD simulations on a block of 216 atoms initially in a crystalline configuration, with periodic boundary conditions in a fixed volume supercell. The system (atoms + electrons) was heated by a laser pulse, as described in ref. [43, 45], and then permitted to equilibrate for several picoseconds to 3100 K, near the vaporization temperature of liquid silicon. The pair correlation function of the final state agrees well with the results of x-ray diffraction measurements on liquid silicon near the melting temperature for pair distances  $R < 3 \text{ \AA}$  (see figure 3.5) [98, 32].

The FEFF calculations of the x-ray absorption spectra used an initial-state approximation, since the inclusion of final state (core hole) effects as implemented in the code yielded a poorer match to experiment for the near-edge structure of the solid silicon  $L_{II,III}$  edge in the range of 10–50 eV past the edge threshold, and it had little qualitative impact on the spectral shape closer to the edge thresholds. Use of an initial-state model in preference to a fully relaxed final-state approximation has precedent in studies of the  $L$ -edges of 3d transition metals, where omission of core-hole effects often results in better agreement with experiment [62].

To extract absorption spectra from the simulated liquid structure, we ran FEFF

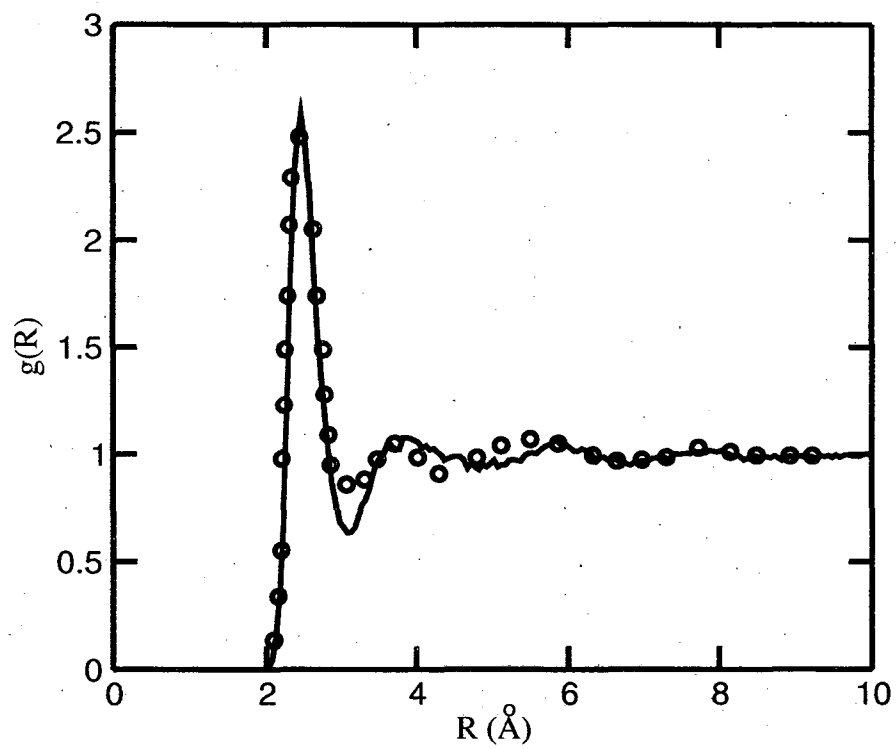


Figure 3.5: Comparison of the liquid silicon pair correlation function from the MD simulations (solid line) with measured values from ref. [98] (circles).

on each of approximately 50 randomly selected atoms as x-ray absorbers. The code calculated the spectrum of each absorber using a cluster of radius 6.1 Å encompassing about 30 atoms. We then averaged together the individual spectra to compare with experiment. We performed similar calculations on the spectrum of the initial solid using a published model structure of amorphous solid silicon [7].

Figure 3.6 shows a comparison of the model results for the near-edge structure of the  $L_{II,III}$  edge for both the initial solid and the liquid. For energies above 110 eV, the model calculations are close to experiment. The prominent feature in this energy range is a broad absorption maximum near 125 eV. The model shows a  $-4$  eV shift in this feature on melting that is consistent with the experiment.<sup>1</sup> This energy shift and the associated reduction of the peak on melting are consequences of the structural changes reflected by the pair correlation function, namely an increase in disorder and an expansion of the average nearest-neighbor distance by  $0.15 \pm 0.07$  Å (compared against the 2.35 Å nearest neighbor spacing in solid silicon). The onset of short-range disorder upon melting also suppresses the EXAFS structure at higher energies via a reduction in the Debye-Waller factor  $e^{-2\sigma^2 k^2}$ , where  $\sigma$  is the variance of the bond length distribution and  $k$  is the photoelectron wavenumber, larger than  $4 \text{ \AA}^{-1}$  for photon energies above 160 eV. Melting causes a large increase in  $\sigma$  from 0.065 Å at room temperature [48] to roughly 0.25 Å, pushing down the EXAFS oscillation

---

<sup>1</sup>An experimental shift of  $4 \pm 2$  eV was estimated by using the model curves as a guide to the shape of the absorption, performing small contractions and dilations of the underlying structure as a fitting parameter. This procedure is also how we estimate the error in the change of the nearest-neighbor distance.

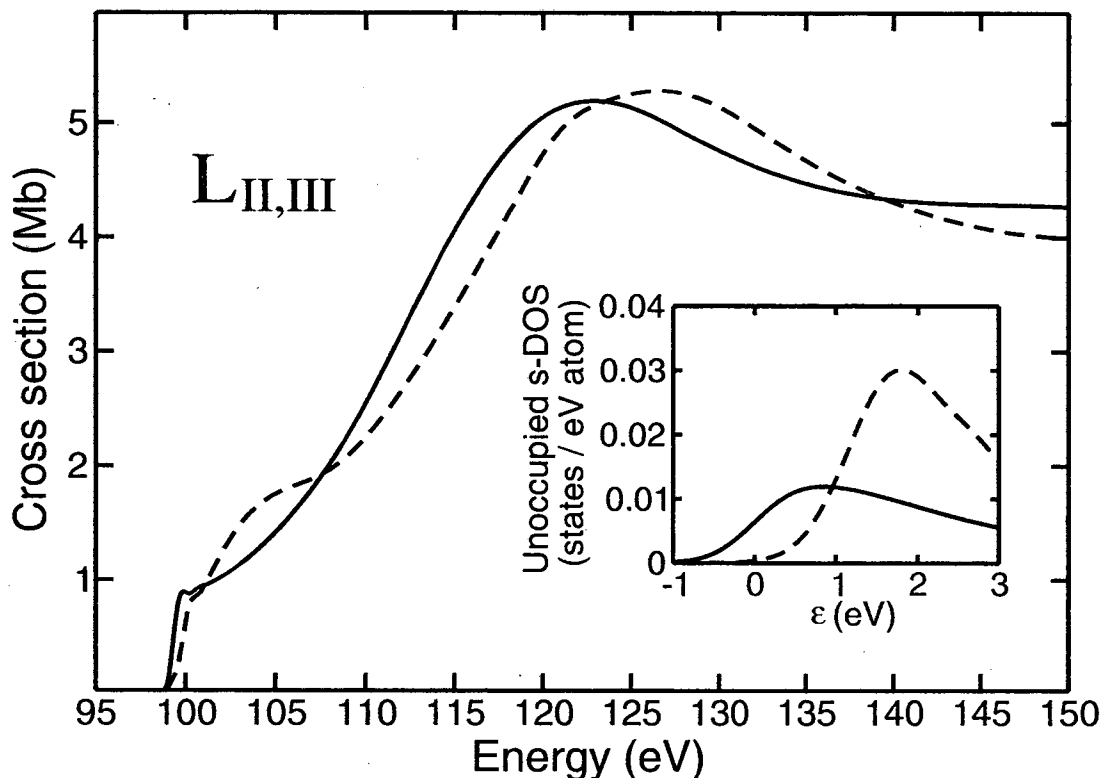


Figure 3.6: Comparison of FEFF calculations for liquid Si (solid curve) and the initial unheated silicon (dashed curve) near the  $L_{II,III}$  edge. The inset shows the unoccupied 3s-projected density of states as calculated by the MD simulations, convolved with a 1 eV FWHM Gaussian to approximate experimental resolution at the edge. The zero of the electron energy  $\epsilon$  is set equal to the calculated Fermi level for the liquid.

amplitude to well below the noise level (see figure 3.7). The observed and calculated shape of the spectrum at these energies are thus consistent with previously measured structural properties of liquid Si.

Closer to the edge threshold, the agreement is mostly qualitative, possibly due to the neglect of non-spherical components of the electron potential in FEFF [73]. The MD calculations show that the melting of silicon causes a “flattening” of the density of states (DOS) near the Fermi level and a collapse of the semiconductor band gap. This

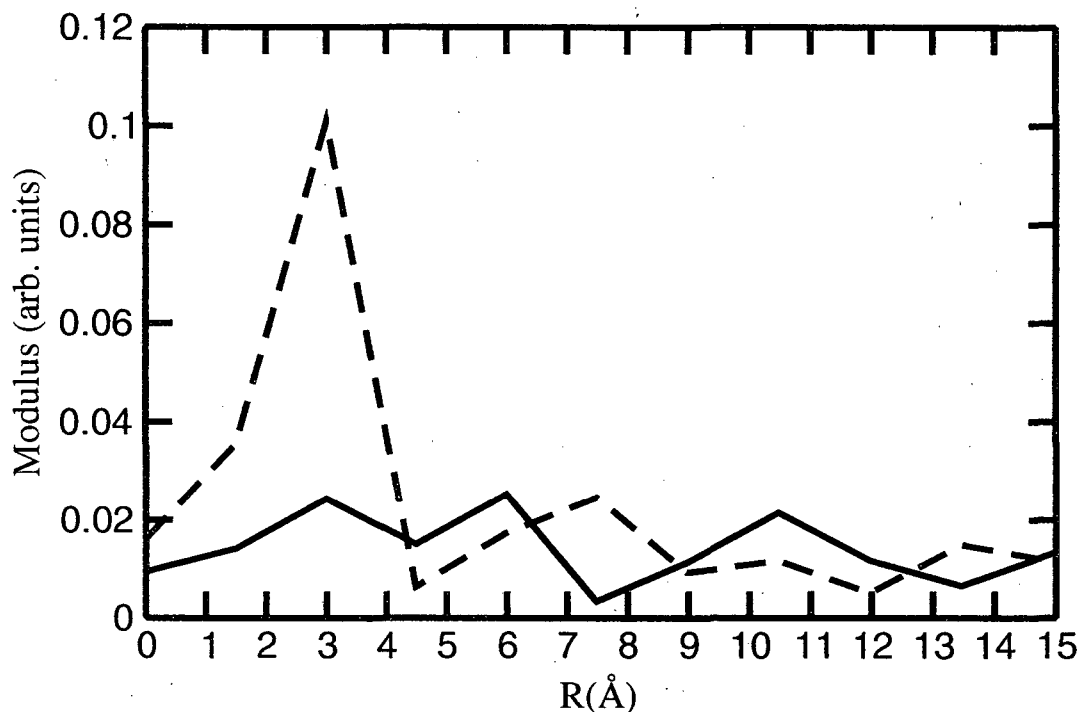


Figure 3.7: Phase-corrected fast-Fourier transform (FFT) of the data plotted in figure 3.2 for photon energies above 160 eV. Here, “phase correction” means simply that the x-ray absorption code FEFF was used to estimate values for the phase shifts  $\delta_c$  and  $\Phi$  that appear in the EXAFS equation 1.4. These scattering phase shifts were then used to correct the phase of the EXAFS oscillations before applying the FFT. The dashed line indicates the unheated EXAFS, and the solid line represents the heated silicon. The clearly visible peak near 2.35 Å in the solid is suppressed below the noise level on heating.

change in the DOS manifests itself in the spectra as a reduction in the near-threshold absorption, evident in both the model spectra and the experimental data. The inset of figure 3.6 shows a plot of the 3s-projected unoccupied DOS from the MD calculations. A comparison of these curves to the observed near-threshold absorption is favorable to within a few eV of the edge, reflecting the large drop in absorption immediately above the edge. This agreement persists even though such a comparison ignores both contributions to the edge structure from other unoccupied states permitted by selection rules and the potentially important core hole effects that have been shown in crystalline silicon to shift the  $L_{II,III}$  edge by  $-1$  eV [15]. The 2 eV edge broadening observed for the liquid  $L_{II,III}$  edge but not reproduced by the modeling may be the result of simultaneously probing a wide range of liquid densities in the experiment. By running FEFF on uniform dilations and contractions of the liquid model structure, we estimated that a 30% distribution of densities around the density of the liquid model is sufficient to cause a 2 eV edge broadening due to shifts of the Fermi level with respect to the 2p core levels (see figure 3.8). This wide density distribution also broadens and reduces by 5% the absorption maximum near 125 eV, bringing it closer to the experimental observations. Such a large variation in density might be explained by non-uniformities of energy deposition along the 300  $\mu\text{m}$  x-ray spot size, or perhaps by the large local density fluctuations expected in liquids when pushed to temperatures near the critical point [57, 56]. Extending the MD simulations to higher temperatures could provide further insight into this issue.

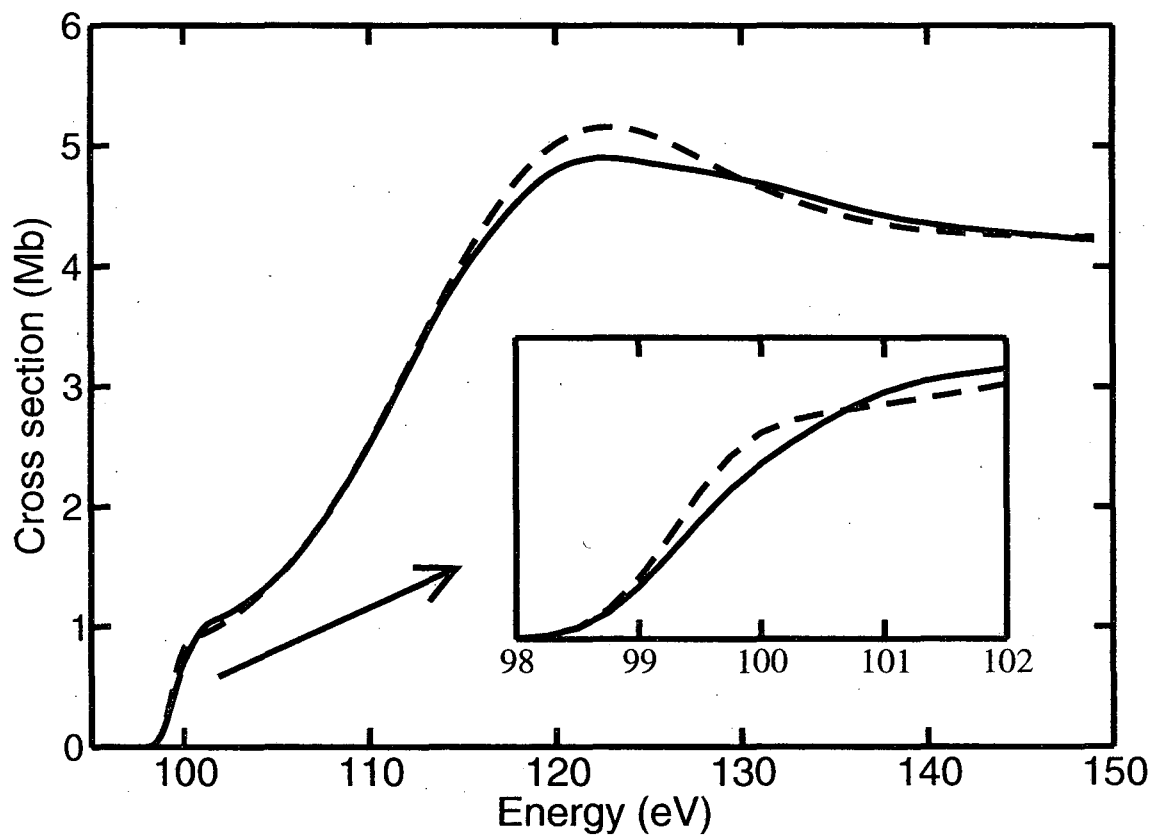


Figure 3.8: The solid line shows the approximate effects of imposing a  $\pm 15\%$  range of densities on the liquid model structure. We constructed the curve by taking a representative structure from the MD simulation output and running FEFF on a range of uniform contractions and dilations of the atomic coordinates. We then averaged the FEFF output spectra to create the plotted curve. For comparison, the liquid model spectrum from figure 3.6 is also plotted as a dashed line. Both curves have been convolved with a 1 eV FWHM Gaussian to simulate experimental resolution near the edge. The density variation causes a broadening of the spectral features that improve agreement with the experiment.

Calculations on the  $L_I$  edge are shown in figure 3.9. Although the models for both the solid and liquid forms of silicon show edge thresholds that differ from experimental values by about 5 eV, the model spectra do show an edge shift of approximately  $-1.2$  eV from the solid to the liquid due to band gap collapse, close to the observed  $-1.6 \pm 0.2$  eV shift. The unoccupied 3p-DOS plotted in the inset of figure 3.9 shows a similar shift of  $-1.1$  eV. Like the changes in the near-edge structure of the  $L_{II,III}$  edge, the  $L_I$  edge shift appears to be at least partly due to collapse of the semiconductor band gap on melting. Note that, compared to the  $L_{II,III}$  edge, the  $L_I$  edge is less sensitive to broadening effects caused by density variations because of its already large lifetime and instrumental broadening.

### 3.5 Summary and future work

By comparing the entirety of the model calculations with the data, we conclude that the high-temperature liquid silicon produced by the laser is a structurally disordered metal with an average nearest neighbor distance in agreement with that previously measured for liquid silicon near the melting temperature. Although agreement between experiment and the model is already quite good, further improvement might result from a better treatment of final-state effects and by extending the MD simulations to even higher temperatures to explore the effects of near-critical local density fluctuations. Experimentally, improvements in per-pulse x-ray flux by moving the experiment to a wiggler beamline along with improvements to the streak camera

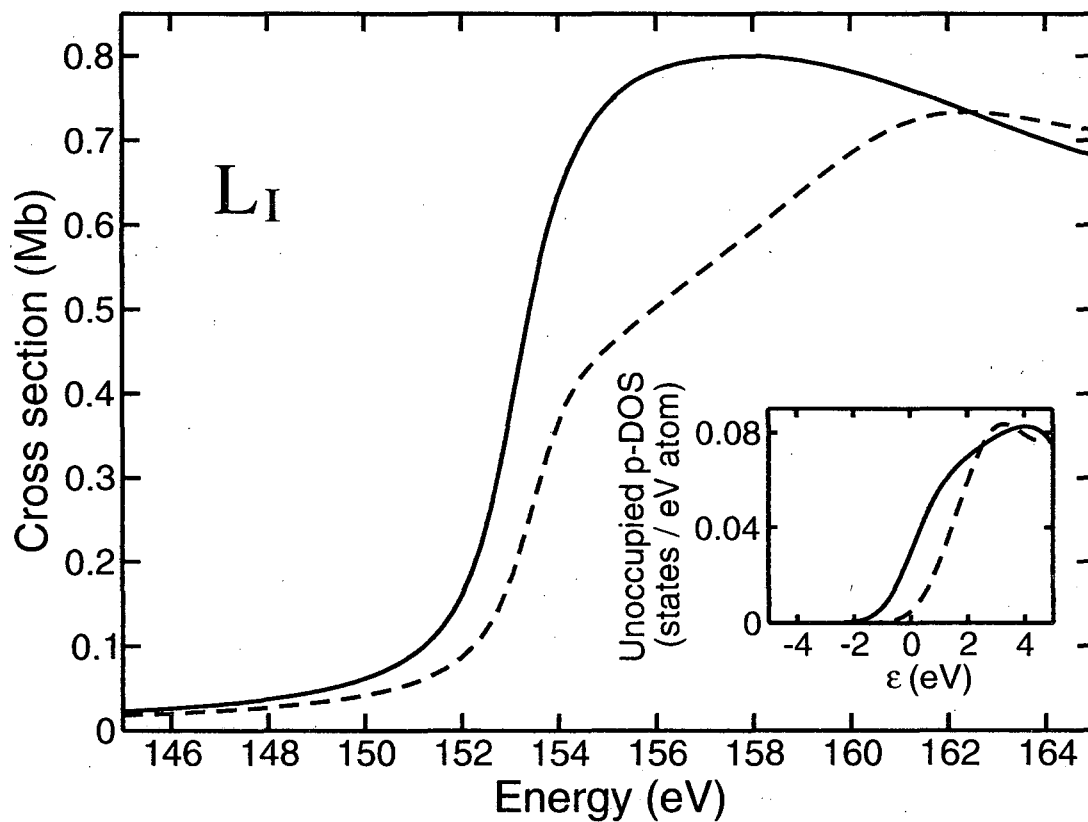


Figure 3.9: Comparison of FEFF calculations for liquid Si (solid curve) and the initial unheated silicon (dashed curve) near the  $L_I$  edge. The inset shows the unoccupied 3p-projected density of states from the MD simulations, convolved with a 2 eV FWHM Gaussian.

could push the time resolution to  $\sim 200$  fs, sufficient to resolve the electronic structure changes during the melting transition itself.

## Chapter 4

# Bonding in liquid carbon

Elemental carbon is an intriguing material, with many different known solid forms that are effectively stable at conditions of room temperature and pressure. Recent interest in nanostructured materials and advances in the fabrication of novel forms of elemental carbon such as fullerenes and nanotubes have made carbon into a technologically important material. Carbon is also a prevalent material in the universe, forming a key component of stars and of giant planets in our solar system.

Although considerable attention has focused on solid forms of carbon, the properties of liquid carbon are only vaguely understood. Liquid carbon may exist as a thermodynamically stable phase near the cores of Uranus and Neptune, and it has been hypothesized that it contributes to the measured magnetic moment of these planets [77]. Much of the difficulty for experimental studies of liquid carbon is related to the high temperatures (above 5000 K) and pressures (above 20 MPa) required

for thermodynamic stability of the liquid. These conditions are difficult to maintain in long-term equilibrium under laboratory conditions. Consequently, most of what we know about the liquid is limited to simulations and to experiments that study liquid carbon as a transient phase in response to a sudden heating of the solid. The first such experimental studies traced the T-P trajectory of the graphite-liquid melting curve by heating the graphite via flash electrical resistive heating under conditions of high pressure [16, 30, 93]. All these works show similar qualitative features of the melting line: as the pressure increases from the graphite-liquid-vapor triple point to the diamond-graphite-liquid triple point (both at similar temperatures), the melting line reaches a temperature maximum at 5-6 GPa. The magnitude of this maximum varies wildly among the experiments, but the most recent of these that uses the most sophisticated equipment measures it as 200 K above the temperature of the graphite-liquid-vapor triple point. Figure 4.1 is a phase diagram of carbon showing this feature of the melting line.

Other properties of the liquid that have been measured include the heat of fusion and the electrical conductivity (both DC and optical). The measurements of the heat of fusion all produce values near 100 kJ/mol, with the most likely value 115 kJ/mol according to [17]. Measurements of the liquid conductivity produce much more varied results, tending to be contradictory. Experiments using electrical flash heating to melt graphite samples confined in a chamber by solid refractory walls [16, 93] all observe conductivities marginally higher than that of graphite. Other experiments that melt

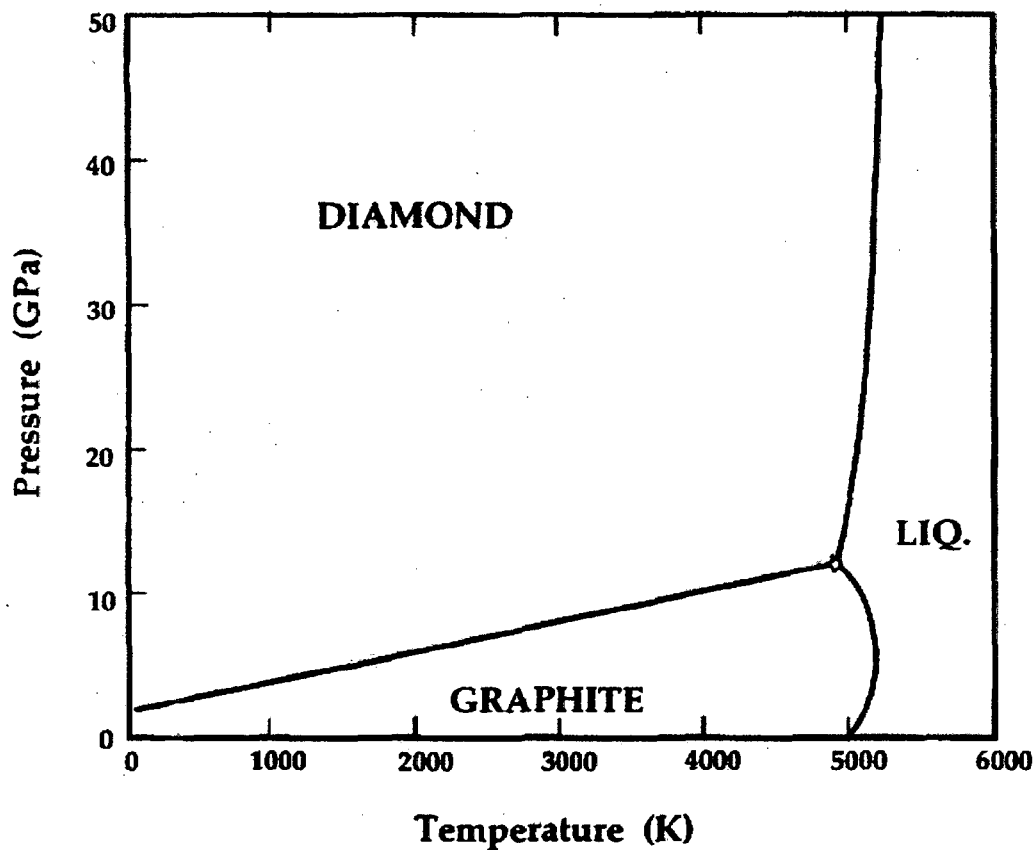


Figure 4.1: Phase diagram of carbon from figure 1 of ref. [17] showing the approximate shape of the graphite-liquid melting line. The liquid-vapor line is at pressures too low to appear on the scaling of this diagram.

graphite samples under high pressures of an inert gas result in widely varying values for the conductivity, ranging from nearly zero [55, 46] to roughly a factor of ten higher than the conductivity of the initial graphite solid [38]. Femtosecond optical pump-probe measurements by Reitze *et al.* [75] imply values of the conductivity of inertially confined molten graphite more in line with the constant-volume pressure cell data (i.e. similar to that of graphite). Similar pump-probe measurements on lower density fullerite solids estimate a conductivity about 3 times lower [21]. These different conductivity results suggest that the electronic properties are a strong function of the density and/or pressure of the liquid, but so far no experiment has been able to explore this issue explicitly.

In place of experiments, the work of Wu *et al.* [105] (which supersedes the earlier work of ref. [35]) uses first-principles MD simulations as a way to explore the properties of the liquid as function of temperature and density. The calculations show that the local bonding structure of the liquid varies continuously as the pressure increases from the liquid-vapor equilibrium line, with primarily 2-fold coordination at low pressures and densities. The liquid passes through a region of 3-fold average coordination at intermediate densities, and at 3.02 g/cc the simulations show that 4-fold coordination in the melt becomes significant as the average coordination number reaches 3.4. These results are largely consistent with the computationally simpler tight-binding simulations at 7000 K summarized in figure 4.2 [58]. This strong dependence of the local structure on density is an intriguing result that encourages experimental

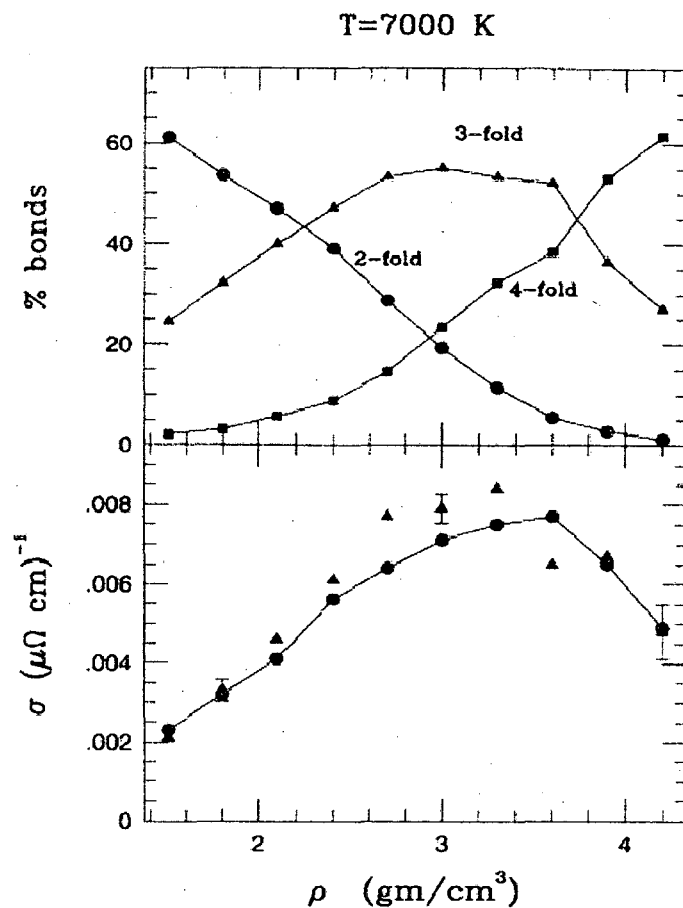


Figure 4.2: The top graph shows the percentages of 2-fold, 3-fold and 4-fold coordinated atoms as a function of density from tight-binding simulations of 7000 K liquid carbon. The bottom plot shows the calculated conductivity. This image is taken from figure 2 of ref. [58].

investigation.

## 4.1 Pump-probe results: low density liquid

To investigate the bonding properties of liquid carbon, we conducted pump-probe measurements on the carbon *K*-edge for laser-heated 500 Å thick foils of “soft” amor-

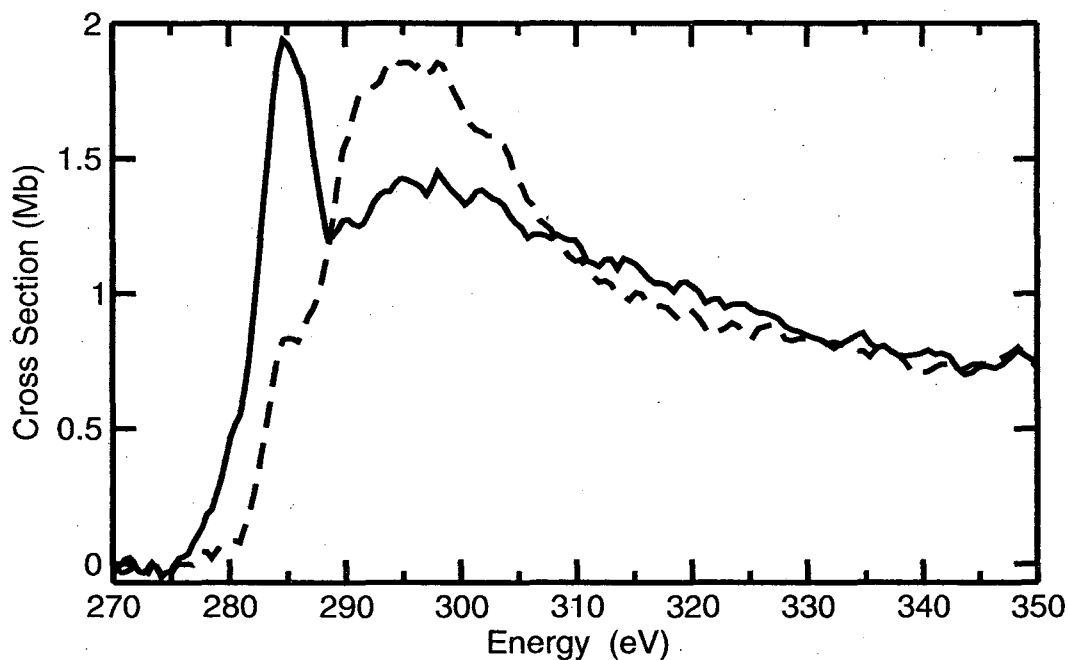


Figure 4.3: Comparison of the spectrum of the initial solid amorphous carbon foil (dashed line) with the spectrum 100 ps after laser excitation (solid line). The data shown is the average of 30 shots, with an incident laser fluence of  $2.4 \text{ J/cm}^2$ .

phous carbon (soft a-C) with a density of  $2.2 \text{ g/cc}$ . Figure 4.3 shows a comparison between the initial spectrum of the solid and the spectrum of the heated sample 100 ps after excitation at an incident laser fluence of  $2.4 \text{ J/cm}^2$ . As with silicon, the laser induces several large changes to the spectrum in the vicinity of the edge. The narrow pre-edge feature near 285 eV increases significantly on melting, and the broader post-edge absorption feature near 297 eV decreases and changes shape, developing a large tail at high energies. At later times the spectrum did not change until approximately 100 ns after excitation, when the overall absorption decreases in a manner similar to that observed in the silicon experiments.

Figure 4.4 shows a plot of the fractional change in the absorption near 285 eV as

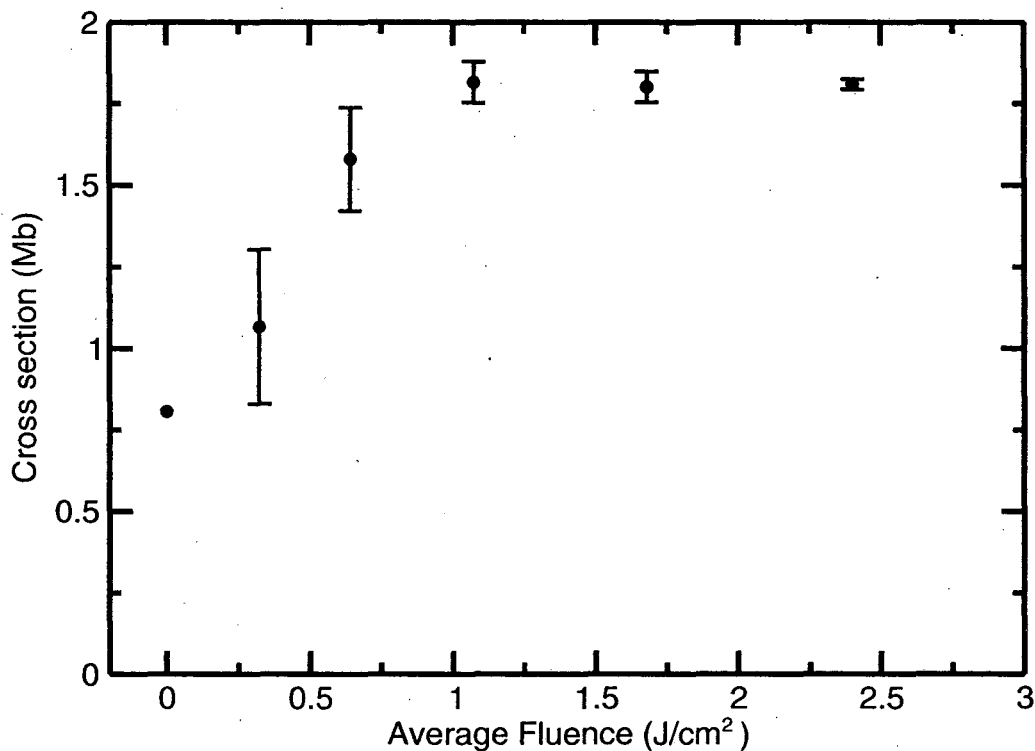


Figure 4.4: Dependence of the pre-edge absorption (averaged over 283–287 eV) at 100 ps after heating as a function of the incident laser fluence.

a function of incident laser fluence. The plot shows that the magnitude of the change in absorption at this energy increases with fluence, approaching a constant at values above 0.7 J/cm<sup>2</sup>. The curve is similar to the fluence dependence of femtosecond ablation crater sizes in bulk HOPG (highly oriented pyroelectric graphite), shown as the upper curve of figure 4.5 (taken from ref. [75]). The fluence threshold for the appearance of these craters was identical to the threshold for optical reflectivity changes from melting of the surface [75]. This strongly suggests that the observed x-ray absorption change results from melting of the carbon target.

The optical self-absorption measurements discussed in appendix B measure a

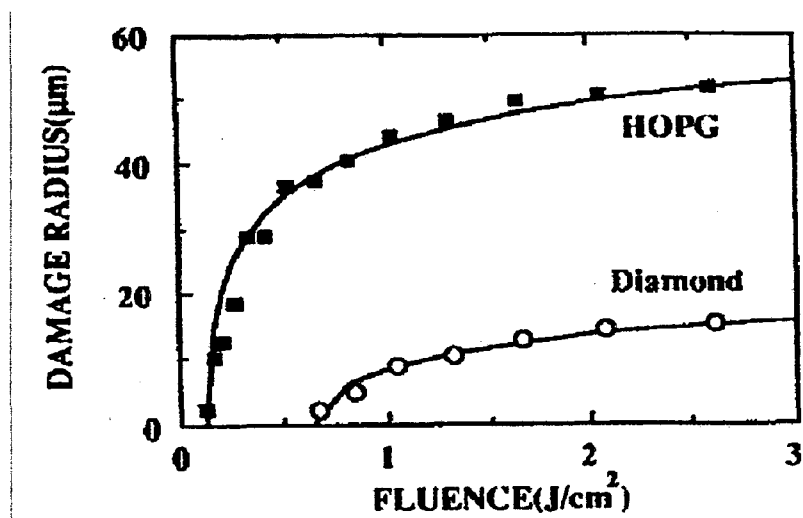


Figure 4.5: The average radius of ablation craters in bulk HOPG and diamond after single shots of a 90 fs, 620 nm laser pulse, taken from figure 1 of ref. [75].

$(37.8 \pm 1.4)\%$  absorption of the incident pulse at a fluence of  $1.5 \text{ J/cm}^2$ . The resulting energy density of  $600 \text{ kJ/mol}$  is comparable to the  $700 \text{ kJ/mol}$  cohesive energy of the solid [17], suggesting that (as with silicon) the fluid is near the critical temperature.

In the amorphous solid, interpretation of the NEXAFS structure relies on application of the “building block” picture, the idea that the absorption spectrum of the material as a whole is really the sum of more basic bonding units. Since x-ray absorption primarily probes the unoccupied states very near the absorbing atom, this model of the NEXAFS spectrum is largely successful even for large molecules. Exceptions to this rule in systems without long-range order typically arise from strong interactions between neighboring antibonding states, also called “conjugation.” This typically results in a splitting of absorption features, but fortunately these splittings are well-documented due to the large volume of data on the various forms of solid

carbon and organic molecules [88].

For amorphous carbon, currently accepted interpretations [88, 26] assign the shoulder in the spectrum at 285 eV to transitions to  $\pi^*$  antibonding states, a collection of narrow resonances ranging in energy from 284 eV to 287 eV. The broader absorption peak at 297 eV is a consequence of promotion to  $\sigma^*$  antibonding states. The strength of these absorption features indicates the proportions of  $\pi$  and  $\sigma$  bonding states in the system and can thus serve as a measure of the average hybridization of the bonding among carbon atoms [26]. The soft a-C solid used for these experiments is primarily  $sp^2$  bonded (measured at 70% for films grown with similar techniques [26]). The sharp increase in the pre-edge  $\pi^*$  peak and the concomitant decrease in the  $\sigma^*$  peak after laser heating indicate a change in the proportion of  $\pi$  and  $\sigma$  bonds consistent with a change from  $sp^2$  to  $sp$  bonded atoms. This conclusion agrees with MD simulations of the bonding of liquid carbon at low densities that predicts a coordination number near 2 [105]. Comparison of the experimental results to these low-density (near 1 g/cc) results from the MD simulations is appropriate since 100 ps of expansion into vacuum is likely to result in a density significantly lower than that of the solid.

The blue-shift and change in shape of the  $\sigma^*$  resonance on melting is understandable in terms of bond length changes and the high level of short range disorder in the high temperature liquid. Both theory and experiment have found an approximate correlation between the energy position of the  $\sigma^*$  resonance and the length of the associated  $\sigma$  bonds [88]. In section 4.4 we will use this correlation to discuss quan-

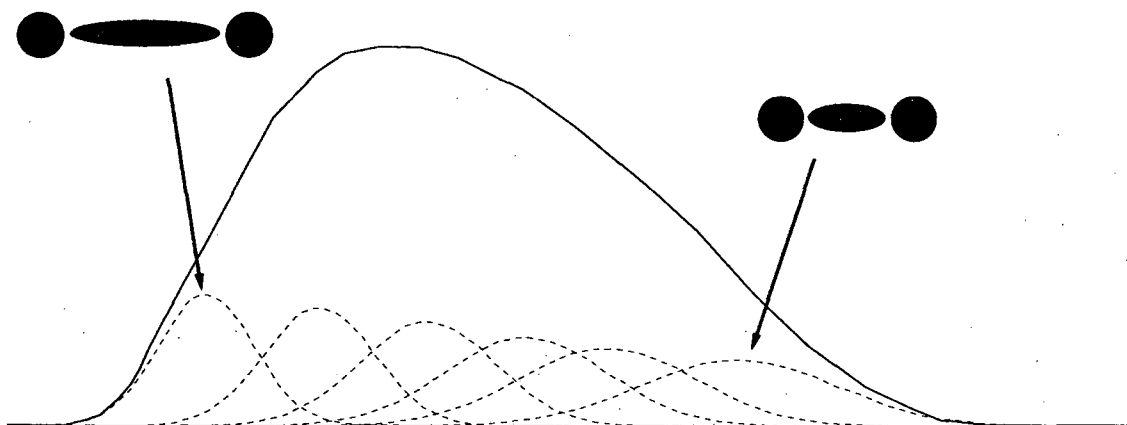


Figure 4.6: Pictorial explanation of the asymmetric  $\sigma^*$  line shape of liquid carbon. At a given moment in time, the high-temperature liquid consists of a wide distribution of  $\sigma$ - $\sigma$  bond lengths. Since the width of the  $\sigma^*$  resonance increases at higher energies due to the shortened lifetime of the final state, the sum of the resonances from these different bond lengths results in an asymmetric profile. This drawing is modeled after figure 7.6 in ref. [88].

titatively the shift and shape change in the peak. Qualitatively, the resonance shift toward higher energies is due to a shorter average  $\sigma$ - $\sigma$  bond length in the liquid. The asymmetry can be understood in terms of the variance of this bond length, both temporally and spatially. The observed resonance is actually the sum of many different resonance peaks, each corresponding to a particular bond length. Since higher energy final states in the continuum have a shorter lifetime and are thus broader in energy, the resulting sum is broad and asymmetric, with a large tail at higher energies as depicted in figure 4.6.

## 4.2 Higher densities: tamping

Although the results plotted in figure 4.3 provide a revealing look at the bonding properties of the liquid at low densities, a more rigorous test of the MD models in ref. [105] requires measurement of the bonding properties of the liquid at known densities in the range of 2–3 g/cc. One way to accomplish this is to probe the sample at times closer to the heating pulse, to observe the liquid before it expands significantly. Femtosecond optical interferometric measurements of the distance between the liquid walls have measured expansion velocities up to 1000 m/s for various materials under similar conditions [83]. Assuming this value for the expansion rate, a 500 Å foil will take approximately 50 ps to expand to nearly twice its initial volume. The 5 ps time resolution demonstrated by the streak camera for silicon absorption should therefore be sufficient to observe the liquid in a mostly unexpanded state, where the density is equivalent to that of the initial solid. Such measurements will be described in section 4.3.

An alternative to using higher time resolution is to somehow delay expansion of the foil so that the 70 ps temporal resolution of the pump-probe technique is sufficient to observe the liquid at high densities. One way to achieve this is to “tamp” the foil on each side with thick layers of a transparent but mechanically stiff material. The laser heats the carbon, creating an essentially instantaneous increase in the elastic stress within the carbon and an outward pressure on the interfaces between the carbon and tamping layers. Because the tamping layers are stiff, this pressure launches a

pair of 1-D acoustic pulses that propagate outward from the carbon through the tamping material, leaving the carbon layer confined to very near its original volume. Eventually the acoustic pulses sent through the tamping layers will result in a volume expansion, but a lower bound for the time when this occurs may be estimated as the time for an acoustic pulse to travel to the outer surface of the tamping layer and back to the carbon:  $2d/v$ , where  $d$  is the thickness of the tamping layer and  $v$  is the sound velocity. A sufficiently thick tamping thickness  $d$  should then delay the expansion of the carbon enough to use the pump-probe methodology to observe the liquid at its initial volume.

For the purposes of this experiment, LiF is in many ways an excellent candidate for a tamping material. Its optical band gap is a very large 14 eV, making the electronic ground state of the solid essentially transparent to the laser pulse, even at high intensities. Figure 4.7 shows the soft x-ray transmission of 7000 Å of LiF over a range of photon energies, including the range of interest for carbon XAS. At the carbon edge the transmission is 0.2, an acceptable sacrifice in photon throughput. The sound velocity in solid LiF is approximately 7 km/s [49], so tamping layers of 3500 Å LiF on each side of the carbon foils should delay the expansion by at least 100 ps.

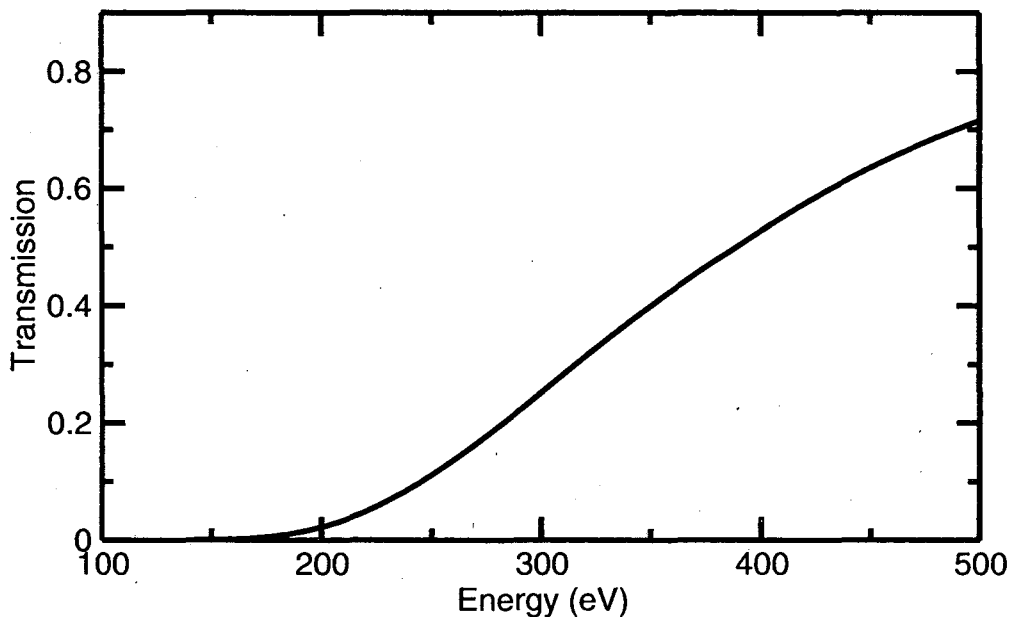


Figure 4.7: Soft x-ray transmission spectrum of 7000 Å thick LiF at solid densities, calculated using ref. [36].

#### 4.2.1 Liquid carbon at 2.2 g/cc

Figure 4.8 is the absorption spectrum obtained for 500 Å soft a-C foils (density 2.2 g/cc) tamped by 3500 Å thick layers of LiF on each side, at a time 100 ps after excitation with an incident laser fluence of 2.1 J/cm<sup>2</sup>. The background absorption of the LiF tamping layers has been subtracted out. The shape of the spectrum is significantly different from that of the untamped foils in figure 4.3. Spectra taken at 200 ps show no significant differences in the *K*-edge structure, suggesting that expansion of the carbon has indeed been delayed by the tamping.

Figure 4.9 plots the dependence of the absorption near 285 eV on incident laser fluence, showing an increase to a nearly constant level beyond a fluence of 2 J/cm<sup>2</sup>. This is a somewhat higher than the saturation value observed in figure 4.4 for untamped

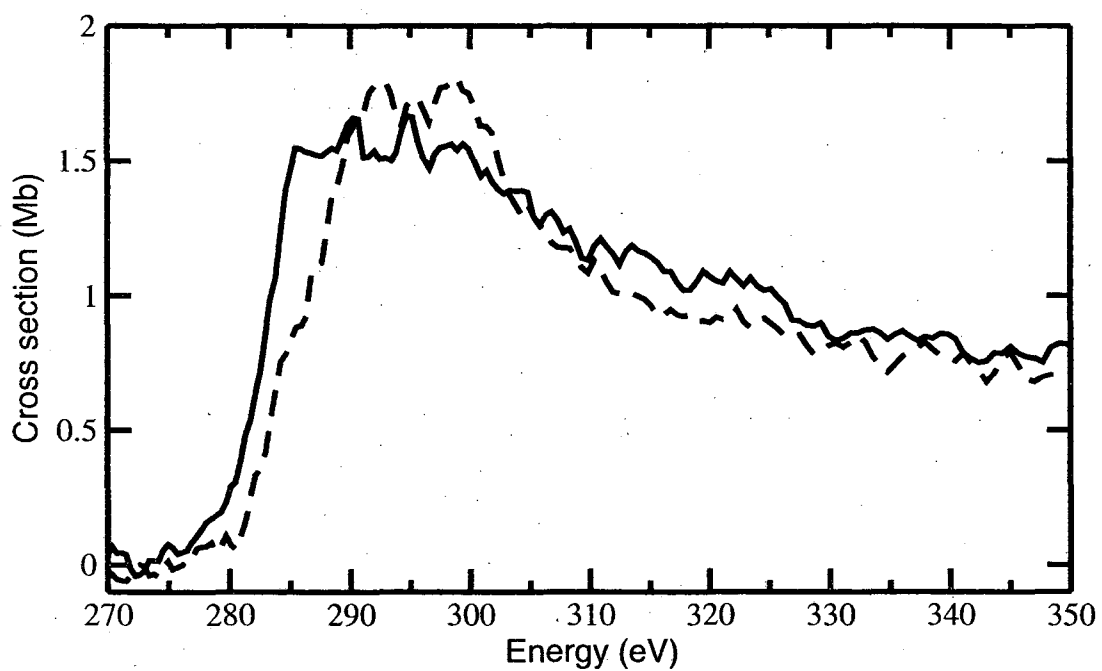


Figure 4.8: Absorption spectrum of a tamped soft carbon foil before heating (dashed line) and 100 ps after excitation (solid red line), with an incident laser fluence of  $2.1 \text{ J/cm}^2$ .

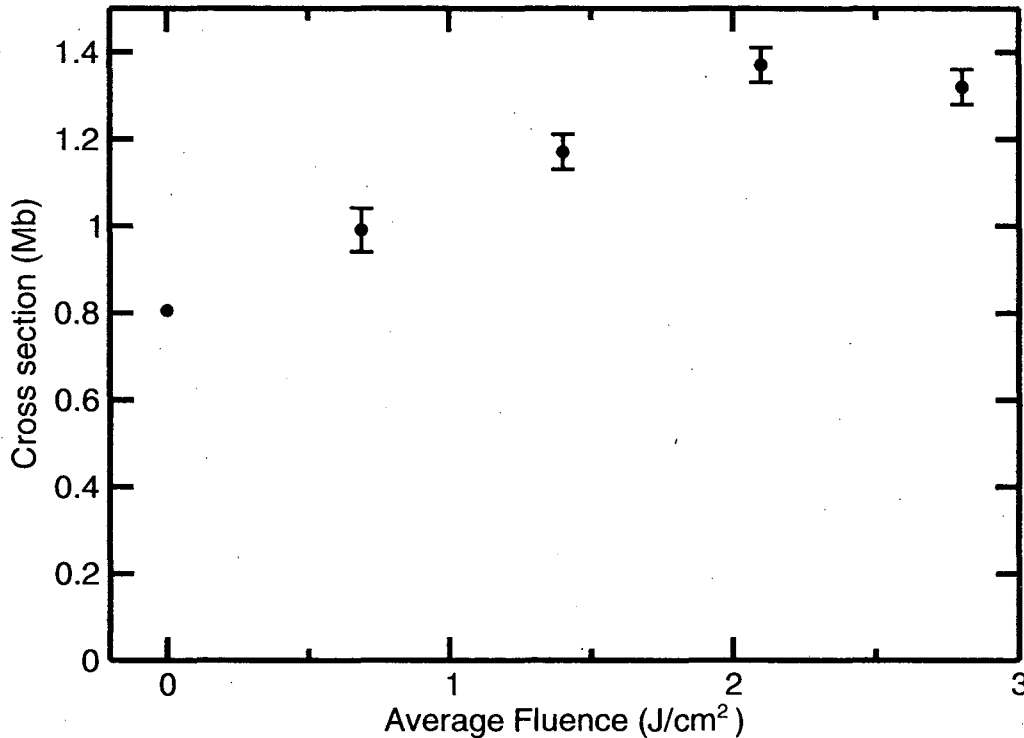


Figure 4.9: Dependence of the pre-edge absorption (averaged over 283–287 eV) for tamped soft carbon foils as a function of the incident laser fluence, at 100 ps after excitation.

foils. The difference is probably from energy loss due to thermal diffusion from the carbon into the tamping layers. The optical self-absorption measurements reported in table B.1 show that the laser pulse absorption of the tamped and untamped foils is only slightly higher with tamping (roughly 60% as opposed to 40–50%), so the initial energy density deposited by the laser should be similar to that for the untamped carbon at a given incident fluence.

The shape of the soft a-C tamped spectrum in figure 4.8 differs from that of the untamped spectrum in several ways, indicating that at this density of 2.2 g/cc the bonding in the liquid is significantly different. The magnitude of the absorption

changes at 285 eV and 300 eV are smaller, and there is no clear distinction between the  $\pi^*$  and  $\sigma^*$  features. The magnitude difference suggests that there are fewer  $\pi$  bonds in the denser liquid, consistent with the higher coordination numbers predicted by MD simulations. The merging of the spectral features is more difficult to understand, but it may be due to an extension of the  $\pi^*$  absorption states to higher energies. Indeed, higher energy, broadened  $\pi^*$  resonances have been observed at energies near 287 eV in amorphous carbon,  $C_{60}$  and benzene [26]. In these materials, these higher-lying  $\pi^*$  states are usually attributed to bond conjugation arising from delocalization of the  $\pi$  states. The merging might also be explained by an increase in the lower-energy  $\sigma^*$  resonances associated with  $sp^3$  bonds.

#### 4.2.2 Liquid carbon at 2.6 g/cc

To investigate the bonding in the liquid at even higher densities, we applied the tamping technique to higher density “diamond-like” carbon (DLC) foils. These amorphous carbon foils (grown by techniques described in ref. [2]) have a number of important properties that make them attractive for a variety of practical uses, but for the purposes of these measurements the only important attributes are the higher density (near 2.6 g/cc) and the presence of a sizeable optical band gap of about 1–2 eV. The  $K$ -edge spectrum of the solid is also somewhat different, with a significantly reduced  $\pi^*$ -to- $\sigma^*$  ratio that reflects the larger proportion of  $sp^3$  bonds in these foils [26].

Figure 4.10 shows the  $K$ -edge absorption spectrum for a 500 Å DLC foil tamped by

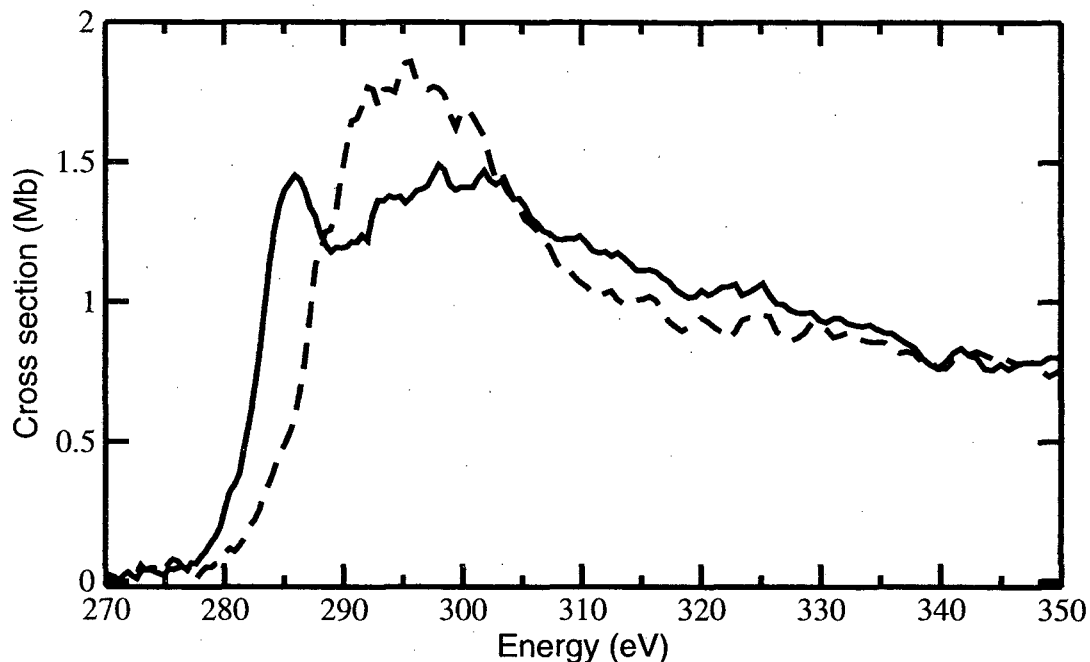


Figure 4.10: Absorption spectrum of a tamped DLC foil without heating (dashed line) and 100 ps after excitation (solid red line), with an incident laser fluence of  $2.1 \text{ J/cm}^2$ .

3500 Å layers of LiF at 100 ps after heating with an incident laser fluence of  $2.1 \text{ J/cm}^2$ . Measurements at 200 ps show no significant changes. The shape and positions of the  $\pi^*$  and  $\sigma^*$  resonances are clearly distinguishable and similar to those observed in the untamped foils. The ratio of the magnitudes of the  $\pi^*$  to the  $\sigma^*$  resonances is smaller, again implying that at these higher densities the bonding consists of fewer  $\pi$  bonds. The clear distinction between the two resonances contrasts with the results of the tamped soft a-C at  $2.2 \text{ g/cc}$ , suggesting that at higher densities the majority of  $\pi^*$  states remain in a narrow range of energies near 285 eV.

Figure 4.11 shows a plot of the fluence dependence of the absorption near 285 eV. At fluences above  $2 \text{ J/cm}^2$  the magnitude of the absorption saturates, suggesting

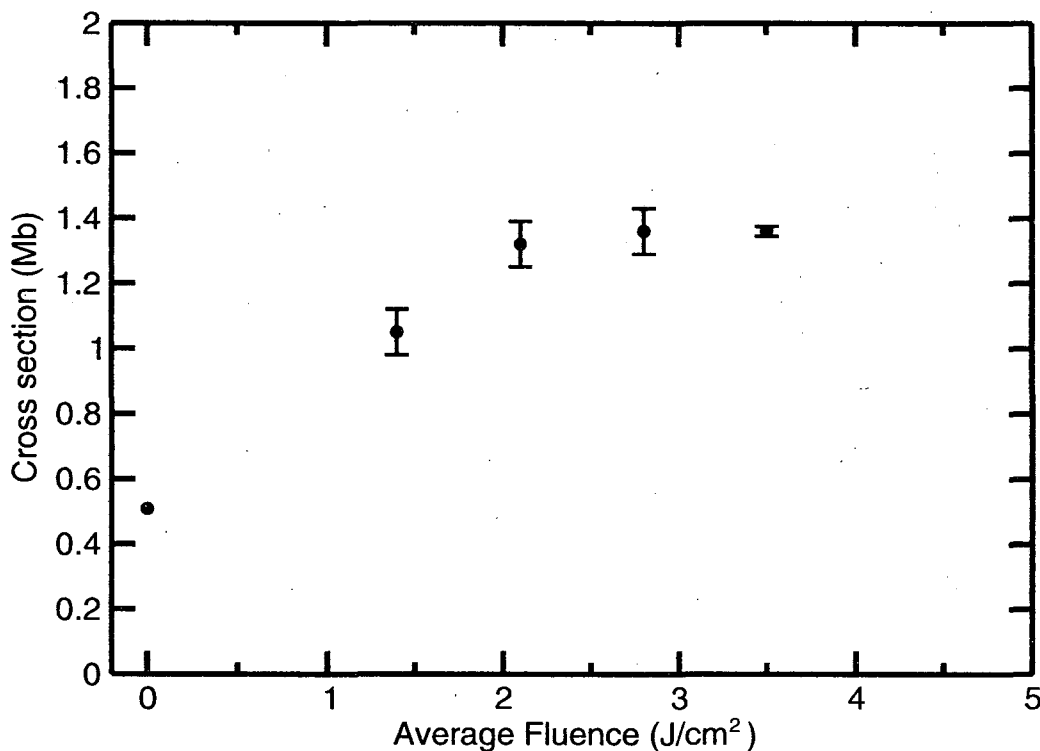


Figure 4.11: Dependence of the pre-edge absorption (averaged over 283–287 eV) for tamped DLC foils 100 ps after heating as a function of the incident laser fluence.

complete melting at these fluences. The optical self-absorption results for the tamped DLC foils are comparable to those of the untamped soft a-C foils, absorbing 40–50% of the incident energy<sup>1</sup>.

### 4.3 Streak camera measurements

Streak camera measurements of the absorption spectrum of 500 Å thick untamped soft carbon foils were performed with 5 ps temporal resolution. Figure 4.12 shows

<sup>1</sup>Unfortunately, a comparison of the absorption to untamped DLC foils was not possible since the available untamped DLC foils completely shattered in response to the mechanical stress from a single laser heating pulse.

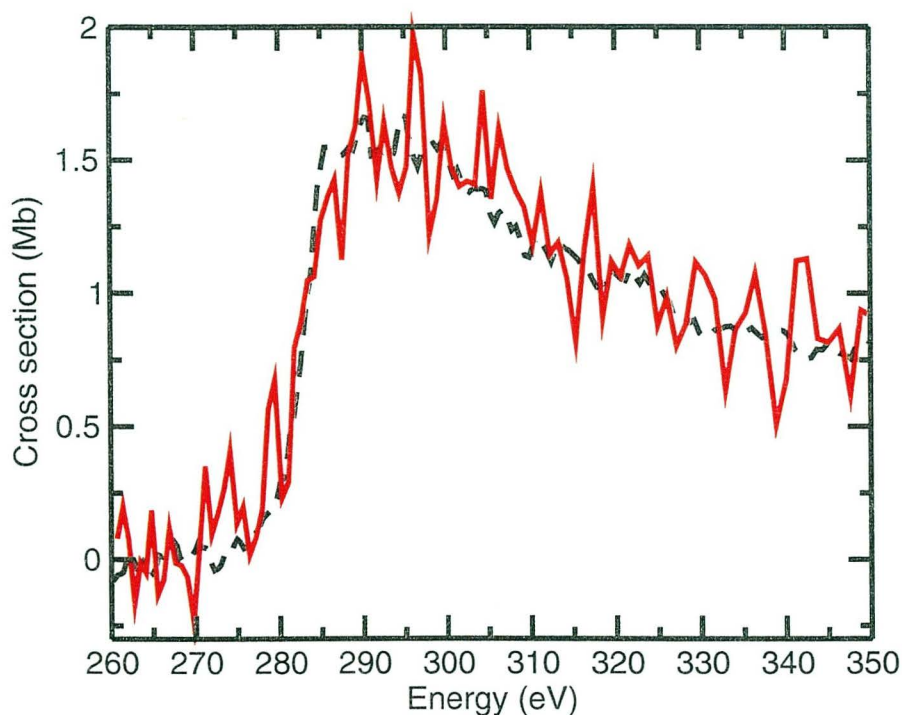


Figure 4.12: Carbon  $K$ -edge absorption spectrum (solid red line), integrated in time from 5–10 ps after heating with an incident laser fluence of  $4.2 \text{ J/cm}^2$ . This data is the average of 324 laser/x-ray shots. The dashed black curve shows the  $2.2 \text{ g/cc}$  tamped liquid spectrum from figure 4.8. The apparent differences at the onset of the  $K$ -edge are due to the focusing properties of the magnetic lens in the streak camera, resulting in slightly worse spectral resolution compared to the pump-probe measurements.

the absorption spectrum integrated in time 5–10 ps after heating. The spectrum is similar to that of figure 4.8, lending further support to the idea that this spectrum really does represent the liquid at densities near that of the initial solid.

One advantage to using the streak camera to observe the liquid with higher time resolution is the possibility of observing changes in the spectrum resulting from the expansion dynamics of the foil. Figure 4.13 shows a plot of the absorption at the  $\pi^*$  and  $\sigma^*$  features as a function of time. After the initial melting, both features appear to remain constant for approximately 5 ps, after which they undergo small oscillations

with a period of 20 ps. The oscillations are out of phase with each other, suggesting that they indicate changes in the relative population of  $\pi$  and  $\sigma$  bonds in the liquid. This time scale of 20 ps is equivalent to the time for an acoustic density wave to travel across a 500 Å distance if we assume a sound velocity of 2.5 km/s, suggesting that these oscillations may be due to changes in the average density of the liquid as acoustic waves induced by the impulsive stress of sudden heating propagate through the liquid and reflect from the surfaces. Hydrodynamic simulations could explore this issue in more detail, and these are indeed planned as future work.

## 4.4 Modeling

To provide some quantitative measure of the bonding changes observed in the liquid at different densities, a slightly modified version of the peak-fitting analysis technique discussed by Díaz *et al.* [26] was applied to the spectra obtained via the pump-probe method. The technique relies on application of the building block picture, discussed earlier in section 4.1. The spectrum is assumed to consist of a sum of a continuum step function and a collection of individual absorption peaks identified with particular types of bonding. This identification is based on comparison with the spectra of reference materials with known carbon bonding structures, namely organic molecules and fullerenes.

In ref. [26], Díaz *et al.* perform this type of analysis on soft a-C and on DLC with the intent of identifying the fraction of  $sp^2$  and  $sp^3$  bonds in each type of solid.

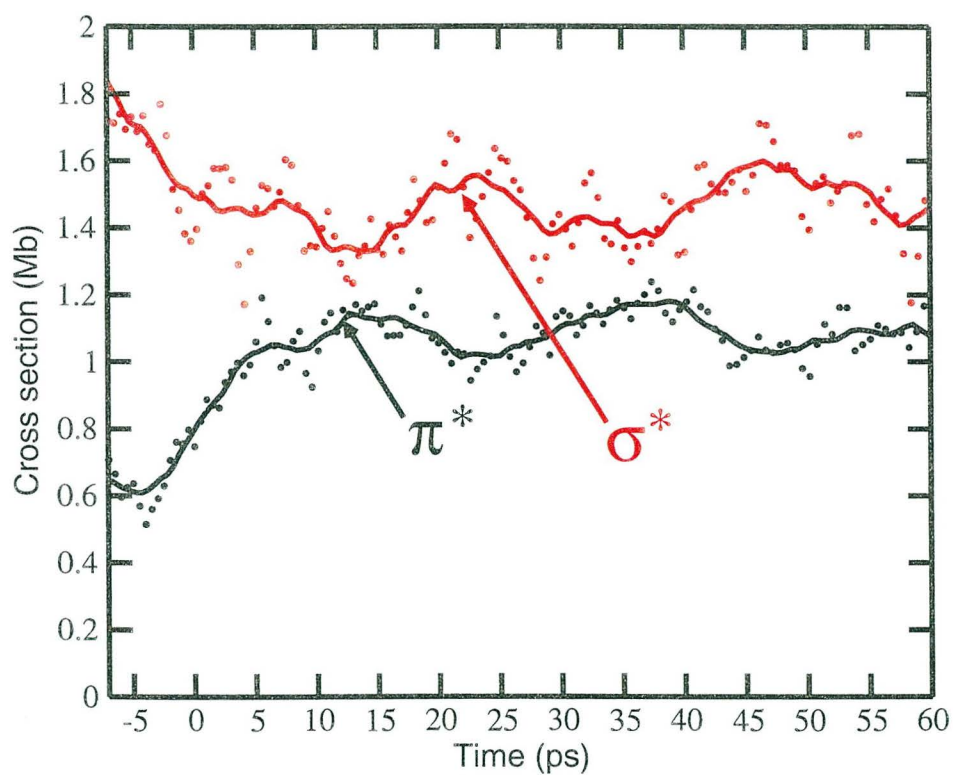


Figure 4.13: Dynamics of the absorption at the  $\pi^*$  (black circles) and  $\sigma^*$  (red squares) bands, showing out-of-phase oscillations in the magnitudes of these absorption features with a period of approximately 20 ps. The  $\pi^*$  absorption was obtained by integrating from 277–287 eV, and the  $\sigma^*$  absorption is integrated from 287–305 eV. The solid lines in the plot show the results of smoothing by a 5 ps boxcar window.

Since the x-ray absorption measurements were performed on static samples, both the signal-to-noise ratio and resolution of these spectra are significantly better than they are for our pump-probe data on liquid carbon. Consequently, a peak fitting analysis of the liquid data cannot be expected to produce as detailed a picture of the bonding as the work of ref. [26] did for the amorphous solids, but nevertheless a modified form of this analysis with more constraints on the fitting parameters should yield some useful information about the types of bonding in the liquid.

Ref. [26] decomposes the spectra of amorphous solid carbon into a continuum step and 7 Gaussian peaks, two of which are identified as  $\pi^*$  resonances at 284.6 eV and 286 eV by comparison with  $\pi^*$  absorption peaks in graphite and  $C_{60}$ . A Gaussian lineshape is the most appropriate here since the broadening of these resonances in amorphous materials is primarily due to disorder. Another component at 288.5 eV appears in these fits, which presents a problem for the analysis since absorption peaks at this energy have been observed for both  $\pi^*$  and  $\sigma^*$  resonances in different compounds. For the analysis of the amorphous solids, ref. [26] assigns it to a  $\sigma^*$  resonance due to distorted  $sp^3$  bonds on the basis of its behavior upon annealing of the samples. The remaining four peaks at energies of 290 eV and higher are unambiguously assigned to  $\sigma^*$  resonances observed in  $sp^3$  and  $sp^2$  bonded carbon structures.

To apply this kind of analysis to the pump-probe data, a much more constrained fitting procedure decomposed each of the spectra into a continuum step function and

a collection of 6 absorption peaks. One peak, representing  $\pi^*$  states, was fixed in energy at 285.5 eV with the width and amplitude varied as fitting parameters. This energy corresponds approximately to the position of the area-weighted average of the 284.6 eV and 286 eV peaks found in the analysis of ref. [26], and it provides a reasonable fit for the  $\pi^*$  peaks observed in the liquid spectra. Two more peaks were set to the energy positions and widths of the two lowest-lying  $\sigma^*$  peaks (at 288.5 eV and 290 eV) from ref. [26] that showed no position dependence on annealing.<sup>2</sup> For the higher energy components (corresponding to short-lived  $\sigma^*$  continuum resonances), the asymmetric Gaussian lineshape from ref. [68] was judged to be a better choice than symmetric peaks at fixed energies, since the position and shape of these peaks are sensitive to bond lengths which can vary significantly from the amorphous solid to the liquids. This lineshape has the form of a Gaussian with an energy-dependent FWHM that varies linearly as  $E \times m + b$ . With the parameters  $m = 0.575$  and  $b = -164.75$  eV, this lineshape has been shown to fit accurately a wide variety of carbon-carbon  $\sigma^*$  resonances above 290 eV for single, double and triple bonds in organic compounds [68]. With  $m$  and  $b$  held at these fixed values, the higher energy portion of the spectrum was fitted with three such asymmetric Gaussian peaks using only the peak photon energy and amplitudes as fitting parameters. These peaks provide only an approximate treatment of the actual lineshapes of the resonances at the very high temperatures of the liquid, but with the noise level of the data a

---

<sup>2</sup>The widths of the peaks were set to the values obtained in ref. [26] added in quadrature to the  $\sim 2$  eV apparent resolution of the spectra.

more refined analysis would not be fruitful. The continuum step was modeled as a step function with linear post-step decay, convolved with a 3 eV wide Gaussian. The position of the step was held fixed to 289.5 eV, the value obtained for amorphous carbon in ref. [26]. The post-edge slope was set to match the slow decay of the cross section observed at energies from 350–400 eV, where all the forms of carbon under study show a very similar dependence of x-ray absorption on photon energy.

Figures 4.14, 4.15, 4.16, 4.17, and 4.18 show plots summarizing the fits to the unheated soft carbon, the unheated DLC, the untamped liquid carbon, the liquid carbon at 2.2 g/cc, and the liquid carbon at 2.6 g/cc. Within the noise level, the accuracy of the fits is acceptable. Table 4.1 summarizes the results numerically in terms of the area under each peak, the total area under the spectrum, and the positions of the three higher energy  $\sigma^*$  peaks.

#### 4.4.1 Analysis of higher-energy $\sigma^*$ resonances

One interesting result of the fits is the movement of the peak positions and change in areas under the three higher energy  $\sigma^*$  resonances. For the solids, ref. [26] assigns the  $\sigma_2^*$  peak near 292 eV to the sum of  $\text{sp}^3$   $\sigma^*$  resonances and conjugated  $\text{sp}^2$  bonds from aromatic rings. These conjugated  $\text{sp}^2$  bonds also contribute to the  $\sigma_4^*$  peak near 302 eV. The  $\sigma_3^*$  peak near 296 eV is from nonconjugated  $\text{sp}^2$  bonds.

These peaks move significantly to higher energies for the fits to the liquid spectra. The presence of  $\text{sp}$  bonded carbon chains as predicted by ref. [105] should cause the

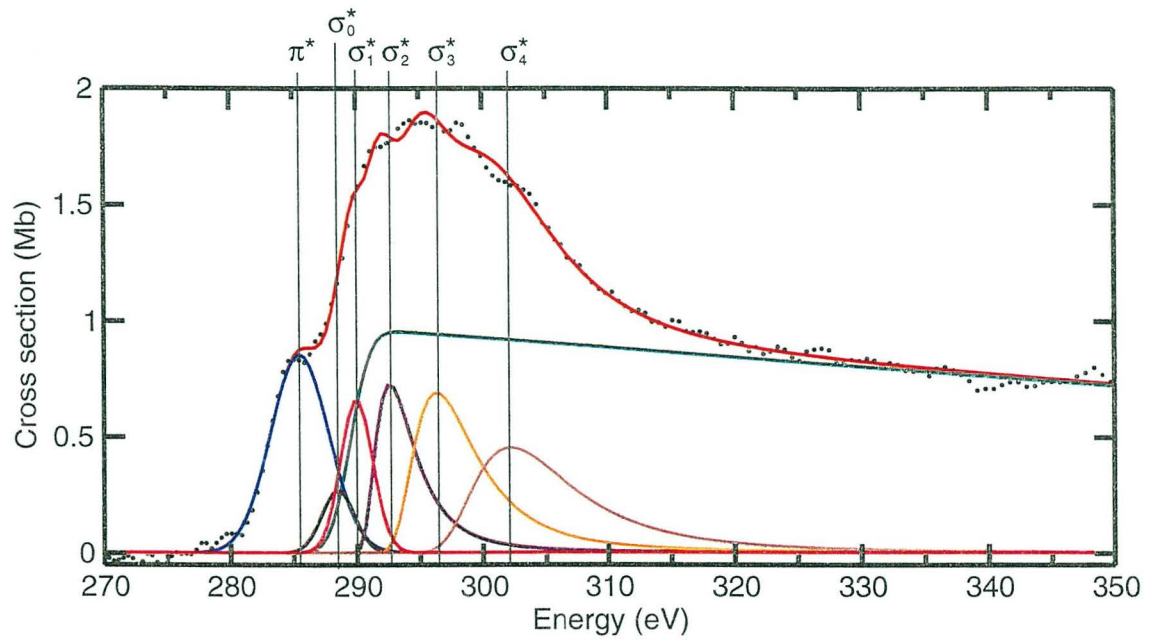


Figure 4.14: Results of fitting to the (unheated) soft amorphous carbon spectrum.

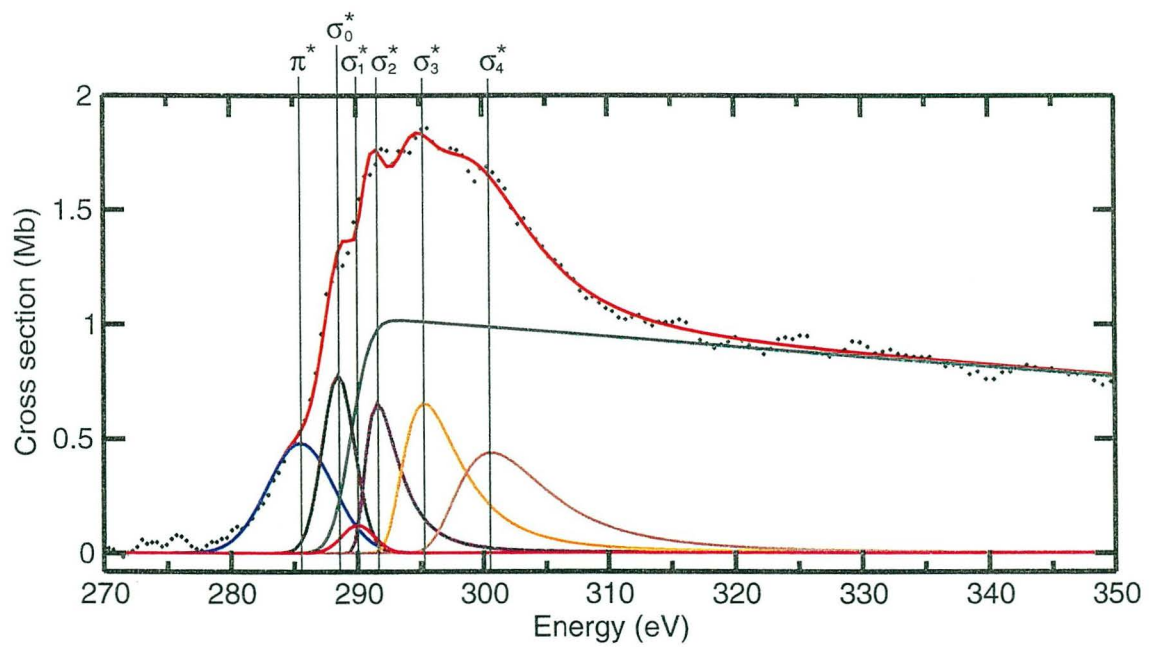


Figure 4.15: Results of fitting to the (unheated) solid DLC spectrum.

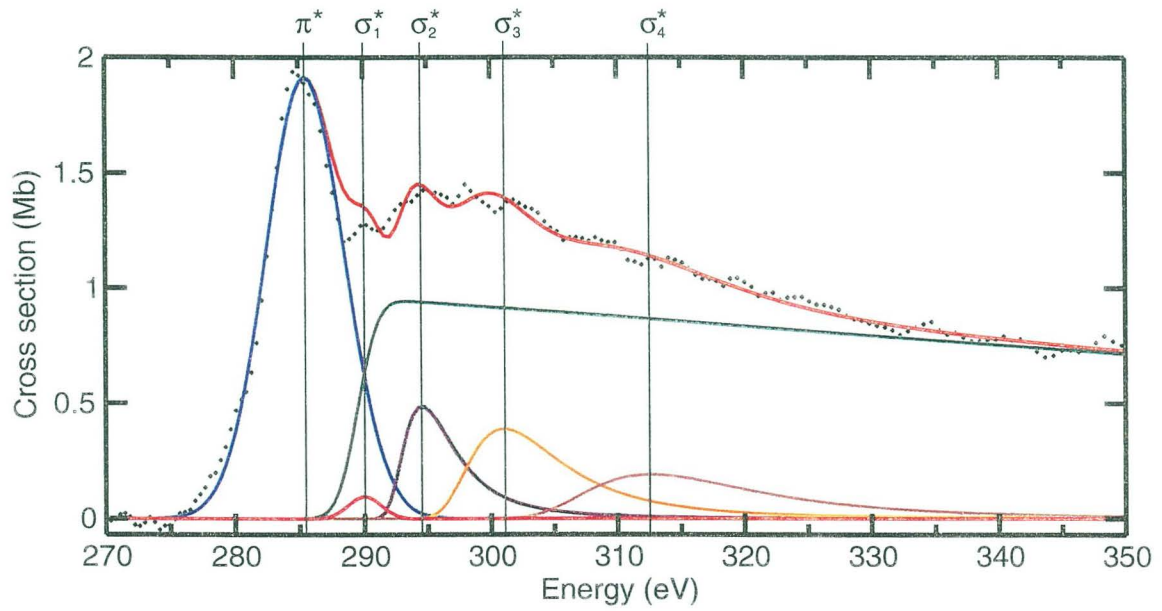


Figure 4.16: Results of fitting to the untamped liquid carbon spectrum.

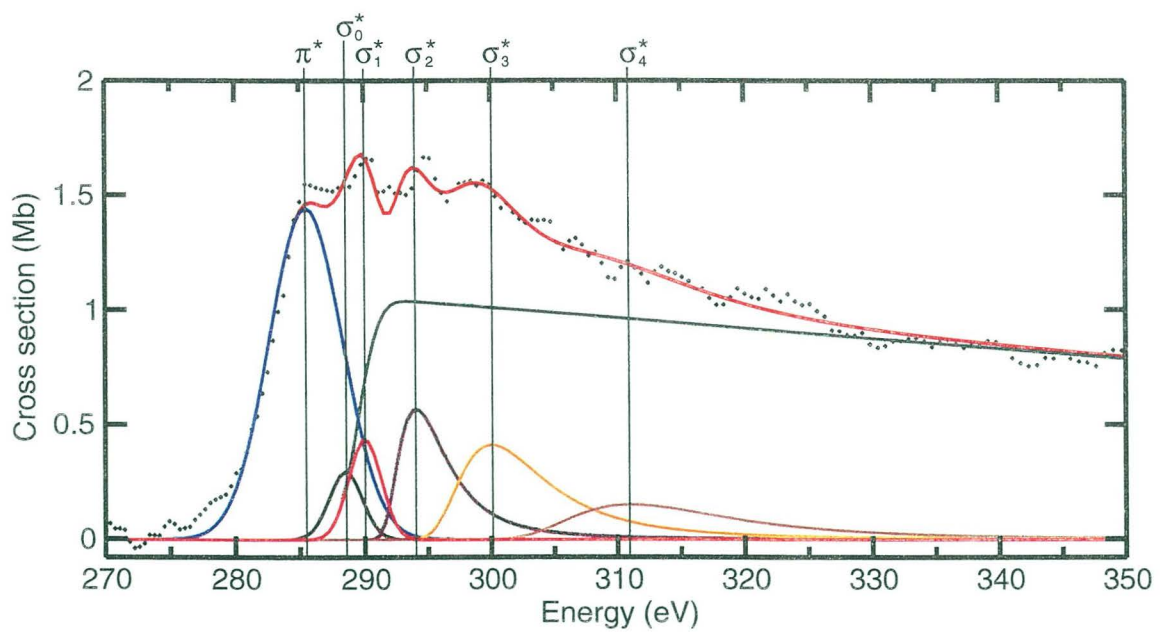


Figure 4.17: Results of fitting to the 2.2 g/cc liquid carbon spectrum.

Material	Area (Mb eV)								Position (eV)		
	$\pi^*$	$\sigma_0^*$	$\sigma_1^*$	$\sigma_2^*$	$\sigma_3^*$	$\sigma_4^*$	$\sigma_{\text{tot}}^*$	total	$\sigma_2^*$	$\sigma_3^*$	$\sigma_4^*$
soft a-C	4.93	0.87	2.11	3.51	5.32	5.54	17.35	104.57	292.6	296.4	302.2
DLC	3.15	2.48	0.39	2.63	4.52	4.81	14.83	105.7	291.6	295.3	300.6
untamped liq.	14.54	0.00	0.31	3.09	4.42	3.84	11.66	107.71	294.6	300.0	312.7
2.2 g/cc liq.	10.19	0.94	1.40	3.39	4.35	2.67	12.94	112.67	294.1	300.0	311.1
2.6 g/cc liq.	9.47	0.64	0.25	2.30	4.57	2.69	10.65	109.49	294.3	300.9	312.9

Table 4.1: Numerical summary of fit results, showing the areas under each peak as well as the total area under the spectrum integrated from 275–400 eV. The positions of the peaks of the asymmetric Gaussians are also listed.

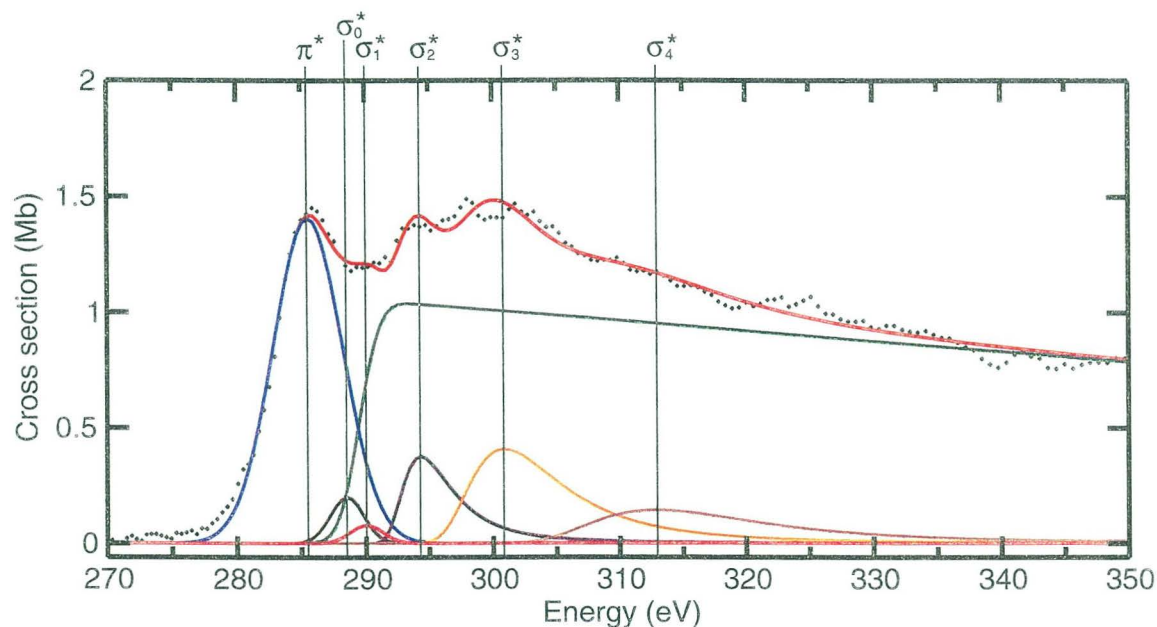


Figure 4.18: Results of fitting to the 2.6 g/cc liquid carbon spectrum.

appearance of  $\sigma^*$  resonances at energy positions similar to those observed in organic molecules with sp bonded carbon chains, such as allene ( $\text{H}_2\text{C}=\text{C}=\text{CH}_2$ ), propargyl alcohol ( $\text{HC}\equiv\text{C}-\text{CH}_2\text{OH}$ ), methylacetylene ( $\text{H}_3\text{C}-\text{C}\equiv\text{C}-\text{H}$ ), 2,4-hexadiyne ( $\text{H}_3\text{C}-\text{C}\equiv\text{C}-\text{C}\equiv\text{C}-\text{CH}_3$ ) and acetylene ( $\text{HC}\equiv\text{CH}$ ). These spectra have  $\sigma^*$  resonances near 294 eV and 310 eV that are associated with this type of bonding. In allene, these features arise from conjugation between the two  $\text{C}=\text{C}$   $\sigma$  bonds [88]. In acetylene, only the resonance at 310 eV appears, suggesting that it is due to the short 1.2 Å  $\text{C}\equiv\text{C}$  bond. Propargyl alcohol, methacetylene, and 2,4-hexadiyne have both resonances, with the lower energy peak from C-C bonds and the higher energy peak from the acetylene-like  $\text{C}\equiv\text{C}$  bonds. A small additional peak appears at 299 eV in 2,4-hexadiyne, apparently due to a 10% shortening of the central C-C bond by conjugation with the adjacent

triple bonds [88]. The large amount of disorder expected in the high temperature liquids under study might also produce spectral features similar the  $\sigma^*$  band of ethylene ( $\text{H}_2\text{C}=\text{CH}_2$ ), which is not sp-bonded but does show a strong absorption feature at 300 eV from its unconjugated C=C bond [88].

For all the liquids, the fits place the  $\sigma_2^*$  peak at very near 294.5 eV, a position which agrees remarkably with the lower energy resonances from conjugated C=C  $\sigma$  bonds and unconjugated C-C bonds observed in the sp-bonded molecules discussed above. The  $\sigma_4^*$  resonance moves to values near 312 eV, similar to the higher energy resonance at 310 eV from C=C  $\sigma$  conjugation and C $\equiv$ C bonds. The  $\sigma_3^*$  component near 300 eV is close to the position of the conjugated C-C bond in 2,4-hexadiyne and the unconjugated C=C bond in ethylene. Of course, the  $\sigma_2^*$  and  $\sigma_3^*$  components of the fit may also contain large contributions from the various resonances that appear in this energy range from the C-C and C=C bonds in  $\text{sp}^3$  and  $\text{sp}^2$  bonding structures, but the new energy position of  $\sigma_4^*$  appears to be unambiguously due to sp-bonding, be it from conjugation between adjacent C=C bonds or from C $\equiv$ C bonds.

Although the peak positions show little dependence on the liquid density, the area under the  $\sigma_4^*$  peak does show a very significant difference between the untamped and tamped liquids. Since this peak serves as an indicator of sp-bonding in the liquid, the fact that the untamped, low-density liquid shows more absorption from this feature does suggest a higher fraction of sp-bonded carbon than in the more dense liquids. The area under this absorption feature in the high density liquids (normalizing to the

total area of the spectrum) is approximately 75% of the area under this peak in the untamped liquid. This gives some indication of the relative fraction of sp-hybridized bonds in the liquids that we will revisit after a discussion of changes in the  $\pi$  bond fraction that we can infer from the fits.

#### 4.4.2 Estimate of $\pi$ bond fraction and local bond structures

To estimate the number of  $\pi$  bonds relative to the number of  $\sigma$  bonds in the liquids, we rely on an application of the important Thomas-Reiche-Kuhn sum rule. This rule states that the sum of the oscillator strengths<sup>3</sup> for a given electron in an atom or molecule to all the other states (both unoccupied *and* occupied) is unity. Assuming that the total p-projected density of unoccupied states is also constant, this implies that the total area under the  $K$ -edge spectrum is the same for all the different forms of structurally disordered carbon under study [26]. Indeed, inspection of the total spectral area integrated from 275–400 eV listed in table 4.1 shows that it is approximately constant.

To use the sum rule to estimate the fraction of  $\pi$  bonding in the liquid, we also need to assume that the oscillator strength is the same for all types of  $\pi^*$  states. Ref. [26] uses this to estimate  $\pi$  bonding in amorphous carbon, with results that agree with measurements by Raman spectroscopy. See appendix D for a thorough justification of this assumption in the disordered systems under study.

---

<sup>3</sup>See appendix D for a definition of the oscillator strength.

material	$\pi^*$ area	$\pi^*$ states/site	$\pi^*$ states/site (ref. [58])
soft a-C	$0.047^{+0.008}_{-0.004}$	$0.70^{+0.12}_{-0.06}$	-
DLC	$0.030^{+0.014}_{-0.004}$	$0.45^{+0.20}_{-0.06}$	-
untamped liquid	$0.135^{+0.002}_{-0.020}$	$2.01^{+0.03}_{-0.30}$	-
2.2 g/cc liquid	$0.090^{+0.007}_{-0.013}$	$1.35^{+0.10}_{-0.20}$	$1.29 \pm 0.04$
2.6 g/cc liquid	$0.087^{+0.005}_{-0.011}$	$1.29^{+0.07}_{-0.20}$	$1.16 \pm 0.09$

Table 4.2: Relative contribution of  $\pi^*$  states to the absorption spectra of solid and liquid forms of carbon, as derived from the fits. The table also lists estimates of the number of  $\pi^*$  states per site, assuming a most likely value of 0.70 for the soft a-C solid. The rightmost column lists the  $\pi^*$  states/site derived from the simulation results in ref. [58]. The errors in these values are based on the estimated uncertainty in the density of the target carbon ( $\pm 5\%$ ).

Provided that the sum rule holds and the oscillator strength of all  $\pi^*$  resonances is constant, we can now estimate the relative numbers of  $\pi^*$  states in each form of carbon by taking the area under the  $\pi^*$  peaks and normalizing by the total area under the spectrum. Table 4.2 summarizes the results.

The quoted errors in the  $\pi^*$  area are based on the idea that the primary source of error is in the mistaken assignment of oscillator strength near 288–290 eV, the region of the spectrum where the  $\pi^*$  and  $\sigma^*$  resonances overlap. The lower bound of the error in the  $\pi^*$  area is set to the integral of the fitted  $\pi^*$  peak over energies above 288.5 eV, the peak position of the lowest  $\sigma^*$  resonance. Similarly, the upper bound of the error is set to the sum of the areas under the sigma resonances and the continuum step for energies below 288.5 eV. This method sometimes gives very asymmetric error ranges (especially in the case of the untamped liquid), but it provides a reasonable

estimate of the actual error in the absorption from  $\pi^*$  states for the liquids. For the solids these errors are probably exaggerated, since the higher quality data of ref. [26] does a good job of identifying resonances in this energy range.

Inspection of the results for the two solids in table 4.2 shows a nearly 60% higher level of  $\pi^*$  contributions in the soft a-C than in the DLC. This agrees with the measurements of ref. [26] that estimate 70% of the sites in their soft a-C samples are  $sp^2$  bonded and 40% of the sites in their DLC samples are  $sp^2$  bonded.<sup>4</sup> Since each  $sp^2$  site contributes one  $\pi^*$  state to the spectrum and  $sp^3$  sites contribute no  $\pi^*$  states, we can make quantitative statements about the average number of  $\pi^*$  states per site if we assume that the soft a-C foils used in the pump-probe experiments are indeed 70%  $sp^2$ . These estimates are listed for each form of carbon in table 4.2, giving a reasonable value of 45% for the  $sp^2$  fraction of the DLC foils. This level of quantitative agreement with other measurements of the  $\pi^*$  bond fraction is an important check of the analysis.

For the liquids there is much more  $\pi$  bonding evident from the fits. The low-density untamped liquid shows nearly 3 times the number of  $\pi^*$  states than does the soft a-C solid. From the rightmost column in table 4.2, we estimate that each site in the untamped liquid contributes an average of 2.01  $\pi^*$  states to the absorption spectrum in agreement with the 2 states/atom expected for purely  $sp$  hybridized bonding. For the tamped liquids, we can compare the data quantitatively to the

---

<sup>4</sup>The fraction was 40% for freshly deposited DLC films, increasing to nearly 60% after annealing.

results of the  $T = 7000$  K tight-binding simulations of ref. [58] (plotted in figure 4.2). Values for the  $\pi^*$  states/atom in the simulations are listed in the rightmost column of table 4.2. Agreement between the simulation and fit results is good for the 2.2 g/cc liquid, with both estimating about 1.3  $\pi^*$  states/atom. At 2.6 g/cc the simulation and fits still agree within the estimated errors, but whereas the simulation predicts fewer  $\pi^*$  states/atom compared to the 2.2 g/cc liquid, the fits do not show a significant change with density.

Another way to help identify the relative numbers of the different bond hybridizations in the liquids is to use the changes in the area under the  $\sigma_4^*$  peak near 310 eV as a signature of the fraction of sp sites. This has an important limitation: although this resonance is unique to the bonding related to sp sites, it is not necessarily present at all such sites if the disorder in the liquid is sufficient to prevent conjugation between adjacent C=C bonds. Another caveat is the ability of the fits to accurately separate absorption from this resonance from the  $\sigma_3^*$  peak. Keeping these drawbacks in mind, recall from section 4.4.1 that the area under the  $\sigma_4^*$  peak for both the tamped liquids is approximately 75% of the area under this peak for the untamped liquids. This would seem to imply that the density of sites with two conjugated C=C bonds and with C $\equiv$ C bonds is (for the tamped liquids) at most about 75% of those in the untamped liquid. Unfortunately, we have no practical way of identifying the density of other types of sp bonds that have lower  $\sigma^*$  resonances because of overlap with sp<sup>2</sup> related absorption. It is interesting to note that although the intensity of this sp related

absorption is about the same for both densities of tamped liquids, the tight-binding simulations predict a large change in the density of 2-fold sites from 45% at 2.2 g/cc to 25% at 2.6 g/cc [58].

## 4.5 Summary and future work

Time-resolved measurements at the  $K$ -edge of carbon have been largely successful in providing an experimental measure of the bonding properties in the liquid at various densities near that of the solid. At low densities, an analysis of the spectra based on fitting to known resonances shows that the low density liquid has is predominantly sp bonded. At higher densities attained by tamping the heated foils the fraction of sp bonded sites is still significant, and the estimated number of  $\pi^*$  antibonding states/atom agrees with the results of published simulations of the liquid structure based on a tight-binding interaction model.

Although the kind of direct theoretical calculation of the absorption spectrum performed for liquid silicon has not yet reached the level of maturity where a meaningful comparison to experiments on liquid carbon is possible, the peak-fitting analysis presented above does provide a quantitative estimate of the changes in the bonding hybridization. A calculation of the unoccupied, p-projected density of states from MD simulations should be possible, providing a more direct comparison to the experimental results. In addition, hydrodynamics simulations could provide additional insight into the small, 20 ps oscillations in the  $\pi$ -to- $\sigma$  bond ratio observed in the

streak camera measurements of the untamped carbon foils.

## Chapter 5

### Conclusion

Time-resolved absorption spectroscopy is a valuable tool for studying the electronic and short-range structural properties of matter under the extreme conditions of very high temperature and near solid densities. The combination of a high power femtosecond laser and a synchrotron bend magnet as described in this work have demonstrated the ability to perform quantitative measurements on the short-range structure and electronic density of states in liquid silicon, as well as the electronic bonding properties of liquid carbon at a variety of densities.

Beyond the very specific discussions of future work given in sections 3.5 and 4.5, there are some more general forward directions for this research. These kinds of experiments would all benefit from a method of experimentally measuring the temperature of the foils at the time the x-rays probe them. This is a difficult problem, but it may be possible by measuring the optical emission from the foil as a func-

tion of time, looking at the intensity of lines from an atom-like impurity. Another possible avenue for future development of these experiments lies in the use of even higher laser fluences to push materials to high enough temperatures to explore the boundary between liquids and plasmas. Current developments in new x-ray sources for time-resolved experiments, namely synchrotron insertion devices and soft x-ray FEL's, offer tremendous improvements in peak x-ray brightness over bend magnet sources. These new sources offer the potential to observe the melting and expansion dynamics of heated solids with greater detail, both temporally and spectrally. The resulting experimental information on the electronic bonding and structural properties in high-energy density materials could offer great insight into the physics of this otherwise mysterious regime.

# Appendix A

## Electronic phase shifter

To facilitate both pump-probe and streak camera measurements, it is desirable to have a way to vary electronically the relative timing of the laser and x-ray pulses. The alternative is to use an opto-mechanical delay line which, while conceptually very simple, is cumbersome to set up and use for very long delays ( $> 10$  ns). The system described here is fairly inexpensive, completely computer-controlled and offers an essentially infinite range of available timing delays.<sup>1</sup>

Conceptually, the “phase shifter” can be divided into three parts: (1) control of the timing of oscillator pulses with respect to the synchrotron bunch timing signal, (2) control of the timing of the amplifier components, specifically the Pockel’s cells and the Q-switch timing of the Quanta-Ray pump laser for the 10 Hz amplification, and (3) the computer program that coordinates these two timings. We will now describe

---

<sup>1</sup>The current implementation requires some manual adjustment of electronic delay boxes for changes larger than  $\sim 100$  ns. This is, however, not an intrinsic limitation of the system but rather a consequence of the fact that experiments rarely need such long delay ranges.

each of these components.

## A.1 Oscillator timing control

In order to vary the timing of the oscillator with respect to the synchrotron, we use an I-Q vector modulator (I. F. Engineering, model QPMX-499) to arbitrarily shift the phase of the 500 MHz synchrotron RF signal that is fed into the phase-locked loop described in section 2.2.1. Figure A.1 illustrates the basic working principle of the modulator. The sinusoidal RF input is first split into two signals, one a simple copy of the input and the other a  $90^\circ$  phase shifted copy (i.e. the first derivative). Each of these signals is attenuated and/or inverted individually, the resulting amplitude proportional to the voltage on the inputs I (for the direct copy) and Q (for the  $90^\circ$  shifted copy). These signals are then added together and serve as the output of the modulator. To understand how to use this device to control the relative phase of the input and output RF signals, suppose that the input voltage waveform is given by

$$\Re [V_0 e^{i\omega t}], \quad (\text{A.1})$$

where  $\Re[\dots]$  denotes the real part of the expression in brackets,  $t$  is time,  $i = \sqrt{-1}$  and  $2\pi\omega = 500$  MHz. The output of the modulator can be mathematically expressed as

$$\Re \left[ V_0 \left( \frac{I}{A} e^{i\omega t} + \frac{Q}{A} e^{i(\omega t + \pi/2)} \right) \right], \quad (\text{A.2})$$

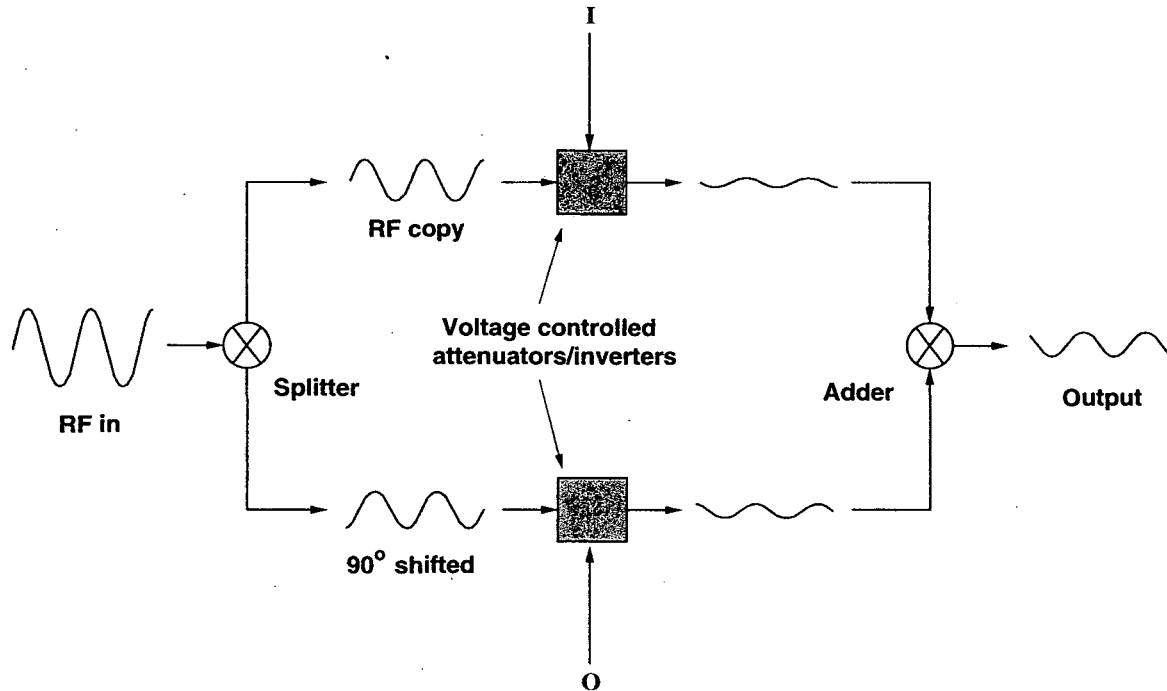


Figure A.1: Functional schematic of the I-Q vector modulator (phase shifter).

where  $A$  is a constant. We can rewrite this as

$$\Re \left[ \frac{V_0}{A} (I + Qi) e^{i\omega t} \right]. \quad (\text{A.3})$$

From this expression it is evident that the complex vector  $I + Qi$  determines the amplitude and phase of the modulator output. Figure A.1 shows a graphical representation of this relationship. If the inputs  $I$  and  $Q$  are chosen such that  $|I + Qi|$  is constant, we can use these inputs to vary the phase of the output continuously from 0 to  $2\pi$ .

In our system, the  $I$  and  $Q$  inputs to the modulator are provided by an SRS245 DAQ module (Stanford Research Systems), connected to a computer via an RS232 serial cable. The algorithm for determining how to set  $I$  and  $Q$  to achieve a desired

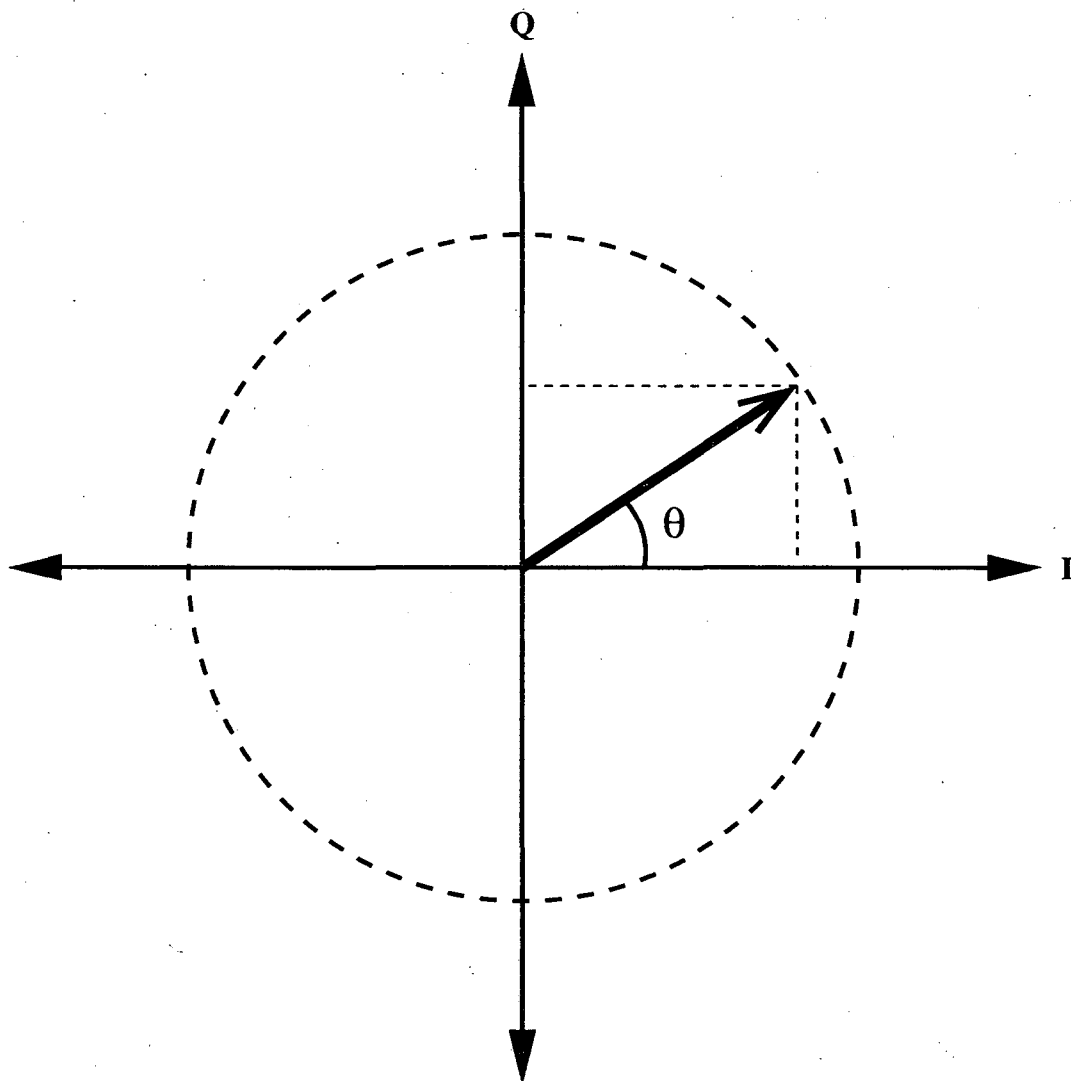


Figure A.2: Relationship of inputs I and Q to the phase shift  $\theta$ .

timing will be detailed in A.4.

## A.2 Amplifier timing control

Although proper use of the I-Q vector modulator can make arbitrary changes to the timing of oscillator pulses with respect to the synchrotron, the timing of the laser system as a whole depends also on the firing time of the amplifier pump lasers and the timing of the Pockel's cells in the regenerative amplifier. These amplifier timings are controlled by a series of SRS DG535 delay generators, as outlined in section 2.2.2. These delay generators all have GPIB ports and can easily be controlled by a computer. The current implementation of the control system regulates only the timing of the Pockel's cells and the Q-switch of the Quanta-Ray 10 Hz pump laser, although future extensions can easily control the firing time of the Merlin 1 KHz lasers and the lamp of the Quanta-Ray. Due to the long lifetime (several hundred nanoseconds) of excited Ti:Sapphire crystals, these timings are not particularly critical if only small  $\sim 10$  ns changes to the timing of the system are desired.

## A.3 Calibration

Although the operation of the I-Q modulator is nominally linear in the inputs voltages I and Q for magnitudes less than 1 V, in practice this is only approximately true. We must therefore calibrate the voltages supplied to I and Q to the actual

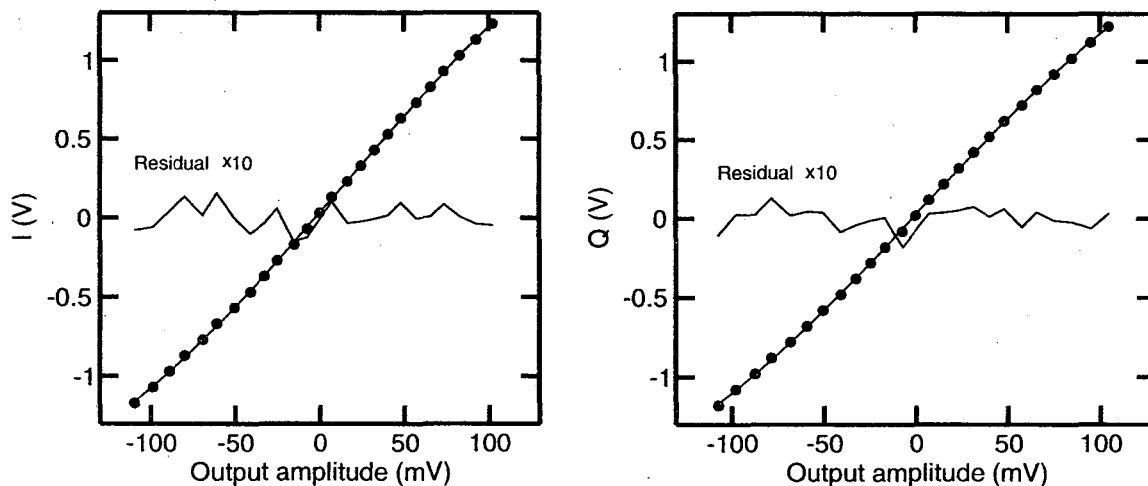


Figure A.3: Plot of the I and Q pin voltages required for various RF amplitudes. For the plot of I voltages, the Q pin was fixed at  $Q_0 = 0.02$  V, and for the Q voltages the I pin was set to  $I_0 = 0.03$  V. A cubic fit to the curves is also plotted, along with the residuals of the fits (multiplied by 10 for visibility).

output signal.

First, the input offsets  $I_0$  and  $Q_0$  to I and Q were determined experimentally by varying the voltage applied to both pins until the output was completely attenuated. These voltages set the position of the origin of the I-Q circle traced by the attenuator as the phase varies.

Next, the voltage on one pin is fixed at its “zero” level ( $I_0$  or  $Q_0$ ) and the output amplitude is measured as a function of the voltage applied to the other pin. Figure A.3 shows plots of the I and Q voltages for various RF output amplitudes, along with fits of these curves to a cubic polynomial. We use the results of these fits in the computer code to calculate the corrected I and Q voltages required to achieve a desired amplitude and phase of the RF output.

Figure A.4 shows the phase accuracy of the system after incorporating these cor-

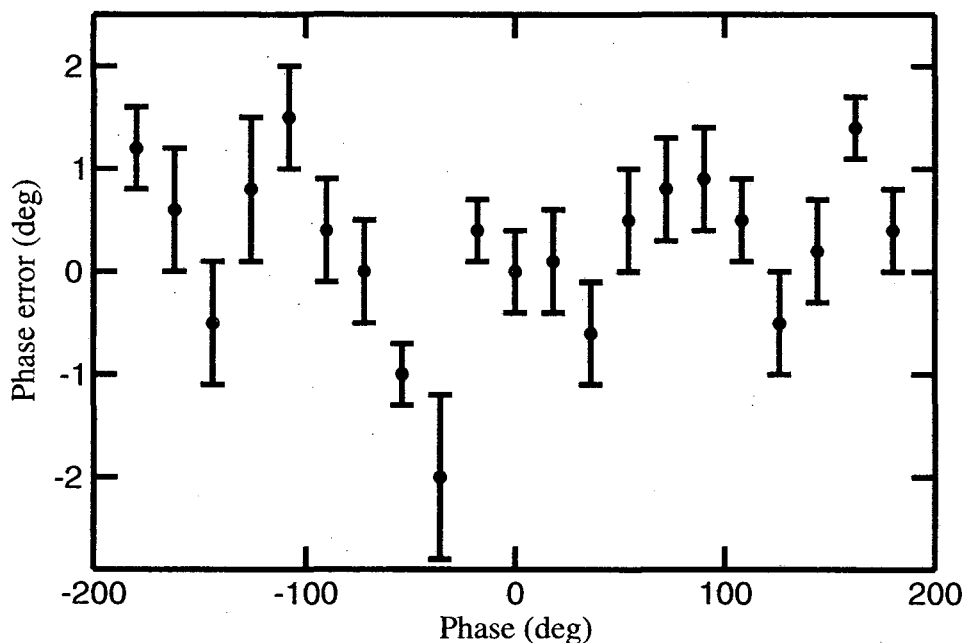


Figure A.4: Plot of the phase accuracy of the system for a range of phases from  $-180^\circ$  to  $180^\circ$ , demonstrating an accuracy of approximately  $\pm 1^\circ$ , or  $\pm 5$  ps.

rections, for various phase shifts. The amplitude of the output is not plotted, but it was constant to within  $\pm 1.5\%$  over the entire range.

## A.4 Overview of computer control programs

Programs for control of the laser timing are written primarily in C on a Debian GNU/Linux PC platform. The job of these programs is to provide a set of tools to easily change the timing of the entire laser system, via either local or remote (ethernet) control. Special care has been taken to ensure the accuracy and reliability of these tools, keeping in mind that the same computer and hardware must be shared with the auxiliary slow-feedback loop for the oscillator cavity described in section 2.2.1.

See appendix E for a listing of the actual code used to control the timing.

For timing accuracy and repeatability, the programs rely on the concept of a fixed “reference timing” of the laser system: an absolute setting of the I and Q inputs of the vector modulator, paired with a set of known delays on the SRS DG535 delay generators that set the timings of the Pockel’s cells and (for the 10 Hz system) the Q-switch of the YAG pump laser. The program assumes that under these and the present timing conditions of the laser system, the laser operates normally. The timing “goal”  $\Delta t$  is always specified in nanoseconds with respect to the reference timing. To change the laser timing, the program first varies the I and Q inputs of the modulator smoothly in phase until the timing changes by  $\Delta t \bmod 12 \text{ ns}$  (changing the oscillator timing by a maximum of 6 ns in either direction). The program then changes the SRS DG535 timings to the appropriate reference timings plus  $\Delta t$ . An example will help to illustrate this idea.

Suppose that the laser is currently operating successfully with a  $I = 1 \text{ V}$  and  $Q = 0 \text{ V}$ , the timing of the Pockel’s cells is set to 6000 ns, and the Q-switch of the YAG is 1000 ns. Now we want to make the laser fire three nanoseconds later. First, the program smoothly varies  $I$  and  $Q$ , keeping the output amplitude of the modulator constant as the phase changes by  $3\text{ns} \times 360^\circ/2\text{ns} = 540^\circ$ . Now the oscillator pulses are at the correct timing, so next the program simply corrects the amplifier timing to make the Pockel’s cells fire at 6003 ns and the YAG Q-switch at 1003 ns. Now the entire laser system is set to produce pulses at the new timing.

For the phase shifter programs to share the GPIB and serial port hardware drivers with the oscillator slow-feedback loop, the programs use special "lock" files to ensure that neither program uses the hardware at the same time. Whenever the user tries to use the phase shifter, the program will check for the presence of one of these files and, if present, will wait until the file disappears. While the program is running, it too creates a lock file to prevent other programs from using the hardware.

## Appendix B

### Optical self-absorption

An important parameter in characterizing the laser-excited states of matter created in these experiments is the amount of energy delivered to the foil by the femtosecond laser pulse. Measuring the energy of the pulse transmitted and reflected by the foil and subtracting that from the total energy of the pulse provides a way to deduce this quantity.

Since the transmittance and reflectance of the foil can be diffuse, accurate measurement of these quantities requires an experimental setup that captures light from as large a solid angle as possible. An integrating sphere is well-suited to these kinds of measurements. The sphere we use is simply a 15 cm diameter hollow sphere with several holes (called “ports”) on the surface, coated on the inside with a highly reflective but diffuse material.

To understand how the integrating sphere works, consider radiation exchange

between two differential surfaces  $dA_1$  and  $dA_2$  along the inner surface, shown in figure B.1. Assuming that every point on the sphere emits radiation uniformly in all directions, the amount of light that travels from  $dA_1$  to  $dA_2$  is simply proportional to the product of the areas after projection onto a plane perpendicular to the line joining them, divided by the square of the distance  $S$ :

$$dF_{1 \rightarrow 2} = \frac{dA_1 dA_2 \cos \theta_1 \cos \theta_2}{\pi S^2}, \quad (\text{B.1})$$

where  $dF_{1 \rightarrow 2}$  is defined by this equation as the fraction of energy emitted from  $dA_1$  that arrives at  $dA_2$ . Elementary trigonometry tells us  $S = 2R \cos \theta_1 = 2R \cos \theta_2$ , so we may simplify equation B.1 as

$$dF_{1 \rightarrow 2} = \frac{dA_1 dA_2}{\pi R^2}. \quad (\text{B.2})$$

Note that this depends *only* on the areas of the two differential elements and the radius of the sphere, and it is completely independent of their position along the surface of the sphere. The radiant flux seen by any point within the sphere surface is thus a constant.

We exploit this property of the sphere to perform measurements of the transmission and total (i.e. specular + diffuse) reflectivity of the foils. To measure the transmission (i.e. scattering in the forward half-space of the foil), we use the geometry of figure B.2. The laser (focused to a point just before the sample) passes through the foil, situated at an entrance port to the sphere. The directly transmitted beam strikes the foil on the other side of the sphere, scattering uniformly off of the diffuse

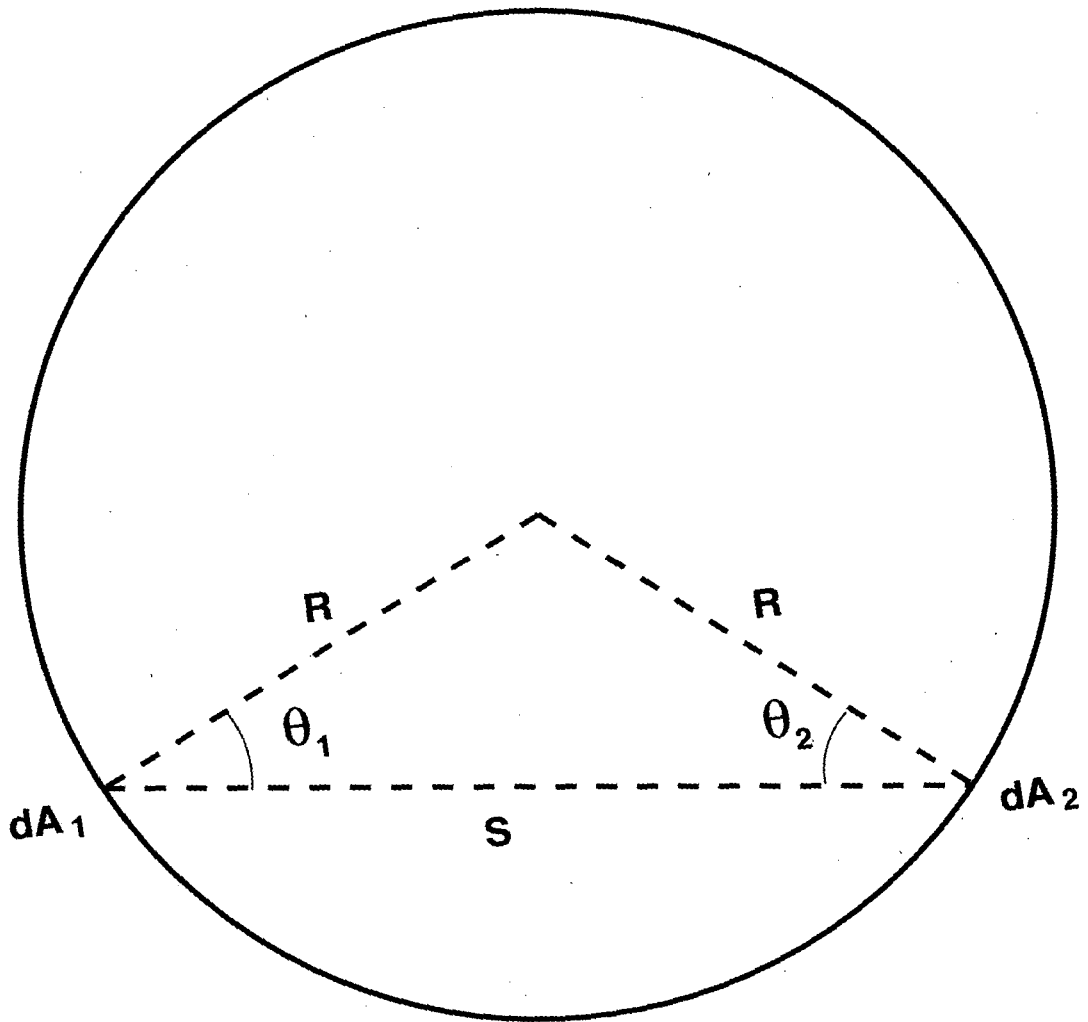


Figure B.1: Radiation exchange between two points in an integrating sphere.

reflective coating. To measure the integrated flux after several reflections from the sphere walls, a lens images a section of the wall of the sphere onto a diode. The ratio of the signal on the diode with and without the foil gives the transmission.<sup>1</sup> Since the angular integration qualities of the sphere rely on the assumption that the light has reflected from the inner wall of the sphere a sufficient number of times to reach a steady-state condition, it is important to restrict the diode from detecting light rays that have undergone only a few reflections. Most of the light entering the sphere strikes the wall opposite to the entrance port, so a reflective barrier (a "baffle") between this point and the imaged portion of the wall helps to reduce the contribution from rays reflecting only twice from the sphere wall.

Figure B.3 shows the setup for reflectivity measurements of the foils. The setup is similar to that for the transmission measurements, but here a mirror on a swivel "flipper" mount is used as a reflectance standard to compare with the foil reflectivity. Contributions to the signal from the wire mesh supporting the foil are also measured by striking the hole left behind in the foil with a second laser pulse, and the result is subtracted from both the with-foil reflectivity signal and the reflectance standard before taking the ratio to calculate the reflectivity. Note that in figure B.3 the baffle is placed so that it blocks the line of sight between the imaged section of the interior and the spot illuminated by specular reflection from the foil, the largest contribution to intensity in the sphere.

---

<sup>1</sup>In practice, the transmission through the wire mesh left behind after ablating the foil is used as a transmission standard, so that transmission losses from the mesh do not affect the results.

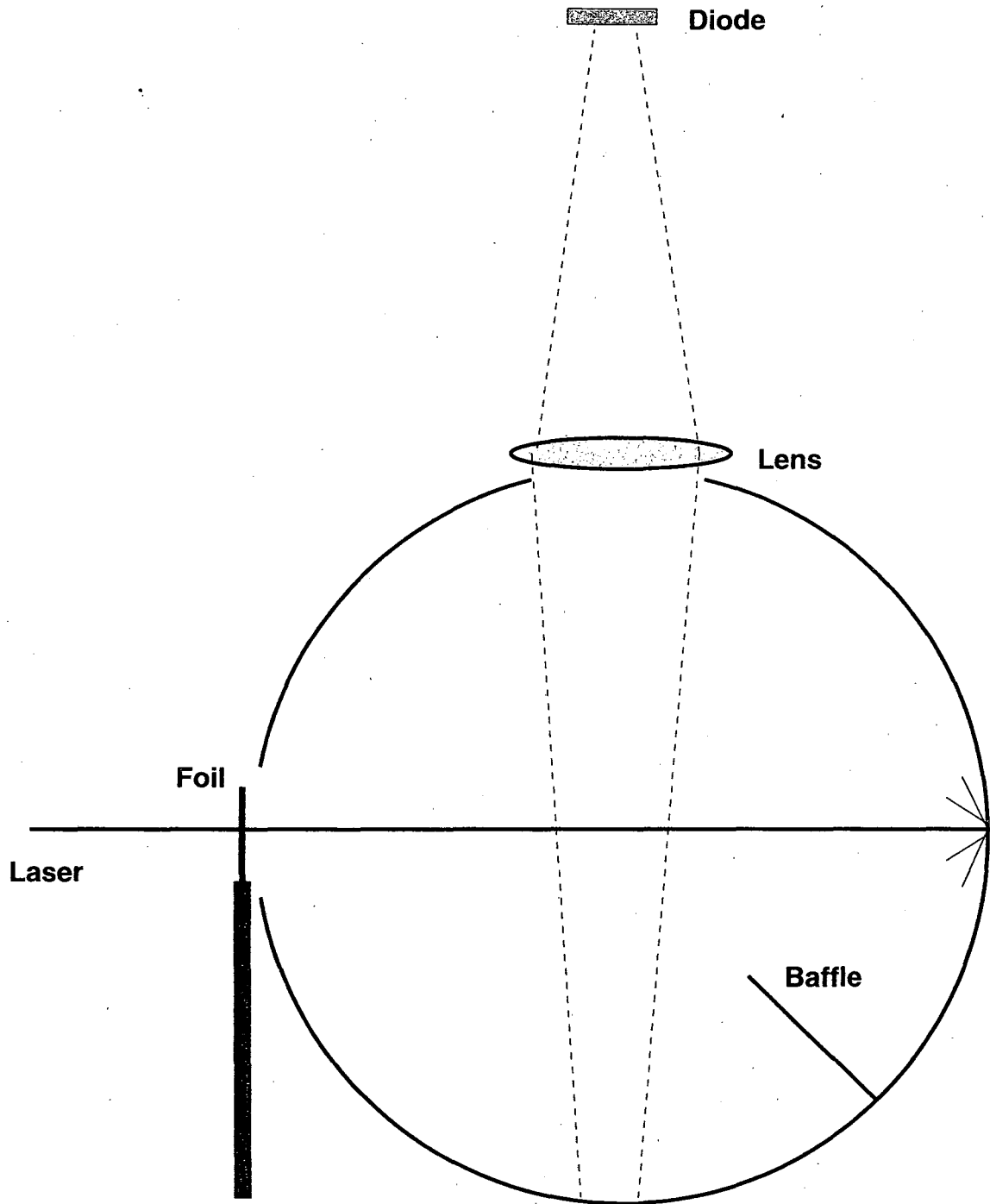


Figure B.2: Optical self-transmission measurement setup

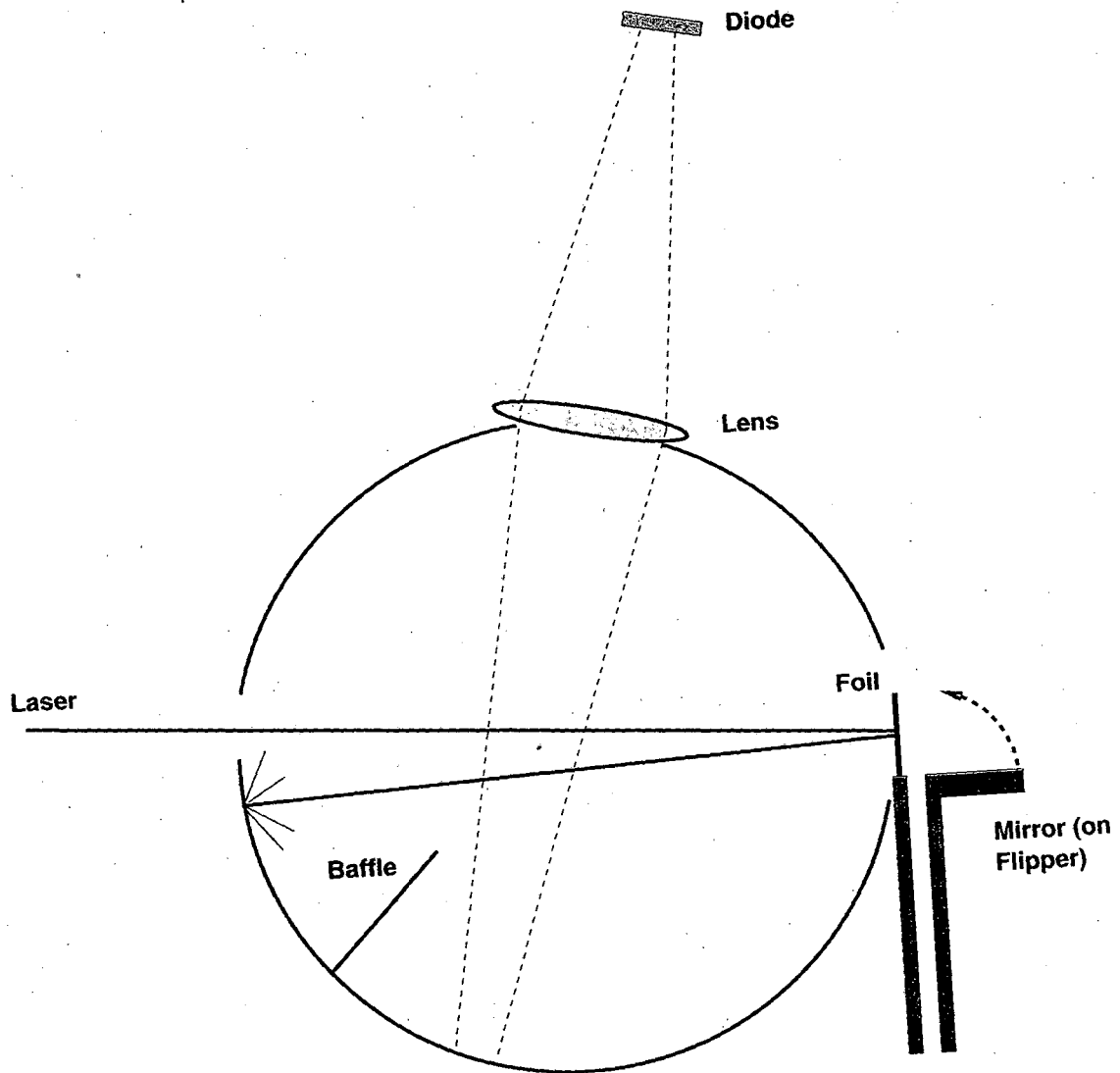


Figure B.3: Optical self-reflectivity measurement setup. The “flipper” mirror provides a reflectance standard.

Foil	Ave. fluence (J/cm <sup>2</sup> ) ( $\pm 10\%$ )	% Trans.	% Refl.	% Abs.
Silicon (500Å)	0.74	$7.18 \pm 0.10$	$55 \pm 4$	$38 \pm 4$
Silicon (1000Å)	0.74	$5.6 \pm 0.2$	$53.6 \pm 1.0$	$40.8 \pm 1.0$
Soft a-C (500Å)	1.5	$27.7 \pm 0.8$	$34.5 \pm 1.4$	$37.8 \pm 1.4$
	3.0	$21.6 \pm 1.4$	$32 \pm 3$	$46 \pm 3$
	6.0	$20.6 \pm 0.9$	$31.7 \pm 0.9$	$47.7 \pm 1.3$
Tamped soft a-C (500Å)	1.5	$30.4 \pm 0.9$	$11.9 \pm 0.9$	$57.7 \pm 1.3$
	3.0	$26.5 \pm 0.8$	$6.5 \pm 0.9$	$67.0 \pm 1.3$
	6.0	$27.3 \pm 0.7$	$9.5 \pm 0.6$	$63.2 \pm 0.9$
Tamped DLC (500Å)	1.5	$41 \pm 2$	$20 \pm 2$	$40 \pm 3$
	3.0	$36.8 \pm 1.4$	$20.4 \pm 1.6$	$43 \pm 2$
	6.0	$33.2 \pm 1.7$	$21 \pm 3$	$46 \pm 3$

Table B.1: Results of optical self-absorption measurements.

Table B.1 summarizes these measurements on the foils used in the reported x-ray experiments. At the fluences used in these experiments, all the foils absorb a significant fraction of the incident radiation.

## Appendix C

### Grating spectrograph

Figure C.1 shows a sketch of the grazing incidence grating spectrograph used to analyze the spectrum of x-ray transmission through the heated foils. X-rays from the sample first encounter a narrow, adjustable width entrance slit (typically set to 150  $\mu\text{m}$ ). Next, a gold-coated mirror horizontally focuses the x-rays from the sample position onto the detector. After this horizontal mirror, the x-rays reflect from a spherical gold-coated mirror and then the plane grating itself, both of which in combination vertically focus an image of the entrance slit onto the detector for the wavelengths of interest.

The position of the vertical slit image from the spherical mirror alone is given by

$$\frac{1}{r_0} + \frac{1}{r} = \frac{2}{R \cos \gamma}, \quad (\text{C.1})$$

where  $r_0$  is the distance from the entrance slit to the mirror,  $r$  is the distance from the mirror to the image,  $R$  is the radius of the mirror (33 m), and  $\gamma$  is the angle of

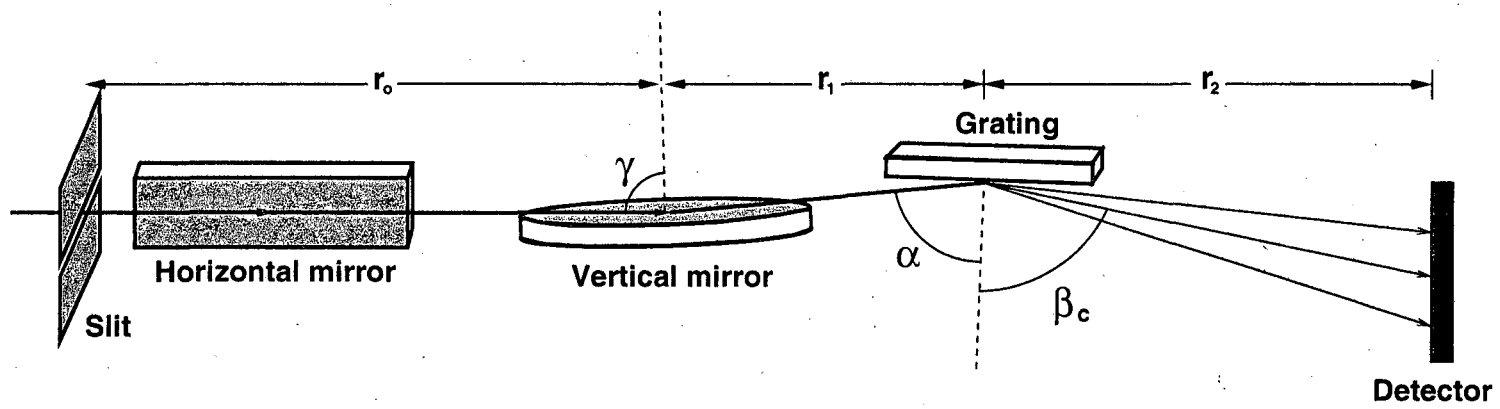


Figure C.1: Sketch of grating spectrograph, showing angles relevant to vertical focusing and spectral calibration.

x-ray incidence on the mirror. Note that we can bring the focus to nearly arbitrary positions by tilting the mirror and varying  $\gamma$ . In this instrument,  $r > r_1$ , where  $r_1$  is the distance from the spherical mirror to the grating.

The grating causes perfect focusing of this intermediate image onto the detector if the distances and angles meet the “plane grating focusing condition”

$$\frac{r_2}{r - r_1} = \left( \frac{\cos \beta}{\cos \alpha} \right)^2, \quad (\text{C.2})$$

where  $\alpha$  and  $\beta$  are the angles of incidence and diffraction, respectively, and  $r_2$  is the distance from the grating to the image plane (i.e. the detector) [69]. The grating equation

$$\frac{m\lambda}{d} = \sin \alpha - \sin \beta, \quad (\text{C.3})$$

where  $m$  is the order and  $d$  is the spacing between grooves in the grating, gives the relationship between x-ray wavelength  $\lambda$  and the grating angles. Together, these equations define the conditions for perfect vertical focusing of the entrance slit onto the detector.

The original design of the spectrograph uses a varied line-spaced (VLS) grating, where the groove spacing  $d$  is not constant but instead varies slightly along the length of the grating to achieve the perfect focusing condition for two different wavelengths  $\lambda_1$  and  $\lambda_2$  with  $r_0 = 87.4$  cm,  $r_1 = 10$  cm,  $r_2 = 77.4$  cm, and a fixed deviation angle  $\theta = \alpha + \beta = 176^\circ$ . We can vary  $\gamma$  to bring the image at  $\lambda_1$  and  $\lambda_2$  into perfect focus on the detector, and the image at other wavelengths near these into approximate focus. We performed the experiments on silicon foils under this design, using a 480 lines/mm

VLS grating. The exact values of  $\lambda_1$  and  $\lambda_2$  for the spectrometer with this grating are unknown, but presumably they straddle the useful range of the grating from photon energies near 50 eV to above 400 eV. The wavelength range on the detector is set by rotating the grating to a new value of  $\alpha$  (but keeping  $\theta$  constant). The edges of solid silicon (first order  $L_{II,III}$  edges at 99.8 eV) and carbon (second order  $K$  edge at 142.5 eV, third order  $K$  edge at 71 eV) were used to calibrate the spectrum for the pump-probe measurements. For the streak camera experiments on silicon, the visible spectral range was too narrow to see these edges simultaneously, so the energy range of the spectrum was calibrated by varying the grating angle  $\alpha$  and relating this to the movement of the silicon  $L_{II,III}$  edge on the streak camera slit, and by doing the same for the zero-order  $m = 0$  reflection from the grating. This allows us to calculate the relationship between the grating angle setting and the actual incidence angle  $\alpha$  as well as the relationship between the position along the streak camera slit and the grating exit angle  $\beta$ , thus determining the relationship between the position along the slit and the wavelength for a given setting of the grating angle.

We can calculate the resolution of the spectrograph by considering the size of the entrance slit, the resolution of the detector, and the vertical magnification of the spherical mirror and grating. Properly focused, the mirror casts an image at  $r = r_0$ , creating a 1:1 image of the slit. Near the silicon  $L_{II,III}$  edge,  $\alpha = 89.2^\circ$ . The grating magnifies the mirror image by  $r_2 \cos \alpha / (r - r_1) \cos \beta = 0.36$ . The spatial resolution of the detectors used is approximately  $150 \mu\text{m}$ , so the entrance slit width (demagnified

to about  $50 \mu\text{m}$  at the detector) is negligible in comparison. A  $150 \mu\text{m}$  vertical spot size at the detector translates to an angular resolution  $\Delta\beta = 150\mu\text{m}/r_2 = 2 \times 10^{-4} \text{rad}$ .

Differentiating the grating equation C.2 for fixed  $\alpha$  gives

$$\frac{m\Delta\lambda}{d} = \cos(\beta)\Delta\beta, \quad (\text{C.4})$$

making  $\Delta\lambda = 0.6 \text{ \AA}$  and the energy resolution  $hc/\Delta\lambda = 0.8 \text{ eV}$ . This is close to the measured  $1 \text{ eV}$  resolution at the  $L_{\text{II,III}}$  edge. For more details on the resolution and general focusing properties of these types of instruments (especially for  $\lambda$  not equal to the optimized wavelengths  $\lambda_1$  or  $\lambda_2$ ), please see refs. [95] and [70].

The efficiency of the grating reflection for these experiments was approximately 2–4%, lower than typically optimal values of 10–20% primarily due to mechanical defects in the ruling of the grating, but also due to the fact that the deviation angle  $\theta$  is fixed and cannot be optimized for maximum reflection. For the carbon experiments we addressed this problem by modifying the spectrograph to use a Hughes 380 lines/mm constant line-spaced grating with fewer ruling defects and by making the deviation angle  $\theta$  adjustable. For increased throughput, the entrance slits were also moved to within 20 cm of the primary x-ray focus (set at the sample position), allowing more light to enter the spectrograph. For the energy of the carbon  $K$ -edge, measurements of the grating efficiency as a function of deviation angle  $\theta$  indicate that  $\theta = 172^\circ$  is optimal, giving efficiencies of roughly 15%. This can be contrasted with the VLS grating, which gives an efficiency of about 2% in this energy range.

Since this more efficient grating is not a VLS grating, there is less flexibility in

choosing the wavelengths for focusing. The conditions for perfect focusing are met for only one wavelength  $\lambda_0$  at a given setting of  $\gamma$  and  $\alpha$ . In practice, this still provides reasonable focus sizes for a fairly broad range of wavelengths near  $\lambda_0$ , chosen for the carbon experiments to be at the carbon  $K$  edge (285 eV). For the modified instrument, efficiency-optimized focusing of the  $K$ -edge is achieved with  $r_0 = 110$  cm,  $r_1 = 10$  cm,  $\theta = \alpha + \beta = 172^\circ$ , and  $r_2 = 100$  cm, along with appropriate adjustments to the mirror angle  $\gamma$  and grating incidence angle  $\alpha$ . Calibration of the spectrometer was done using the first-order carbon  $K$  edge, the nitrogen  $K$ -edge at 409.9 eV (from a 1000 Å  $\text{Si}_3\text{N}_4$  film), and the titanium  $L_{\text{III}}$  edge at 453.8 eV (from a 1000 Å Ti foil). The vertical magnification of the image of the entrance slit on the detector plane is 1.4, making a slit width of 100  $\mu\text{m}$  both optimal for focusing and big enough to allow nearly all the x-rays to enter the instrument. This leads to an energy resolution of 2 eV, which agrees with estimates based on the actual spectra.

## Appendix D

### Oscillator strength of $\pi^*$ resonances

Let us define the *oscillator strength*  $f$  for an x-ray absorption transition from an initial state  $|i\rangle$  to a bound final state  $|f\rangle$  as

$$f = \frac{2}{mE} |\langle f | \mathbf{e} \cdot \mathbf{p} | i \rangle|^2, \quad (\text{D.1})$$

where (as in section 1.2.2)  $E$  is the photon energy,  $\mathbf{e}$  is a unit vector indicating the x-ray polarization direction, and  $\mathbf{p}$  is the momentum operator. Then we can write equation 1.3 as

$$\sigma_x = \frac{2\pi\hbar^2\alpha}{m} f \rho_f(\epsilon). \quad (\text{D.2})$$

If we now integrate over all final state energies, the density of states  $\rho_f(\epsilon)$  drops out (assuming the state  $|f\rangle$  is normalized to unity), leaving us with an interesting alternative expression for  $f$ :

$$f = \frac{m}{2\pi\hbar^2\alpha} \int \sigma_x dE. \quad (\text{D.3})$$

From this we see that the oscillator strength  $f$  for a transition to a bound state is proportional to the energy integral of the absorption cross section for that transition.

In order to make quantitative statements about the relative numbers of  $\pi^*$  bound states in the various forms of carbon under study in chapter 4, we needed to assume that, when summed over all absorbers in the probed volume,  $f$  is approximately constant for all such states. What follows is a justification of this assumption.

Let  $|\psi\rangle$  be a particular  $\pi^*$  state in an amorphous solid or liquid carbon. Under the LCAO (linear combination of atomic orbitals) scheme, this state can be written as a superposition of the atomic  $|2p\rangle$  orbitals over the different carbon sites [88]:

$$|\psi\rangle = \sum_j \left( a_j |2p_z\rangle_j + b_j |2p_x\rangle_j + c_j |2p_y\rangle_j \right). \quad (\text{D.4})$$

Imposing the normalization condition  $\langle\psi|\psi\rangle^2 = 1$  and assuming no significant overlap between the orbitals of different sites,<sup>1</sup> we obtain

$$\sum_j (|a_j|^2 + |b_j|^2 + |c_j|^2) = 1. \quad (\text{D.5})$$

Since all the materials under study are amorphous, we can also assume that the spatial orientation of the state is not important since it is averaged out by similar states with random orientations. We therefore impose the condition that, for each  $j$ ,  $|a_j|^2 = |b_j|^2 = |c_j|^2$  so we can simplify equation D.5 to

$$\sum_k (|a_k|^2) = 1/3. \quad (\text{D.6})$$

---

<sup>1</sup>This "zero overlap assumption" is reasonably accurate for  $\pi$  bonding. It is used successfully in the perturbative Hückel theory to obtain the splitting of  $\pi$  and  $\pi^*$  orbitals in hydrocarbons [88].

Now consider x-ray absorption from the localized 1s core states within the material to  $|\psi\rangle$ . The oscillator strength  $f_k$  for absorption from a particular site  $k$  is then

$$f_k = \frac{2}{mE} |\langle\psi|\mathbf{e}\cdot\mathbf{p}|1s\rangle_k|^2. \quad (\text{D.7})$$

Using an operator equivalent for the momentum operator

$$\mathbf{p} = \frac{imE}{\hbar} \mathbf{r}, \quad (\text{D.8})$$

we can rewrite  $f_k$  as

$$f_k = \frac{2mE}{\hbar^2} |\mathbf{e}\cdot\langle\psi|\mathbf{r}|1s\rangle_k|^2. \quad (\text{D.9})$$

Let us define the z-axis of the atomic orbitals to be the polarization direction  $\mathbf{e}$  of the x-rays. We can then write

$$f_k = \frac{2mE}{\hbar^2} |\langle\psi|z|1s\rangle_k|^2. \quad (\text{D.10})$$

Since the 1s core state is highly localized, in evaluating the matrix element  $\langle\psi|z|1s\rangle_k$  for a given absorber we can ignore contributions to  $|\psi\rangle$  from the atomic orbitals of other sites. We can then evaluate the matrix element by integrating in position space to obtain

$$\langle\psi|z|1s\rangle_k = \frac{4\pi R}{3} a_k^* \quad (\text{D.11})$$

where  $R = \int_0^\infty R_{1s}(r)R_{2p}(r)r^3dr$ , and the functions  $R_{1s}(r)$  and  $R_{2p}(r)$  are radial components of the atomic wavefunctions [88]. The *total* oscillator strength  $f_{\text{tot}}$  for all possible transitions to  $|\psi\rangle$  is then

$$f_{\text{tot}} = \sum_k f_k = \frac{32mE}{9\hbar^2} |R|^2 \sum_k |a_k|^2 = \frac{32mE}{27\hbar^2} |R|^2, \quad (\text{D.12})$$

where the last step invokes the state normalization condition of equation D.6. Since  $f_{\text{tot}}$  is independent of the coefficients  $a_k$ ,  $b_k$  and  $c_k$  that compose the final state  $|\psi\rangle$ , it is the same for all such states.<sup>2</sup> Each  $\pi^*$  state thus contributes equally to the area under the absorption cross section.

---

<sup>2</sup>After averaging out any directional dependence of such states, of course.

# Appendix E

## Computer scripts and code

The following is a listing of the scripts and code used for controlling the phase-shifter (appendix A) and the slow-feedback oscillator cavity control (described briefly in section 2.2.1). The code is organized into separate files. The “user-level” programs directly used by a person are all BASH shell scripts, ending in “.sh”. The rest of the programs are written in C and compiled using the “makefile” of section E.1.

### E.1 Makefile (for C programs)

This “makefile” controls compilation of the C programs in the rest of this appendix. It has been shown to work well with the GNU version of make, freely available as of the time of this writing at <http://www.gnu.org/software/make/>.

```
# Makefile for the C components of the phaseshifter
# and drift programs
```

CC = gcc

OBJECTS\_RPS = dg.o ps.o serial-ps.o readps.o  
OBJECTS\_SR = dg.o ps.o serial-ps.o shiftrel.o  
OBJECTS\_SPSD = dg.o ps.o serial-ps.o setps-d.o  
OBJECTS\_DRIFT = drift.o serial-ps.o  
OBJECTS\_SPSA = dg.o ps.o serial-ps.o setpsabs.o  
OBJECTS\_SETIQ = ps.o serial-ps.o setiq.o dg.o

all: readps shiftrel setps-d setpsabs setiq drift

clean:

rm \*.o

setps-d: \$(OBJECTS\_SPSD)

\$(CC) -o setps-d \$(OBJECTS\_SPSD) -lgpib -lm -lc

shiftrel: \$(OBJECTS\_SR)

\$(CC) -o shiftrel \$(OBJECTS\_SR) -lgpib -lm -lc

readps: \$(OBJECTS\_RPS)

\$(CC) -o readps \$(OBJECTS\_RPS) -lgpib -lm -lc

setpsabs: \$(OBJECTS\_SPSA)

\$(CC) -o setpsabs \$(OBJECTS\_SPSA) -lgpib -lm -lc

setiq: \$(OBJECTS\_SETIQ)

\$(CC) -o setiq \$(OBJECTS\_SETIQ) -lm -lc -lgpib

drift: \$(OBJECTS\_DRIFT)

\$(CC) -o drift \$(OBJECTS\_DRIFT) -lgpib -lc

setps-d.o: ps\_constants.h ps.h

\$(CC) -c -Wall setps-d.c

shiftrel.o: ps.h dg.h serial-ps.h ps\_constants.h

\$(CC) -c -Wall shiftrel.c

setpsabs.o: ps\_constants.h serial-ps.h dg.h ps.h

\$(CC) -c -Wall setpsabs.c

readps.o: ps.h dg.h serial-ps.h ps\_constants.h



```

# *   readps-wrap.sh                               *
# *   (user-level bash shell script)               *
# *                                               *
# *   Waits for lock files (lock1, lock) to       *
# *   disappear, then reads the status of the     *
# *   I-Q modulator and DG535's using readps     *
# *                                               *
# *****

# Wait for lock file "lock1" from other phaseshifter
# programs to go away
while (test -f /tmp/lock1)
do true
done

# Create lock file for this program
touch /tmp/lock1

# Wait for driftd lock file "lock" to go away
while (test -f /tmp/lock)
do true
done

readps

# We're done, so delete lock file
rm /tmp/lock1

```

## E.2.2 setps-d-wrap.sh

```

#!/bin/sh
# *****
# *                                               *
# *   setps-d-wrap.sh                               *
# *   (user-level bash shell script)               *
# *                                               *
# *   Waits for lock files (lock1, lock) to       *
# *   disappear, then moves the phase via         *
# *   setps-d                                       *
# *                                               *
# *

```

```

# *****

# Wait for lock file "lock1" from other
# phaseshifter programs to go away
while (test -f /tmp/lock1)
do true
done

# Create lock file for this program
touch /tmp/lock1

# Wait for driftd lock file "lock" to go away
while (test -f /tmp/lock)
do true
done

# set the timing, using standard input (see setps-d.c)
setps-d

# We're done, so delete lock file
rm /tmp/lock1

```

### E.2.3 shiftrel-wrap.sh

```

#!/bin/sh
# *****
# *
# *   shiftrel-wrap.sh
# *   (user-level bash shell script)
# *
# *   Waits for lock files (lock1, lock) to
# *   disappear, then reads the status of the
# *   I-Q modulator and DG535's using readps
# *
# *****

# Wait for lock file "lock1" from other
# phaseshifter programs to go away
while (test -f /tmp/lock1)
do true

```

```

done

# Create lock file for this program
touch /tmp/lock1

# Wait for driftd lock file "lock" to go away
while (test -f /tmp/lock)
do true
done

shiftrrel $1

# remove lock file
rm /tmp/lock1

```

## E.2.4 readps.c

```

/*****

```

readps.c

Main source file for constructing the "readps" executable.

### Description:

Polls the DG535's and SRS245 to get the current status of the laser timing delays. Specifically, it returns the phase of the I-Q vector modulator (oscillator phase-shifter), the timing of the Pockel's cells triggers, and the timing of the Q-switch to the Quanta-Ray 10 Hz pump laser.

### Usage:

Simply run the executable.

### Output:

A single line of output, containing the IQ modulator amplitude (i.e.  $\sqrt{I^2+Q^2}$ , after nonlinear corrections), oscillator phase (in ps), Pockel's cell trigger delay (in seconds), and the Quanta-Ray Q-switch trigger delay (in seconds).

```

*****/

#include <stdio.h>
#include "ps.h"
#include "dg.h"
#include "serial-ps.h"
#include "ps_constants.h"

int main()
{
    double psdelay, psamplitude; /* variables for oscillator timing */
    double dgdelay, dg2delay;    /* ...for amplifier timing */
    int fd = open_sr245();        /* open the serial port to the SR245 */
    char buf[200];
    configure_sr245(fd,2);        /* configure I/O of SR245 */

    getpsdelay(fd, ICHANNEL, QCHANNEL, &psdelay, &psamplitude);
    readPCdelay(DG_CONTR, DG_DEV, TIMEOUT, &dgdelay);
    readQSdelay(DG_CONTR, DG2_DEV, TIMEOUT, &dg2delay);

    printf("%f %f %e %e\n", psamplitude, psdelay, dgdelay, dg2delay);
    return 0;
}

```

## E.2.5 setps-d.c

```

/*****

```

setps-d.c

Main source file for generating the "setps-d" executable.

### Description:

The program "setps-d" changes the timing of the laser system with respect to a supplied set of reference timings. All input is from standard input, to facilitate running this program as a

TCP/IP daemon under the "mini-inetd"  
program.

Usage:

Run the program, then enter via standard input a reference I-Q modulator delay (in ps), a reference PC timing (in s), a reference Q-switch timing (in s), and the desired delay (in ns) with respect to the reference timing.

Output:

None

```

*****/

#include "ps_constants.h"
#include "ps.h"
#include <stdlib.h>
#include <stdio.h>

int main(int argc, char** argv)
{
    double junk;
    double refps, refdg, refdg2, delay;

    scanf("%lf %lf %lf %lf",&refps,&refdg,&refdg2,&delay);

    settotaldelay(DG_CONTR,DG_DEV,DG2_DEV,TIMEOUT,
                  ICHANNEL,QCHANNEL,refps,refdg,refdg2,
                  delay/1e9,1,AMPSTEP,DELSTEP,&junk);
    return 0;
}

```

## E.2.6 shiftrel.c

```

/*****

```

```

shiftrel.c

```

Main source file for creating "shiftrel"

**Description:**

Command-line interface program that changes the timing from its current position to some number of ns later (or earlier if given a negative delay).

**Usage:**

shiftrrel <number of ns later>

**Note:**

This program should never be used to do any kind of timing scan. After many steps roundoff errors will foil any semblance of reproducibility.

\*\*\*\*\*/

```

#include <stdio.h>
#include <stdlib.h>
#include <unistd.h>
#include "ps.h"
#include "dg.h"
#include "serial-ps.h"
#include "ps_constants.h"

int main(int argc, char** argv)
{
    double psdelay, psamplitude;
    double dgdelay, dg2delay;
    double reldelay;
    double newpsdelay;

    /* for some odd reason, opening, closing and opening
       the serial port like this eliminates some intermittent
       errors */
    int fd = open_sr245();
    configure_sr245(fd,2);
    close(fd);
    fd = open_sr245();
    configure_sr245(fd,2);

    /* read the current timings */
    getpsdelay(fd, ICHANNEL, QCHANNEL, &psdelay, &psamplitude);

```

```

close(fd);
readPCdelay(DG_CONTR,DG_DEV,TIMEOUT,&dgdelay);
readQSDelay(DG_CONTR,DG2_DEV,TIMEOUT,&dg2delay);

/* if the command line is OK, change the timing */
if (argc==2)
{
    reldelay = atof(argv[1]);
    settotaldelay(DG_CONTR,DG_DEV,DG2_DEV,TIMEOUT,
                  ICHANNEL,QCHANNEL,
                  psdelay,dgdelay,dg2delay, reldelay/1e9,
                  1,AMPSTEP,DELSTEP,&newpsdelay);
}
else
{
    printf("usage:  shiftrel <delay in ns>\n");
    exit(1);
}

close(fd);
return 0;
}

```

## E.2.7 ps\_constants.h

```

/*****

```

```

ps_constants.h

```

```

Header file containg constants of general utility for the
phaseshifter programs

```

```

*****/

```

```

/* Set the I and Q channels of the SR245 */

```

```

#define ICHANNEL 7

```

```

#define QCHANNEL 8

```

```

/* Set the communication parameters of the DG535's */

```

```

#define DG_CONTR 0 /* GPIB card ID */

```

```

#define DG_DEV    10    /* PC switch timing DG535 device ID */
#define DG2_DEV   11    /* Quanta-Ray Q-switch DG535 device ID */
#define TIMEOUT   10    /* GPIB timeout in ms */

/* Step sizes for moving the phase and amplitude of the
   IQ modulator */
#define AMPSTEP   0.01
#define DELSTEP   10

/* define the DG535 output channels used to trigger the
   Pockel's Cells and Quanta-Ray Q-switch.

   T = 1
   A = 2
   B = 3
   C = 4
   D = 5
*/
#define PC_REF_TRIG 1
   /* reference for Pockel's cells trigger */
#define PC_TRIG     2
   /* actual ouptut channel for Pockel's cells trigger */
#define QS_REF_TRIG 1
   /* reference for QR Q-switch trigger */
#define QS_TRIG     2
   /* actual ouptut channel for QR Q-switch trigger */

```

## E.2.8 ps.h

```

/*****

```

```

ps.h

```

```

Header file for functions related to programming the
phase shifter

```

```

*****/

```

```

int settotaldelay(int dg_controllerid, int dg_deviceid,
                  int dg2_deviceid, int timeout,
                  int ichannel, int qchannel,
                  double ref_psdelay, double ref_dgdelay,
                  double ref_dg2delay,
                  double target_totdelay,
                  double target_psamplitude,
                  double amplitude_step, double delay_step,
                  double* new_psdelay);

int shiftsmooth(int fd, int ichannel,
                int qchannel, double target_delay,
                double target_amplitude,
                double amplitude_step, double delay_step );

int getpsdelay(int fd, int ichannel, int qchannel,
               double* delay, double* amplitude);

int setpsdelay(int fd, int ichannel,
               int qchannel, double delay, double amplitude);

int setiq(int fd, float i, float q,
          int ichannel, int qchannel);

int getiq(int fd, int ichannel, int qchannel, float* i,
          float* q);

```

## E.2.9 ps.c

```

/*****

```

```

ps.c

```

Source file for functions related to manipulating the I-Q vector modulator and amplifier timings.

Requires: math libraries (-lm)

```

*****/

```

```

#include <unistd.h>
#include <string.h>
#include <stdio.h>
#include <assert.h>
#include <math.h>
#include "ps.h"
#include "dg.h"
#include "serial-ps.h"

#define PI 3.14159265359

/*****
Changes the delay of the laser s.t. it fires at
"target_totdelay" seconds after the reference delays.
All phaseshifter delays are in picoseconds; all other delays
are in seconds.
*****/
int settotaldelay(int dg_controllerid, int dg_deviceid,
                  int dg2_deviceid, int timeout,
                  int ichannel, int qchannel, double ref_psdelay,
                  double ref_dgdelay, double ref_dg2delay,
                  double target_totdelay,
                  double target_psamplitude,
                  double amplitude_step, double delay_step,
                  double* new_psdelay)
{
    double old_dgdelay;
    double correction_delay;
    double cur_psdelay, cur_psamplitude;
    int fd;

    /* read the PC DG535 to find out its current delay */
    if (readPCdelay(dg_controllerid, dg_deviceid, timeout,
                   &old_dgdelay))
        return -1;
    /* Due to a history of GPIB errors, make sure this timing is
       reasonable.  If not, read until it is OK */
    while (fabs(old_dgdelay - ref_dgdelay)>1e-7)
        readPCdelay(dg_controllerid, dg_deviceid, timeout,
                   &old_dgdelay);
    if (old_dgdelay<1e-6)

```

```

    exit(0);

/* open serial port, initialize sr245 */
fd = open_sr245();
configure_sr245(fd,2);

/* first, move the phase of the oscillator */

/* calculate the "approximate" new I-Q modulator delay */
getpsdelay(fd, ichannel, qchannel,&cur_psdelay,
           &cur_psamplitude);
*new_psdelay = fmod((target_totdelay
                    -(old_dgdelay-ref_dgdelay))*1e12,12000);
if (*new_psdelay < -6000)
    *new_psdelay += 12000;
if (*new_psdelay > 6000)
    *new_psdelay -= 12000;
*new_psdelay += cur_psdelay;

/* now correct for any errors introduced by rounding */
correction_delay = fmod(target_totdelay*1e12
                        -(new_psdelay-ref_psdelay),2000);
if (correction_delay < -1000)
    correction_delay += 2000;
if (correction_delay > 1000)
    correction_delay -= 2000;
*new_psdelay += correction_delay;

/* closing and opening the serial port here seems to
   help sometimes */
close(fd);
fd = open_sr245();
configure_sr245(fd,2);

/* move the I-Q modulator to the new phase! */
if (shiftsmooth(fd, ichannel,
               qchannel,*new_psdelay,
               target_psamplitude,amplitude_step,
               delay_step)==-1)
    return -1;

close(fd);

```

```

/* move the pockel cell timing */
setPCdelay(dg_controllerid,dg_deviceid,timeout,
    target_totdelay+ref_dgdelay);

/* move the Quanta-Ray Q switch timing */
return setQSDelay(dg_controllerid,dg2_deviceid,timeout,
    target_totdelay+ref_dg2delay);

}

/*****
    Changes delay and amplitude of the IQ modulator
    smoothly. Returns 0 if no error, otherwise -1.
*****/
int shiftsmooth(int fd, int ichannel,
    int qchannel, double target_delay,
    double target_amplitude,
    double amplitude_step, double delay_step )
{
    int i,j;
    int a_count;
    int d_count;
    double cur_delay;
    double cur_amplitude;
    int error_flag = 0;

    getpsdelay(fd, ichannel, qchannel, &cur_delay,
        &cur_amplitude);

    /* figure out how many steps we should take */
    a_count = fabs((target_amplitude-cur_amplitude)
        /amplitude_step);
    d_count = fabs((target_delay-cur_delay)/delay_step);
    if (a_count == 0) a_count = 1;
    if (d_count == 0) d_count = 1;

    /* Change amplitude first */
    for (i=0;i<a_count;i++)
        if (setpsdelay(fd, ichannel, qchannel,
            cur_delay, cur_amplitude+(i+1)*
            (target_amplitude-cur_amplitude)

```

```

                /a_count)==0)
    error_flag=-1;

    /* Then (if no errors), change phase */
    if (error_flag == 0)
        for (j=0;j<d_count;j++)
            if (setpsdelay(fd, ichannel, qchannel,
                cur_delay+(j+1)
                    *(target_delay-cur_delay)/d_count,
                target_amplitude)==0)
    error_flag=-1;

    return error_flag;
}

/*****
    Set the delay of the I-Q modulator instantaneously.
    Delay is in picoseconds.
*****/
int setpsdelay(int fd, int ichannel,
               int qchannel, double delay, double amplitude)
{
    return setiq(fd,
                amplitude*cos(delay*2*PI/2000),
                amplitude*sin(delay*2*PI/2000),
                ichannel, qchannel);
}

/*****
    Read the delay of the I-Q modulator, in ps.
*****/
int getpsdelay(int fd, int ichannel, int qchannel,
               double* delay, double* amplitude)
{
    float i,q;
    int toret;

    toret = getiq(fd, ichannel, qchannel,&i,&q);
    if (fabs(i) < 1e-3)
        if (q>0) *delay = 500;
        else *delay = -500;
}

```

```

else
    *delay = atan(q/i)*1000/PI;
if ((i<0)&&(q>0))
    *delay = *delay+1000;
if ((i<0)&&(q<0))
    *delay = *delay-1000;

*amplitude = sqrt(i*i+q*q);

return toret;
}

/*****
Read values of I and Q for the I-Q modulator, correcting
them according to calibration measurements.
*****/
int getiq(int fd, int ichannel, int qchannel, float* i,
          float* q)
{
    float rawi,rawq;
    rawi = readvoltage_sr245(fd,ichannel);
    rawq = readvoltage_sr245(fd,qchannel);
    *i = (-2.353+80.82*rawi-3.23*rawi*rawi
          +5.33*rawi*rawi*rawi)/88.8;
    *q = (-2.15+79.835*rawq-1.03169*rawq*rawq
          +6.19529*rawq*rawq*rawq)/88.8;
    return 1;
}

/*****
Set values of I and Q for the I-Q modulator, correcting them
according to calibration measurements.
*****/
int setiq(int fd, float i, float q,
          int ichannel, int qchannel)
{
    float iout,qout;
    setvoltage_sr245(fd,ichannel,
                     iout=(0.03094+0.01232*(i*88.8)
                           +3.47203e-6*(i*i*88.8*88.8)
                           -8.74979e-8*(i*i*i*88.8*88.8*88.8)));
    setvoltage_sr245(fd,qchannel,

```

```

        qout=(0.02731+0.01243*(q*88.8)
              +6.35859e-7*(q*q*88.8*88.8)
              -1.04181e-7*(q*q*q*88.8*88.8*88.8));
    return 1;
}

```

## E.2.10 dg.h

```

/*****

```

```

dg.h

```

Header file for functions related to setting the amplifier timing via the DG535's.

```

*****/

```

```

int setPCdelay(int controllerid, int deviceid, int timeout,
               double delay);
int setQSDelay(int controllerid, int deviceid, int timeout,
               double delay);
int readPCdelay(int controllerid, int deviceid, int timeout,
                double* pdelay);
int readQSDelay(int controllerid, int deviceid, int timeout,
                double* pdelay);

int sendgpib_dg(int ud, int controllerid, int deviceid,
                int timeout, char* command);
int readgpib_dg(int ud, int controllerid, int deviceid,
                int timeout, char* buffer, int bufferlen);

int setdelay_dg(int controllerid, int deviceid, int timeout,
                double delay, int reftrigchannel,
                int trigchannel);
int readdelay_dg(int controllerid, int deviceid,
                 int timeout, double* pdelay,
                 int trigchannel);

```

## E.2.11 dg.c

```

/*****

```

```

dg.c

```

```

Source file for using the DG535 via GPIB

```

```

*****/

```

```

#include <stdio.h>
#include <string.h>
#include <assert.h>
#include "dg.h"
#include <sys/ugpib.h>
#include "ps_constants.h"

```

```

#define EOS_CODE 7178 /* send eoi with eos char;
                       eos char = LF */
#define BUFLLEN 100 /* length of string buffers */

```

```

/*****

```

```

    Sets the delay of the Pockel's cells.

```

```

*****/

```

```

int setPCdelay(int controllerid, int deviceid, int timeout,
               double delay)

```

```

{
    return setdelay_dg(controllerid,deviceid,timeout,delay,
                       PC_REF_TRIG,PC_TRIG);
}

```

```

/*****

```

```

    Sets the delay of the QR Q-switch.

```

```

*****/

```

```

int setQSDelay(int controllerid, int deviceid, int timeout,
               double delay)

```

```

{

```

```

return setdelay_dg(controllerid,deviceid,timeout,delay,
                    QS_REF_TRIG,QS_TRIG);
}

/*****
set the delay of a DG535 (delay in seconds)
*****/
int setdelay_dg(int controllerid, int deviceid, int timeout,
                double delay, int reftrigchannel,
                int trigchannel)
{
    char command[BUFLEN],rdbuffer[BUFLEN];
    int ud;

    /* Create the command string to send */
    sprintf(command,"DT %i,%i,%E\n",trigchannel,
            reftrigchannel,delay);

    /* Open the device interface */
    ud = ibdev(controllerid, deviceid, deviceid, timeout,
                1, EOS_CODE);
    ibsic(ud);

    /* Send the command */
    sendgpib_dg(ud,controllerid,deviceid,timeout,command);

    while (ibsta != 256) /* if there is an error, resend
                        until it is clear */
    {
        ibonl(ud,0);
        ud = ibdev(controllerid, deviceid, deviceid, timeout,
                    1, EOS_CODE);
        ibsic(ud);
        sendgpib_dg(ud,controllerid,deviceid,timeout,"ES");
        readgpib_dg(ud,controllerid,deviceid,timeout,rdbuffer,
                    BUFLEN);
        sendgpib_dg(ud,controllerid,deviceid,timeout,command);
    }
    ibonl(ud,0);
    return 0;
}

```

```

/*****
  send a gpib command
*****/
int sendgpib_dg(int ud, int controllerid, int deviceid,
                int timeout, char* command)
{
  int toret;
  toret = ibwrt(ud,command,strlen(command));
  return toret;
}

/*****
  read a response over gpib
*****/
int readgpib_dg(int ud, int controllerid, int deviceid,
                int timeout, char* buffer, int bufferlen)
{
  int toret;
  toret = ibrd(ud, buffer, bufferlen);
  return toret;
}

/*****
  Read the current delay of the Pockel's cells.
*****/
int readPCdelay(int controllerid, int deviceid,
                int timeout, double* pdelay)
{
  return readdelay_dg(controllerid,deviceid,timeout,pdelay,
                      PC_TRIG);
}

/*****
  Read the current delay of the QR Q-switch.
*****/
int readQSdelay(int controllerid, int deviceid, int timeout,
                double* pdelay)
{
  return readdelay_dg(controllerid,deviceid,timeout,
                      pdelay,QS_TRIG);
}

```

```

}

/*****
Read the current delay of a DG535 (in seconds)
*****/
int readdelay_dg(int controllerid, int deviceid, int timeout,
double* pdelay, int trigchannel)
{
char buffer[BUFLEN] = "hello";
char buffer2[BUFLEN] = "";
char rdbuffer[BUFLEN] = "hey";

int ud;

/* prepare device for communication */
ud = ibdev(controllerid, deviceid, deviceid, timeout, 1,
EOS_CODE);
ibsic(ud);
sendgpib_dg(ud,controllerid,deviceid,timeout,"GT 13,10");

/* send the command to request the delay */
sprintf(buffer, "DT%i\n", trigchannel);
sendgpib_dg(ud,controllerid,deviceid,timeout,buffer);

/* read the response */
if (ibsta == 256) readgpib_dg(ud,controllerid, deviceid,
timeout, rdbuffer, BUFLEN);
while ((ibsta!=8448)) /* try again if there were errors */
{
strcpy(buffer2,rdbuffer);
ibonl(ud,0);
ud = ibdev(controllerid, deviceid, deviceid,
timeout, 1, EOS_CODE);
ibsic(ud);
sendgpib_dg(ud,controllerid,deviceid,timeout,"ES");
readgpib_dg(ud,controllerid,deviceid,timeout,
rdbuffer,BUFLEN);
sendgpib_dg(ud,controllerid,deviceid,timeout,
buffer);
if (ibsta == 256)
readgpib_dg(ud,controllerid, deviceid, timeout,
rdbuffer, BUFLEN);
}
}

```

```

    }

    /* Parse the return string */
    sscanf(rdbuffer+3, "%lf", pdelay);

    ibonl(ud,0);
    return 0;
}

```

### E.2.12 serial-ps.h

```

/*****

serial-ps.h

Header file for functions that control the serial interface to the
SR245

*****/

int open_sr245();
float readvoltage_sr245(int fd, int channel);
void setvoltage_sr245(int fd, int channel, float voltage);
void configure_sr245(int fd, int inchannels);

```

### E.2.13 serial-ps.c

```

/*****

serial-ps.c

Source file for functions that use the serial interface to
talk to the SR245 DAQ for using the I-Q modulator and/or
the slow-feedback for the oscillator phase lock.

*****/

#include <termios.h>
#include <stdio.h>

```

```

#include <unistd.h>
#include <fcntl.h>
#include <sys/signal.h>
#include <string.h>
#include "serial-ps.h"

#define BAUDRATE B9600
#define SR245DEVICE "/dev/ttyS0"
#define MAXCHARS 100

/*****
  Opens the serial port for read/write, *not* as controlling
  TY does high-level configure, too
*****/
int open_sr245()
{
    struct termios newtio;

    int fd = open(SR245DEVICE,O_RDWR | O_NOCTTY );
    if (fd<0) {perror(SR245DEVICE);exit(-1);}

    newtio.c_cflag = BAUDRATE | CRTSCTS | CS8 | CLOCAL | CREAD;
    newtio.c_iflag = IGNPAR | ICRNL;
    newtio.c_oflag = 0;
    newtio.c_lflag = ICANON;
    newtio.c_cc[VMIN]=1;
    newtio.c_cc[VTIME]=0;
    tcflush(fd, TCIFLUSH);
    tcsetattr(fd,TCSANOW,&newtio);
    return fd;
}

/*****
  Reads a voltage pin on the SR245
*****/
float readvoltage_sr245(int fd, int channel)
{
    char buffer[MAXCHARS+1];
    float toret;

    /* send a request for the pin voltage */
    sprintf(buffer, "?%i\r", channel);

```

```

write(fd,buffer,3);

/* read the response */
read(fd,buffer,MAXCHARS);
sscanf(buffer, "%f", &toret);
return toret;
}

/*****
Sets a pin voltage on the SR245
*****/
void setvoltage_sr245(int fd, int channel, float voltage)
{
char buffer[MAXCHARS+1];
sprintf(buffer, "s%i=%f\r", channel, voltage);
write(fd,buffer,strlen(buffer));
}

/*****
Configures the SR245 to decide which pins are inputs and
which are outputs
*****/
void configure_sr245(int fd, int inchannels)
{
char buffer[MAXCHARS+1];

/* Make the first <inchannels> pins inputs.
The rest are outputs. */
sprintf(buffer, "W0;I%i\r", inchannels);
write(fd,buffer,strlen(buffer));
}

```

## E.2.14 setpsabs.c

```

/*****

```

```

setpsabs.c

```

```

Main source file to make "setpsabs"

```

**Description:**

Sets the I-Q modulator ALONE to a particular phase (non-smoothly)

**Usage:**

setpsabs <phase (ps)>

\*\*\*\*\*/

```
#include <stdio.h>
#include <stdlib.h>
#include "ps.h"
#include "dg.h"
#include "serial-ps.h"
#include "ps_constants.h"

int main(int argc, char** argv)
{
    double reldelay;
    int fd = open_sr245();
    configure_sr245(fd,2);

    if (argc==2)
    {
        reldelay = atof(argv[1]);
        setpsdelay(fd, ICHANNEL, QCHANNEL, reldelay, 1);
    }
    else
    {
        printf("usage:  shiftrel <delay in ps>\n");
        exit(1);
    }
    return 0;
}
```

**E.2.15 setiq.c**

/\*\*\*\*\*

setiq.c

Main source file to create "setiq" executable

Description:

Allows explicit setting of I and Q voltages to the IQ modulator

Usage:

setiq <i> <q>

\*\*\*\*\*/

```
#include "ps.h"
#include <stdlib.h>
#include <stdio.h>
#include "serial-ps.h"
#include "ps_constants.h"

int main(int argc, char** argv)
{
    int fd;

    if (argc != 3)
    {
        printf("usage: setiq <i> <q> \n");
        exit(1);
    }

    fd = open_sr245();
    configure_sr245(fd,2);
    setiq(fd,atof(argv[1]),atof(argv[2]),ICHANNEL,QCHANNEL);
    return 0;
}
```

## E.3 Slow-feedback control scripts and code

To enable the slow-feedback checking and correction of the oscillator cavity, simply run `driftd.sh`. In practice, this is done automatically by the computer upon startup.

Note that compiling “`drift.c`” requires several files from the phaseshifter code, since it uses some of the same functions for interfacing with the SR245 and the GPIB card.

### E.3.1 `driftd.sh`

```
#!/bin/bash

# *****
# *                                     *
# *   driftd.sh                         *
# *                                     *
# *   Runds driftcheck.sh continuously  *
# *                                     *
# *****

while (true)
do
    driftcheck.sh
done
```

### E.3.2 `driftcheck.sh`

```
#!/bin/bash
# *****
# *                                     *
# *   driftcheck.sh                     *
# *                                     *
# *   Checks for phaseshifter lock file (lock1) *
# *   If not there, then checks & corrects  *
# *   oscillator cavity length           *
# *****
```

```

# *
# *****

# Create lock file
touch /tmp/lock

# Abort if phaseshifter lock file seen
if [ -f /tmp/lock1 ]
then
  rm /tmp/lock
  sleep 1
  exit 0
fi

# Otherwise, perform check & correction
drift

# Remove lock file
rm /tmp/lock

# Wait a little bit so we don't do this too
# frequently, tying up the hardware .
sleep 1

```

### E.3.3 drift.c

```

/*****

```

drift.c

Main source file to generate "drift", a program to check and correct the oscillator cavity length on a slow time scale

Usage:

Just run the program

Output:

Sends a diagnostic string to std output, indicating

the voltage read and action taken.

```

*****/

#include "serial-ps.h"
#include <sys/ugpib.h>
#include <stdio.h>
#include <stdlib.h>

#define INCHANNEL 1 /* Input channel for sr245. The HV
                    monitor from the PLL interface box
                    should come into this channel. */

/* Set "allowed" voltage range for INCHANNEL */
#define TOOHIGH 1.1
#define TOLOW 0.61
#define WAYTOLOW 0.4 /* If INCHANNEL's voltage is below
                     WAYTOLOW, the program assumes
                     phase lock is completely lost
                     and will doo nothing */

#define EOS_CODE 7178
#define BUFFLEN 100

/* Parameters for Picomotor Driver control over GPIB */
#define CONTROLID 0 /* GPIB card ID */
#define DEVID 3 /* Device ID */
#define TIMEOUT 10 /* GPIB timeout in ms */

/* Various commands we might want to send to the
   Picomotor Driver */
#define SELCOM ":INST:NSEL 112"
    /* Selects the right picomotor */
#define INDIRCOM ":SOUR:DIR IN"
    /* Picks the "IN" direction of motion */
#define OUTDIRCOM ":SOUR:DIR OUT"
    /* Picks the "OUT" direction of motion */
#define PULSECOM ":SOUR:PULS:COUN 1"
    /* Send one pulse */

```

```
int main(int argc, char** argv)
{
float voltage;
int fd;      /* file handler for sr245 */
int direction;

/* read voltage */
fd = open_sr245();
configure_sr245(fd,2);
voltage = readvoltage_sr245(fd, INCHANNEL);

/* decide on direction */
direction = 0;
if (voltage > TOOHIGH) direction = 1;
if (voltage < TOLOW) direction = -1;
if (voltage < WAYTOLOW) direction = 0;

/* Send diagnostic string */
printf("%f\t%i\n",voltage,direction);

/* move pico */
if (direction != 0)
{
int ud;
ud = ibdev(CONTROLID, DEVID, DEVID, TIMEOUT, 1, EOS_CODE);
ibwrt(ud,SELCOM,strlen(SELCOM));
if (direction == -1) ibwrt(ud, INDIRCOM, strlen(INDIRCOM));
if (direction == 1) ibwrt(ud, OUTDIRCOM, strlen(OUTDIRCOM));
ibwrt(ud, PULSECOM, strlen(PULSECOM));
ibonl(ud,0);
}

return 0;

}
```

## Bibliography

- [1] M. Alterelli and D. L. Dexter. Core excitons and the soft-X-ray threshold of silicon. *Phys. Rev. Lett.*, 29:1100, 1972.
- [2] S. Anders, A. Anders, I. G. Brown, B. Wei, K. Komvopoulos, J. W. Ager III, and K. M. Yu. Effect of vacuum arc deposition parameters on the properties of amorphous-carbon thin-films. *Surf. Coat. Technol.*, 68/69:388, 1994.
- [3] S. I. Anisimov, N. A. Inogamov, A. M. Oparin, B. Rethfeld, T. Yabe, M. Ogawa, and V. E. Fortov. Pulsed laser evaporation: Equation-of-state effects. *Appl. Phys. A*, 69:617–620, 1999.
- [4] A. L. Ankudinov, B. Ravel, J. J. Rehr, and S. D. Conradson. Real-space multiple-scattering calculation and interpretation of X-ray-absorption near-edge structure. *Phys. Rev. B*, 58:7565, 1998.
- [5] A. L. Ankudinov and J. J. Rehr. Theory of solid-state contributions to the X-ray elastic scattering amplitude. *Phys. Rev. B*, 62:2437–45, 2000.

- [6] A. Assion, T. Baumert, M. Bergt, T. Brixner, B. Kiefer, V. Seyfried, M. Strehle, and G. Gerber. Control of chemical reactions by feedback-optimized phase-shaped femtosecond laser pulses. *Science*, 282:919–922, 1998.
- [7] G. T. Barkema and Normand Mousseau. High-quality continuous random networks. *Phys. Rev. Lett.*, 62:4985–4990, 2000.
- [8] P. E. Batson. Distortion of the core exciton by the swift electron and plasmon wake in spatially resolved electron-energy-loss scattering. *Phys. Rev. B*, 47:6898–10, 1993.
- [9] P. E. Batson. Near edge conduction band electronic states in sige alloys. *J. Electron. Microsc.*, 49:267–73, 2000.
- [10] A. Bianconi. Multiplet splitting of final-state configurations in x-ray-absorption spectrum of metal  $\text{VO}_2$ : Effect of core-hole-screening, electron correlation, and metal-insulator transition. *Phys. Rev. B*, 26:2741–2747, 1989.
- [11] C. Bressler, M. Saes, P. A. Heimann, R. Abela, D. Grolimund, S. L. Johnson, and M. Chergui. Observing transient chemical changes by ultrafast X-ray absorption spectroscopy. Submitted.
- [12] S. D. Brorson, A. Kazeroonian, J. S. Moodera, D. W. Face, T. K. Cheng, E. P. Ippen, M. S. Dresselhaus, , and G. Dresselhaus. Femtosecond room-

- temperature measurement of the electron-phonon coupling constant  $\gamma$  in metallic superconductors. *Phys. Rev. Lett.*, 64:2172–2175, 1990.
- [13] Fredrick C. Brown, R. Z. Bachrach, and M. Skibowski.  $L_{2,3}$  threshold spectra of doped silicon and silicon compounds. *Phys. Rev. B*, 15:4781–4788, 1977.
- [14] Fredrick C. Brown and Om P. Rustigi. Extreme ultraviolet transmission of crystalline and amorphous silicon. *Phys. Rev. Lett.*, 28:497–500, 1972.
- [15] R. Buczko, G. Duscher, S. J. Pennycook, and S. T. Pantelides. Excitonic effects in core-excitation spectra of semiconductors. *Phys. Rev. Lett.*, 85:2168–2171, 2000.
- [16] F. P. Bundy. Direct conversion of graphite to diamond in static pressure apparatus. *J. Chem. Phys.*, 38:618, 1963.
- [17] F. P. Bundy, W. A. Bassett, M. S. Weathers, R. J. Hemley, H. K. Mao, and A. F. Goncharov. The pressure-temperature phase and transformation diagram for carbon; updated through 1994. *Carbon*, 34:141–53, 1995.
- [18] J. Byrd. Personal communication.
- [19] L. Campbell, L. Hedin, J. J. Rehr, and W. Bardyszewski. Interference between extrinsic and intrinsic losses in X-ray absorption fine structure. *Phys. Rev. B*, 65:064107/1–13, 2002.

- [20] A. Cavalleri, C. W. Siders, F. L. H. Brown, D. M. Leitner, C. Tóth, J. A. Squier, C. P. J. Barty, and K. R. Wilson. Anharmonic lattice dynamics in germanium measured with ultrafast X-ray diffraction. *Phys. Rev. Lett.*, 82:586–589, 2000.
- [21] A. Cavalleri, K. Sokolowski-Tinten, C. von der Linde, I. Spagnolatti, M. Bernasconi, G. Benedek, A. Podestá, and P. Milani. Generation of the low-density liquid phase of carbon by non-thermal melting of fullerite. *Europhys. Lett.*, 57:281–87, 2002.
- [22] A. Cavalleri, C. Toth, C. W. Siders, J. A. Squier, F. Raksi, P. Forget, and J. C. Kieffer. Femtosecond structural dynamics in VO<sub>2</sub> during an ultrafast solid-solid phase transition. *Phys. Rev. Lett.*, 87:237401/1–4, 2001.
- [23] Z. Chang, A. Rundquist, J. Zhou, M. M. Murnane, H. C. Kapteyn, X. Liu, B. Shan, J. Liu, L. Niu, M. Gong, and X. Zhang. Demonstration of a sub-picosecond x-ray streak camera. *Appl. Phys. Lett.*, 69:133–135, 1996.
- [24] L. X. Chen, W. J. H. Jäger, G. Jennings, and D. J. Gosztola. Capturing a photoexcited molecular structure through time-domain X-ray absorption fine structure. *Science*, 292:262–4, 2001.
- [25] A. H. Chin, R. W. Schoenlein, T. E. Glover TE, P. Balling, W. P. Leemans, and C. V. Shank. Ultrafast structural dynamics in InSb probed by time-resolved X-ray diffraction. *Phys. Rev. Lett.*, 83:336–9, 1999.

- [26] J. Díaz, S. Anders, X. Zhou, E. J. Moler, S. A. Kellar, and Z. Hussain. Analysis of the  $\pi^*$  and  $\sigma^*$  bands of the x-ray absorption spectrum of amorphous carbon. *Phys. Rev. B*, pages 125204/1–19, 2001.
- [27] F. E. Doany and D. Grischkowsky. Measurement of ultrafast hot-carrier relaxation in silicon by thin-film-enhanced, time-resolved reflectivity. *Appl. Phys. Lett.*, 52:36–38, 1988.
- [28] M. C. Downer and C. V. Shank. Ultrafast heating of silicon on sapphire by femtosecond optical pulses. *Phys. Rev. Lett.*, 56:761–764, 1986.
- [29] A. Erbil, G. S. Cargill III, R. Frahm, and R. F. Boehme. Total-electron-yield current measurements for near-surface extended x-ray-absorption fine structure. *Phys. Rev. B*, 37:2450–64, 1988.
- [30] N. S. Fateeva and L. F. Vereshchagin. Concerning the melting point of graphite up to 90 kbar. *JETP Lett.*, 13:110–1, 1971.
- [31] M. Fiebig, K. Miyano, Y. Tomioka, and Y. Tokura. Sub-picosecond photo-induced melting of a charge-ordered state in a perovskite manganite. *Appl. Phys. B*, 71:211–215, 2000.
- [32] J. P. Gabathuler and S. Steeb. Structure of Si-, Ge-, Sn-, and Pb-melts. *Z. Naturforsch A*, 34:1314, 1979.

- [33] G. R. Gathers, J. W. Shaner, and D. A. Young. Experimental, very high-temperature, liquid-uranium equation of state. *Phys. Rev. Lett.*, 33:70–72, 1974.
- [34] H. C. Gerritsen, H. van Brug, F. Bijkerk, K. Murakami, and M. J. van der Wiel. A time-resolved X-ray absorption study of amorphous Si during pulsed laser irradiation. *J. Appl. Phys.*, 60:1774–83, 1986.
- [35] James N. Glosli and Francis H. Ree. Liquid-liquid phase transformation in carbon. *Phys. Rev. Lett.*, 82:4659–62, 1999.
- [36] E. Gullikson. CXRO's home page. <http://www.cxro-lbl.gov>, 2002. WWW-based program to calculate X-ray reflection, transmission, and bend magnet radiation properties. Based partly on data of ref. [37].
- [37] B.L. Henke, E.M. Gullikson, and J.C. Davis. X-ray interactions: photoabsorption, scattering, transmission, and reflection at  $e=50\text{--}30000$  ev,  $z=1\text{--}92$ . *Atomic Data and Nuclear Data Tables*, 54:181–342, 1993.
- [38] J. Heremans, C. H. Olk, G. L. Ecsly, J. Steinbeck, and G. Dresselhaus. Observation of metallic conductivity in liquid carbon. *Phys. Rev. Lett.*, 60:452–455, 1988.
- [39] J. Herrmann. Theory of Kerr-lens mode locking: role of self-focusing and radially varying gain. *J. Opt. Soc. Amer. B*, 11:498–512, 1994.

- [40] D. Horowitz and W. Hill. *The Art of Electronics*. Cambridge University Press, 2nd edition, 1989.
- [41] S. Ichimaru. Nuclear fusion in dense plasmas. *Rev. Mod. Phys.*, 65:255–299, 1993.
- [42] W. Jank and J. Hafner. Structural and electronic properties of the liquid polyvalent elements: The group-IV elements Si, Ge, Sn, and Pb. *Phys. Rev. B*, 41:1497–1515, 1990.
- [43] H. O. Jeschke, M. E. Garcia, and K. H. Bennemann. Microscopic analysis of the laser-induced femtosecond graphitization of diamond. *Phys. Rev. B*, 60:R3701–4, 1999.
- [44] H. O. Jeschke, M. E. Garcia, and K. H. Bennemann. Theory for laser-induced ultrafast phase transitions in carbon. *Appl. Phys. A*, 69:S49–53, 1999.
- [45] H. O. Jeschke, M. E. Garcia, and K. H. Bennemann. Theory for the ultrafast ablation of graphite films. *Phys. Rev. Lett.*, 87:15003, 2001.
- [46] M. T. Jones. *Nat. Carbon Res Lab. Report PRG*.
- [47] K.-J. Kim. Characteristics of synchrotron radiation. In *Physics of Particle Accelerators*, volume 184 of *AIP Conf. Proc.*, page 565. Am. Inst. Phys., New York, 1989.

- [48] Khalid Laaziri, S. Kycia, S. Roorda, M. Chicoine, J. L. Robertson, J. Wang, and S. C. Moss. High-energy x-ray diffraction study of pure amorphous silicon. *Phys. Rev. B*, 60:13520–33, 1999.
- [49] S. D. Lambade, G. G. Sahasrabudhe, and S. Rajagopalan. Temperature variation of ultrasonic attenuation and nonlinearity parameter in lif and naf. *J. Appl. Phys.*, 78:6525–33, 1995.
- [50] B. C. Larson, C. W. White, T. S. Noggle, J. F. Barhorst, and D. M. Mills. Time-resolved x-ray diffraction measurement of the temperature and temperature gradients in silicon during pulsed laser annealing. *Appl. Phys. Lett.*, 42:282–4, 1983.
- [51] J. Larsson, A. Allen, P. H. Bucksbaum, R. W. Falcone, A. Lindenberg, G. Naylor, T. Missalla, D. A. Reis, K. Scheidt, A. Sjogren, P. Sondhauss, M. Wulff, and J. S. Wark. Picosecond X-ray diffraction studies of laser-excited acoustic phonons in InSb. *Appl. Phys. A*, A75:467–78, 2002.
- [52] A. M. Lindenberg. *Ultrafast Lattice Dynamics in Solids Probed by Time-resolved X-ray Diffraction*. PhD thesis, University of California at Berkeley, 2001. Section 2.4.1.
- [53] A. M. Lindenberg, I. Kang, S. L. Johnson, T. Missalla, P. A. Heimann, Z. Chang, J. Larsson, P. H. Bucksbaum, H. C. Kapteyn, H. A. Padmore, R. W. Lee, J. W. Wark, and R. W. Falcone. Time-resolved X-ray diffraction from

- coherent phonons during a laser-induced phase transition. *Phys. Rev. Lett.*, 84:111–114, 2000.
- [54] C. S. Liu, Z. G. Zhu, Junchao Xia, and D. Y. Sun. Molecular dynamics simulation of the local inherent structure of liquid silicon at different temperatures. *Phys. Rev. B*, 60:3194–3199, 1999.
- [55] A. Ludwig. Die Schmelzung der Kohle. *Zeit. Elektrochem.*, 8:273, 1902.
- [56] M. M. Martynyuk. Resistance and enthalpy of refractory exploding wires. *Sov. Phys. Tech. Phys.*, 19:793–797, 1974.
- [57] A. Miotello and R. Kelly. Laser-induced phase explosion: new physical problems when a condensed phase approaches the thermodynamic critical temperature. *Appl. Phys. A*, 69:S67–S73, 1999.
- [58] J. R. Morris, C. Z. Wang, and K. M. Ho. Relationship between structure and conductivity in liquid carbon. *Phys. Rev. B*, 52:4138–45, 1995.
- [59] K. Murakami and K. Masuda. *Semiconductors Probed by Ultrafast Laser Spectroscopy*, volume II, pages 171–95. Academic, New York, 1984.
- [60] Kouichi Murakami, Hans C. Gerritsen, Heder van Brug, Fred Bijkerk, Frans W. Saris, and Marnix J. van der Wiel. Pulsed-laser irradiated silicon studied by time-resolved X-ray absorption (90–300 eV). *Phys. Rev. Lett.*, 56:655–658, 1986.

- [61] H. Nakano, Y. Goto, P. Lu, T. Nishikawa, and N. Uesugi. Time-resolved soft X-ray absorption spectroscopy of silicon using femtosecond laser plasma X-rays. *Appl. Phys. Lett.*, 75:2350–2, 1999.
- [62] A. I. Nesvizhskii and J. J. Rehr. L-edge xanes of 3d-transition metals. *J. Synchrotron Radiat.*, 6:696, 1999.
- [63] R. Neutze, R. Wouts, S. Techert, J. Davidsson, M. Kocsis, A. Kirrander, F. Schotte, and M. Wulff. Visualizing photochemical dynamics in solution through picosecond X-ray scattering. *Phys. Rev. Lett.*, 87:109–12, 2001.
- [64] R. Neutze, R. Wouts, D. van der Spoel, E. Weckert, and J. Hajdu. Potential for biomolecular imaging with femtosecond X-ray pulses. *Nature*, 406:752–7, 2000.
- [65] New Focus, Inc., Santa Clara, CA. *Model 8732 User's Manual: The Picomotor Driver*.
- [66] L. Nugent-Glandorf, M. Scheer, D. A. Samuels, V. Bierbaum, and S. R. Leone. A laser-based instrument for the study of ultrafast chemical dynamics by soft X-ray-probe photoelectron spectroscopy. *Rev. Sci. Instrum.*, 73:1875–86, 2002.
- [67] L. Nugent-Glandorf, M. Scheer, D. A. Samuels, A. M. Mulhisen, E. R. Grant, Xueming Yang, V. M. Bierbaum, and S. R. Leone. Ultrafast time-resolved soft X-ray photoelectron spectroscopy of dissociating Br<sub>2</sub>. *Phys. Rev. Lett.*, 87:33–6, 2001.

- [68] D. A. Outka and J. Stöhr. Curve fitting analysis of near-edge core excitation spectra of free, adsorbed, and polymeric molecules. *J. Chem. Phys.*, pages 3539–54, 1988.
- [69] H. Petersen. The plane grating and elliptical mirror: a new optical configuration for monochromators. *Opt. Commun.*, 40:402, 1982.
- [70] H. Petersen, C. Jung, C. Hellwig, W. B. Peatman, and W. Gudat. Review of plane grating focusing for soft x-ray monochromators. *Rev. Sci. Instrum.*, 66:1–13Z, 1995.
- [71] V. Petkov, S. Takeda, Y. Waseda, and K. Sugiyama. Structural study of molten germanium by energy-dispersive X-ray diffraction. *J. Non-Cryst. Solids*, 168:97–105, 1994.
- [72] F. Raksi, K. R. Wilson, Zhimig Jiang, A. Ikhlef, C. Y. Cote, and J-C. Kieffer. Ultrafast X-ray absorption probing of a chemical reaction. *J. Chem. Phys.*, 104:6066–9, 1996.
- [73] J. J. Rehr and R. C. Albers. Theoretical approaches to X-ray absorption fine structure. *Rev. Mod. Phys.*, 72:621–654, 2000.
- [74] D. A. Reis, M. F. DeCamp, P. H. Bucksbaum, R. Clarke, E. Dufresne, M. Hertlein, R. Merlin, R. Falcone, and H. Kapteyn. Probing impulsive strain propagation with X-ray pulses. *Phys. Rev. Lett.*, 86:3072, 2001.

- [75] D. H. Reitze, H. Ahn, and M. C. Downer. Optical properties of liquid carbon measured by femtosecond spectroscopy. *Phys. Rev. B*, 45:2677–93, 1992.
- [76] C. Rose-Petruck, R. Jimenez, T. Guo, A. Cavalleri, C. W. Siders, F. Raksi, J. A. Squier, B. C. Walker, K. R. Wilson, and C. P. J. Barty. Picosecond-milliangstrom lattice dynamics measured by ultrafast X-ray diffraction. *Nature*, 398:310–12, 1999.
- [77] M. Ross. The ice layer in Uranus and Neptune-diamonds in the sky? *Nature*, 292:435–6, 1981.
- [78] A. Rousse, C. Rischel, S. Fourmaux, I. Uschmann, S. Sebban, G. Grillon, Ph. Balcou, E. Forster, J. P. Geindre, P. Audebert, J. C. Gauthier, and D. Hulin. Non-thermal melting in semiconductors measured at femtosecond resolution. *Nature*, 410:65–8, 2001.
- [79] P. S. Salmon. A neutron diffraction study on the structure of liquid germanium. *J. Phys. F*, 18:2345, 1988.
- [80] K. Seibert, G. C. Cho, W. Kütt, H. Kurz, D. H. Reitze, J. I. Dadap, H. Ahn, M. C. Downer, and A. M. Malvezzi. Femtosecond carrier dynamics in graphite. *Phys. Rev. B*, 42:2842, 1990.
- [81] I. L. Shumay and U. Hofer. Phase transformations of an InSb surface induced by strong femtosecond laser pulses. *Phys. Rev. B*, 53:15878–84, 1996.

- [82] P. L. Silvestrelli and M. Parrinello. *Ab initio* molecular dynamics simulation of laser melting of graphite. *J. Appl. Phys.*, 83:2478–83, 1998.
- [83] K. Sokolowski-Tinten, J. Bialkowski, A. Cavalleri, and D. von der Linde. Transient states of matter during short pulse laser ablation. *Phys. Rev. Lett.*, 81:224–227, 1998.
- [84] K. Sokolowski-Tinten, C. Blome, C. Dietrich, A. Tarasevitch, M. Horn von Hoegen, D. von der Linde, A. Cavalleri, J. Squier, and M. Kammler. Femtosecond X-ray measurement of ultrafast melting and large acoustic transients. *Phys. Rev. Lett.*, 87:225701/1–4, 2001.
- [85] D. E. Spence, J. M. Evans, W. E. Sleat, and W. Sibbett. Regeneratively initiated self-mode locked Ti:sapphire laser. *Opt. Lett.*, 16:1762–4, 1991.
- [86] P. Stampfli and K. H. Bennemann. Dynamical theory of the laser-induced lattice instability of silicon. *Phys. Rev. B*, 46:10686–92, 1992.
- [87] P. Stampfli and K. H. Bennemann. Time dependence of the laser-induced femtosecond lattice instability of Si and GaAs: Role of longitudinal optical distortions. *Phys. Rev. B*, 49:7299–305, 1994.
- [88] Joachim Stör. *NEXAFS Spectroscopy*. Springer-Verlag, Berlin Heidelberg, 1992.
- [89] D. Strickland and G. Mourou. Compression of amplified chirped optical pulses. *Op. Commun.*, 56:219–211, 1985.

- [90] E. Tamura, J. van Ek, M. Fröba, and J. Wong. X-ray absorption near edge structure in metals: Relativistic effects and core-hole screening. *Phys. Rev. Lett.*, 74:4899–4902, 1995.
- [91] S. Techert, F. Schotte, and M. Wulff. Picosecond X-ray diffraction probed transient structural changes in organic solids. *Phys. Rev. Lett.*, 86:2030–3, 2001.
- [92] Michael O. Thompson, G. J. Galvin, J. W. Mayer, P. S. Peercy, J. M. Poate, D. C. Jacobson, A. G. Cullis, and N. G. Chew. Melting temperature and explosive crystallization of amorphous silicon during pulsed laser irradiation. *Phys. Rev. Lett.*, 52:2360–2363, 1984.
- [93] Motohiro Togaya. Pressure dependences of the melting temperature of graphite and the electrical resistivity of liquid carbon. *Phys. Rev. Lett.*, 79:2474–7, 1997.
- [94] H. W. K. Tom, G. D. Aumiller, and C. H. Brito-Cruz. Time-resolved study of laser-induced disorder of Si surfaces. *Phys. Rev. Lett.*, 60:1438–1441, 1988.
- [95] James H. Underwood and Jeffrey A Koch. High-resolution tunable spectrograph for x-ray laser linewidth measurements with a plane varied-line-spacing grating. *Appl. Opt.*, 36:4913–21, 1997.
- [96] H. van Brug, K. Murakami, F. Bijkerk, and M. J. van der Wiel. Time-resolved X-ray monitoring of laser ablation of and plasma formation from Si. *J. Appl. Phys.*, 60:3438–43, 1986.

- [97] I. Štich, R. Car, and M. Parrinello. Bonding and disorder in liquid silicon. *Phys. Rev. Lett.*, 63:2240–2243, 1989.
- [98] Y. Waseda and K. Suzuki. Structure of molten silicon and germanium by X-ray diffraction (and calculation of resistivity and thermoelectric power). *Z. Phys. B*, 20:339, 1975.
- [99] X. Weng, P. Rez, and P. E. Batson. Single electron calculations for the si  $l_{2,3}$  near edge structure. *Solid State Commun.*, 74:1013, 1990.
- [100] X. Weng, P. Rez, and O. F. Sankey. Pseudo-atomic-orbital band theory applied to electron-energy-loss near-edge structures. *Phys. Rev. B*, 40:5694, 1989.
- [101] G. K. Wertheim, M. A. Butler, and K. W. West. Determination of the gaussian and lorentzian content of experimental line shapes. *Rev. Sci. Instrum.*, page 1369, 1974.
- [102] C. M. Whelan, R. Neubauer, D. Borgmann, R. Denecke, and H-P. Steinruck. A fast X-ray photoelectron spectroscopy study of the adsorption and temperature-dependent decomposition of propene on Ni(100). *J. Chem. Phys.*, 115:8133–40, 2001.
- [103] K. Widmann, G. Guethlein, M. E. Foord, R. C. Cauble, F. G. Patterson, D. F. Price, F. J. Rogers, P. T. Springer, R. E. Stewart, A. Ng, T. Ao, and A. Forsman.

- Interferometric investigation of femtosecond laser-heated expanded states. *Phys. Plasmas*, 8:3869–72, 2001.
- [104] J. Workman, M. Nantel, A. Maksimchuk, and D. Umstadter. Application of a picosecond soft X-ray source to time-resolved plasma dynamics. *Appl. Phys. Lett.*, 70:312–14, 1997.
- [105] C. J. Wu, J. N. Glosli, G. Galli, and F. H. Ree. Liquid-liquid phase transition in elemental carbon: A first-principles investigation. *Phys. Rev. Lett.*, 89:135701, 2002.
- [106] M. T. Yin and Marvin T. Cohen. Theory of static structural properties, crystal stability, and phase transformations: Application to Si and Ge. *Phys. Rev. B*, pages 5668–87, 1982.
- [107] L. Zhu, V. Kleiman, X. Li, S. Lu, K. Trentelman, and R. J. Gordon. Coherent laser control of the product distribution obtained in the photoexcitation of HI. *Science*, 270:77–80, 1995.

**ERNEST ORLANDO LAWRENCE BERKELEY NATIONAL LABORATORY  
ONE CYCLOTRON ROAD | BERKELEY, CALIFORNIA 94720**